

**WASM: Minerals, Energy and Chemical Engineering**

**Permeability Evolution in Sandstone and Carbonate after  
Fracture Induced by CO<sub>2</sub> Injection**

**Olu-Ojo Toluwalope**

**This thesis is presented for the Degree of  
Master of Philosophy (Petroleum Engineering)  
of  
Curtin University**

**June 2020**

## **DECLARATION**

To the best of my knowledge and belief this thesis contains no material previously published by any other person except where due acknowledgement has been made.

This thesis contains no material which has been accepted for the award of any other degree or diploma in any university.

Olu-Ojo Toluwalope

---

June 16<sup>th</sup>, 2020

## DEDICATION

*To my wife, Abisola, and my kids, Teju and Bamise, who despite the associated rigors and time demand associated with undergoing this research degree, still encouraged me to start and complete.*

## **ACKNOWLEDGEMENT**

I would like to express my profound gratitude to my supervisor Dr. Mohammad Sarmadivaleh. I have the utmost appreciation for his steady guidance, knowledge-sharing, and encouragement which helped steer me in the right direction especially at times when the research seemed to hit a brick wall.

As well, I would also like to thank Dr. Nathan Taron and Bob Webb, who consistently provided the help required to get the required laboratory equipment operational during the experiments conducted in this research. This couldn't have been completed without their assistance.

Also, I'd like to acknowledge my fellow research students, with whom there were engaging and stimulating discussions that helped create a better understanding of research to me and proffered improved ways of achieving my set objectives.

## **Abstract**

Global warming mitigation solutions have included the capture of carbon dioxide from the atmosphere and its storage into geological bodies; one of the methods involves CO<sub>2</sub> being captured and injected into porous reservoir rocks embedded within the earth's crust. During the process of injection, there is pressure build-up within the reservoir; this consequently increased stress associated with the injection process and leads to geomechanical and geochemical changes within the geological storage sites.

Critical to the achievement of effective sequestration is the rock permeability; and, this permeability becomes a dynamic property dependent on the thermo-physical conditions of the storage rock. Numerous studies have researched the changes to permeability in sandstone and carbonate rocks undergoing triaxial compression, using live brine and supercritical carbon dioxide as the injection fluids. In this study, we went a step further and analysed the impact of induced fracture(s) on permeability as it occurs during geosequestration of CO<sub>2</sub> using live brine and supercritical CO<sub>2</sub> as injection fluids. The tests were conducted at reservoir conditions (10 MPa, 323 K) on Berea sandstone and Savonnières limestone rock samples which are the most prevalent reservoir rocks used as geosequestration sites.

As fracture occurred, the permeability evolution experienced differed based on the rocks types and the geomechanical or geochemical reactions occurring in the samples. The results showed that the permeability in both sandstone and carbonate decreased pre-fracture, as the triaxial compression caused compaction in the rocks; as the fracture was induced, there was created an enlarged pathway for fluid flow. Continued injection indicated a gradual increase in the permeability of the carbonate samples after fracture occurrence while the sandstone samples showed little to no increase during post-peak.

Findings from this study have improved the knowledge of the permeability evolution which occurs during simultaneous triaxial compression and injection of supercritical carbon dioxide in sandstone and carbonate rocks.

## Table of Contents

DECLARATION.....	ii
DEDICATION .....	iii
ACKNOWLEDGEMENT .....	iv
Abstract.....	v
Table of Contents .....	vi
List of Figures.....	viii
List of Tables.....	xiii
CHAPTER 1 INTRODUCTION.....	1
1.1 Background .....	1
1.2 Motivation of research.....	4
1.3 Objectives of this research .....	5
1.4 Organisation of thesis .....	5
CHAPTER 2 LITERATURE REVIEW .....	7
2.1 Introduction .....	7
2.2 Carbon Dioxide Sequestration .....	7
2.3 CO <sub>2</sub> sequestration options .....	9
2.4 Major CO <sub>2</sub> sequestration projects.....	12
2.5 Geochemical and geomechanical processes during CO <sub>2</sub> sequestration .....	14
2.6 CO <sub>2</sub> trapping.....	16
2.7 Sandstone and Carbonate rocks.....	19
2.8 Mechanical properties of Savonnières Limestone .....	20
2.9 Mechanical properties of Berea Sandstone .....	24
2.10 Stress generation during sequestration and effects on rock structure .....	25
2.11 Rock Permeability .....	27
2.12 Conditions affecting rock permeability .....	27
2.12.1 Grain size, shape & sorting .....	27
2.12.2 Overburden pressure .....	28
2.13 Fluid injection.....	29
2.14 Mechanical stress.....	30
CHAPTER 3 EXPERIMENTAL SETUP, MATERIALS & METHODS .....	36
3.1 Introduction .....	36
3.2 Equipment used .....	37

3.2.1 Triaxial compression system.....	38
3.2.2 Fluid injection system.....	41
3.2.3 Control system .....	42
3.3 Materials used .....	42
3.3.1 Rock Samples.....	42
3.3.2 Fluids and salts .....	52
3.4 Experimental procedure.....	53
3.4.1 Dead brine preparation .....	53
3.4.2 Live brine preparation .....	53
3.4.3 Rock sample preparation.....	55
3.4.4 Testing procedures .....	56
3.5 Permeability Measurement and calculations .....	60
CHAPTER 4 RESULTS AND DISCUSSIONS.....	61
4.1 Rock samples injected with dead brine.....	61
4.2 Rock samples injected with CO <sub>2</sub> saturated (live) brine .....	65
4.3 Rock samples injected with supercritical carbon dioxide (scCO <sub>2</sub> ) .....	70
4.4 Permeability change in rocks post-fracture.....	74
CHAPTER 5 CONCLUSION AND RECOMMENDATIONS .....	76
5.1 Conclusion.....	76
5.2 Recommendations .....	77

## List of Figures

Figure 1.1 Trend of CO <sub>2</sub> emissions due to fossil fuel combustion from 1900-2020. As cited in (IEA, 2020) .....	2
Figure 2.1 CO <sub>2</sub> Phase Diagram. Reproduced from (Aydin et al., 2010) .....	8
Figure 2.2.....	9
CO <sub>2</sub> density based on a geothermal gradient of 30°C/km. From Bentham and Kirby (2005) .....	9
Figure 2.3 Underground geological options for CO <sub>2</sub> storage. (From the Global CCS Institute).....	10
Figure 2.4 Pictorial representation of capillary trapping. From De Silva and Ranjith (2012) .....	17
Figure 2.5 Effective trapping mechanisms based on the length of stored CO <sub>2</sub> . Modified from Bert et al. (2005).....	18
Figure 2.6 Different categories of carbonate rocks based on the Dunham classification. From Akbar et al. (2000).....	19
Figure 2.7 UCS of Savonnières limestone using the scratch test method. From He et al. (2017).....	22
Figure 2.8 Young's Modulus of Savonnières flooded with live brine and scCO <sub>2</sub> . From Zhang et al. (2018) .....	23
Figure 2.9 Poisson's ratio of Savonnières flooded with live brine and scCO <sub>2</sub> . From Zhang et al. (2018) .....	23
Figure 2.10 Poorly sorted rock (left) with different grain sizes and well-sorted rock (right) showing similar grain size. Reproduced from (Selley, 2000) .....	28
Figure 2.11 Permeability evolution in Berea sandstone at different injection rates over time using (a) dead brine and (b) live brine. Reproduced from Iglauer et al. (2014).....	29
Figure 2.12 Sandstone shear band patterns at different confining pressures (Values in MPa) From Bésuelle et al. (2000). .....	33
Figure 2.13 Variations in Indiana limestone permeability evolution at different confining pressures. From (Zhou et al., 2011) .....	34
Figure 2.14 Relationship between permeability and effective stress in carbonate. From (Zhou et al., 2011) .....	35

Figure 3.1 Experimental setup of triaxial and fluid injection equipment showing; oven-fitted stress frame (a), Vinci pumps (b), heating control for Vinci pumps (b1), Reactor mixer (c), High pressure mixing cell (c1), Water heat bath (c2), mixer controller (c3), Recording computer (d), CO <sub>2</sub> cylinder (e), and data acquisition system (f). .....	37
Figure 3.2 Stress frame (a), Oven enclosure (b), Temperature controller (b1), Pressure measurement (c), Input pore pressure (c1), Output pore pressure (c2), Confinement stress (c3), Ram pressure (c3), and hydraulic ram (d). .	38
Figure 3.3 Setup showing (a) the Hoek cell affixed in the stress frame within the oven enclosure; and (b) schematic showing flow directions and applied stresses .....	39
Figure 3.4 End plug and cross-section of circular surface with two holes where one is dedicated to pressure measurement while the second hole injects fluid through rock sample.....	40
Figure 3.5 Vinci pumps <b>(i)</b> for injecting brine and CO <sub>2</sub> into the samples showing the <b>(a)</b> pump housing <b>(b1)</b> user interface control, <b>(b2)</b> fluid tank with temperature control jacket; positive displacement ISCO pumps <b>(ii)</b> to produce confining and axial pressure on rock specimen in Hoek Cell showing <b>(c)</b> pump controller and <b>(d)</b> oil tank; and <b>(e)</b> vacuum pump for removing air in the samples .....	41
Figure 3.6 Micro CT scan of Savonnières limestone showing (a) mouldic porosity, (b) intergranular macroporosity, (c) intergranular mesopores and (d) intra-granular microporosity .....	43
Figure 3.7 XRD of Savonnières limestone. Reproduced from (Zhang et al., 2018).....	44
Figure 3.8 SEM Image of Savonnières limestone .....	44
Figure 3.9 Thin section petrography of Savonnières showing limestone bimoldic porosity <b>bp</b> , intra ooid pores <b>iop</b> , palisidic fringing cement <b>f</b> , composite ooid <b>c</b> , concentric layer oolitic cortices <b>o</b> and superficial ooid <b>s</b> . From (Lebedev et al., 2014).....	45
Figure 3.10 Savonnières core samples R, N & H pre-testing.....	46
Figure 3.11 Berea core samples E, F & D prior to testing.....	47
Figure 3.12 XRD of Berea sandstone. Reproduced from (Kim et al., 2019)	48
Figure 3.13 SEM Image of Berea sandstone .....	48

Figure 3.14 Permeability values of Savonnières samples as measured with the AP-608 poro-permeameter .....	49
Figure 3.15 Porosity values of Savonnières samples as measured with the AP-608 poro-permeameter .....	50
Figure 3.16 Permeability values of Berea samples as measured with the AP-608 poro-permeameter .....	50
Figure 3.17 Porosity values of Berea samples as measured with the AP-608 poro-permeameter .....	51
Figure 3.18 Schematic of setup for live brine preparation and close up view of reactor.....	54
Figure 3.19 Protective wrapping of core samples in (a) teflon over aluminium foil (b) aluminium foil over teflon, and (c) polyolefin tubing as final layer prior to scCO <sub>2</sub> injection testing .....	55
Figure 3.20 Schematic of equipment setup for permeability evolution measurement tests with unsaturated (dead) brine injected.....	59
Figure 3.21 Schematic of equipment setup for permeability evolution measurement tests with live (CO <sub>2</sub> saturated) brine injected.....	59
Figure 3.22 Schematic of equipment setup for permeability evolution measurement tests with supercritical carbon dioxide (scCO <sub>2</sub> ) injected.....	60
Figure 4.1 Permeability evolution observed during simultaneous flooding with unsaturated brine and triaxial loading, up to failure, of Berea Sandstone sample 'A' .....	62
Figure 4.2 CT scan images of Berea Sandstone sample 'A' showing induced fractures across the cross-sectional area and longitudinal section after triaxial compression failure during flooding with unsaturated brine .....	63
Figure 4.3 Permeability evolution observed during simultaneous flooding with unsaturated brine and triaxial loading, up to failure, of Berea Sandstone sample 'B' .....	63
Figure 4.4 CT scan images of Berea Sandstone sample 'B' showing induced fractures across the cross-sectional area and longitudinal section after triaxial compression failure during flooding with unsaturated brine .....	64
Figure 4.5 Permeability evolution during simultaneous flooding with unsaturated brine and triaxial loading, up to failure, of Savonnières limestone sample 'R' .....	64

Figure 4.6 CT scan images of Savonnières limestone sample ‘R’ showing the induced fractures across the cross-sectional area after triaxial compression failure during flooding with unsaturated brine. ....	65
Figure 4.7 Permeability evolution observed during simultaneous flooding with live brine and triaxial loading, up to failure, of Berea Sandstone sample ‘E’	66
Figure 4.8 CT scan images of Berea Sandstone sample ‘E’ showing the induced fractures across the cross-sectional area and longitudinal section after triaxial compression failure during flooding with live brine. ....	66
Figure 4.9 Permeability evolution observed during simultaneous flooding with live brine and triaxial loading, up to failure, of Berea Sandstone sample ‘F’	67
Figure 4.10 CT scan images of Berea Sandstone sample ‘F’ showing the induced fractures across the cross-sectional area and longitudinal section after triaxial compression failure during flooding with live brine. ....	67
Figure 4.11 Permeability evolution observed during simultaneous flooding with live brine and triaxial loading, up to failure, of Savonnières Limestone Sample ‘1’ .....	68
Figure 4.12 CT scan images of Savonnières Limestone Sample ‘1’ showing a slightly induced fracture line across the cross-sectional area and longitudinal section after triaxial compression failure during flooding with live brine. ....	68
Figure 4.13 Permeability evolution observed during simultaneous flooding with live brine and triaxial loading, up to failure, of Savonnières limestone sample ‘H’ .....	69
Fig 4.14 CT scan images of Savonnières limestone sample ‘H’ showing the induced fractures across the cross-sectional area and longitudinal section after triaxial compression failure during flooding with live brine. ....	69
Figure 4.15 Permeability evolution observed during simultaneous flooding with super critical CO <sub>2</sub> and triaxial loading, up to failure, of Berea Sandstone sample ‘C’ .....	70
Fig 4.16 CT scan images of Berea Sandstone Sample ‘C’ showing the induced fractures across the cross-sectional area and longitudinal section after triaxial compression failure during flooding with supercritical carbon dioxide .....	71

Figure 4.17 Permeability evolution observed during simultaneous flooding with super critical CO <sub>2</sub> and triaxial loading, up to failure, of Berea Sandstone sample 'D' .....	71
Fig 4.18 CT scan images of Berea Sandstone Sample 'D' showing the induced fractures across the cross-sectional area and longitudinal section after triaxial compression failure during flooding with supercritical carbon dioxide .....	72
Figure 4.19 Permeability evolution observed during simultaneous flooding with super critical CO <sub>2</sub> and triaxial loading, up to failure, of Savonnières Limestone Sample N.....	72
Figure 4.20 CT scan images of Savonnières sample 'N' showing the induced fractures across the cross-sectional area and longitudinal section after triaxial compression failure during flooding with supercritical carbon dioxide.....	73
Figure 4.21 Permeability evolution observed during simultaneous flooding with super critical CO <sub>2</sub> and triaxial loading, up to failure, of Savonnières Limestone sample '2' .....	73
Figure 4.22 CT scan images of Savonnières sample '2' showing the induced fractures across the cross-sectional area and longitudinal section after triaxial compression failure during flooding with supercritical carbon dioxide.....	74
Figure 4.23 Berea sandstone after fracture showing the shear fracture and tensile crack at P <sub>c</sub> = 10MPa .....	74

## List of Tables

<i>Table 2.1 Global estimated geological storage capacity. From IPCC (2005)</i>	10
<i>Table 2.2 Rock mechanical properties of Savonnieres limestone.....</i>	24
<i>Table 2.3 Rock mechanical properties of Berea sandstone.....</i>	25
<i>Table 3.1 XRD derived composition of Berea sandstone.....</i>	47
<i>Table 3.2 Petrophysical properties of core samples injected with dead brine (Group 1) .....</i>	51
<i>Table 3.3. Petrophysical properties of core samples injected with live brine (Group 2) .....</i>	52
<i>Table 3.4 Petrophysical properties of core samples injected with supercritical CO<sub>2</sub> (Group 3) .....</i>	52
<i>Table 3.5 Experimental fluids used in for injection and sources.....</i>	53
<i>Table 4.1 Percentage change in permeability observed after fracture in rock samples .....</i>	75

# CHAPTER 1 INTRODUCTION

## 1.1 Background

Concerns on increased global carbon emissions have necessitated the search for a solution to curtail and minimize the volume of carbon dioxide emissions in the atmosphere. Responsible for these increasing emissions is the continued usage of fossil fuels. This quest has led to the development of carbon capture and storage (CCS) technology as an environmentally acceptable means for reducing carbon concentrations in the atmosphere (IPCC, 2006). Carbon capture and storage (CCS) refers to the processes involved in the extraction of CO<sub>2</sub> from point sources and its long term storage with the lowest possibility of reintroduction into the atmosphere.

Increased industrialisation leading to global economic advancements has created an upsurge in world energy requirements and the power required to run these industries is generated from fossil fuels, which undergo the process of combustion to provide energy. It is estimated that about 75-85% of the total global energy requirement comes from fossil fuel combustion (Aydin et al., 2010). And, it is expected that fossil fuel sources will still remain key energy providers for at least another century due to the numerous advantages posed over other sources of energy, some of which include abundance, cost of extraction and transportation.

Ever since the industrial revolution, the global carbon cycle has been greatly changed by human activities over the past two centuries and atmospheric CO<sub>2</sub> regulation by natural processes is evidently incapable of curtailing all the produced CO<sub>2</sub> (Falkowski et al., 2000). To tackle this rapidly growing phenomenon, CCS is employed as a solution to the containment of the carbon dioxide emissions associated with fossil fuel usage.

In the last two centuries, the levels of CO<sub>2</sub> concentration has risen greatly from average recordings of 280 ppm in the 19<sup>th</sup> century to 2018 values recorded at concentrations of 407.4 ppm and approximately 32.5 gigatonnes of CO<sub>2</sub> emissions annually released into the atmosphere (as shown in Fig 1.1)

stemming from industrial activities (IEA, 2018). In the year 2020 however, there has been a slight decrease of approximately 5% in the global CO<sub>2</sub> emissions due to the coronavirus pandemic (IEA, 2020); with economies gradually reopening, it is expected that the emissions might increase as industries resume operations after the imposed lockdowns.

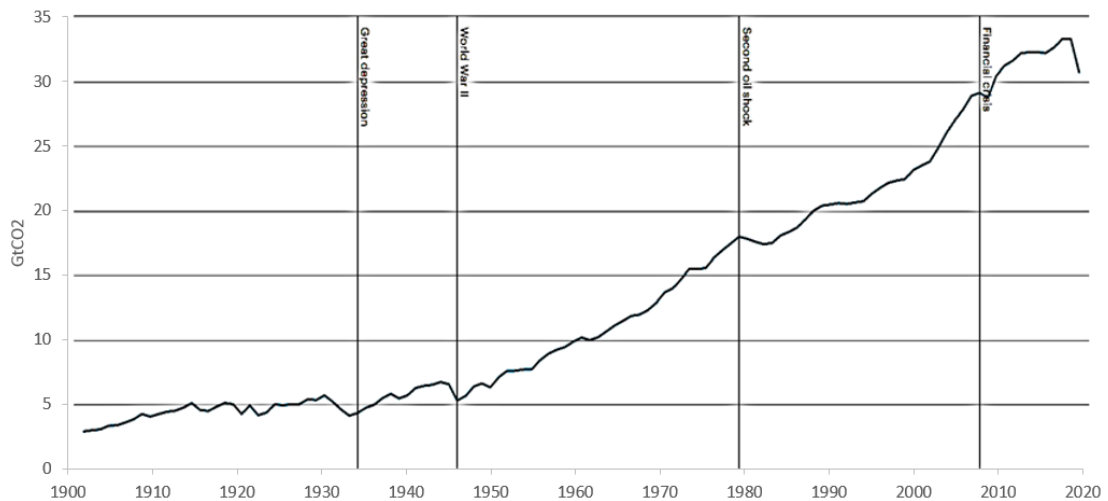


Figure 1.1 Trend of CO<sub>2</sub> emissions due to fossil fuel combustion from 1900-2020. As cited in (IEA, 2020)

Porous geological media have been identified as the most suitable sites for immobilising and trapping CO<sub>2</sub> in the long term, with the effective time of CO<sub>2</sub> storage suggested at a minimum of 1,000 years and up to 10,000 years (Espinoza et al., 2011) with sedimentary rocks being the main rock types used as storage sites- majorly sandstone and carbonates.

During carbon capture and storage process, the CO<sub>2</sub> is extracted, compressed and injected into geological storage at supercritical conditions (Benson & Cole, 2008; Bentham & Kirby, 2005; Hendriks & Blok, 1993); the supercritical state of the CO<sub>2</sub> aids in maximizing the storage capacity of the selected sites.

As the injected scCO<sub>2</sub> needs to displace existing brine in the formation, the injection pressure has to be higher than the formation fluid pressure (Holloway & van der Straaten, 1995). With the injected CO<sub>2</sub> having a higher buoyancy than the brine situated in the formation, there is a tendency to flow upwards; to

forestall this upward migration, certain mechanisms come into play which traps the CO<sub>2</sub> within the aquifer formation at different time scales.

The mechanisms that trap CO<sub>2</sub> and immobilise it by physical or chemical processes within the formation are categorised as: (i) structural/stratigraphic trapping (Biddle & Wielchowsky, 1994), (ii) mineral trapping (Benson & Cole, 2008; Xu et al., 2005), (iii) hydrodynamic or dissolution trapping (Bachu & Adams, 2003; Ennis-King & Paterson, 2005) and (iv) capillary or residual trapping (Benson & Cole, 2008; Hesse et al., 2008).

The injection pressure experienced at a sequestration site is high to enable the injection and storage of a considerable amount of CO<sub>2</sub> annually. As more volume of CO<sub>2</sub> is injected into storage, the fluid pressure within the formation increases as the overlying caprock above withstands the overpressure caused by the injection process; this increase in the fluid pressure induces mechanical stress within and around the formation (Rutqvist et al., 2007; Streit & Hillis, 2004). If the mechanical stresses reach excessive levels i.e. above the critical fracture point of the rock, it may lead to slip reactivation of existing faults or creations of new ones (Rigg et al., 2001; Sminchak et al., 2001).

The occurrence of this can improve fracture permeability and cause the release of CO<sub>2</sub>-saturated brine or CO<sub>2</sub> to the environment if the network of open fractures connects as pathways enabling the escape of CO<sub>2</sub> (Streit & Hillis, 2004). On the contrary, it can also lead to reduced permeability should there be closing off of existing pathways due to pore collapse under compaction or slip along the fault lines.

The flow of liquids through geomaterials is an aspect that necessitates in-depth research due to its high relevance to various real-life applications such as CO<sub>2</sub> sequestration, petroleum extraction, hydrology, wastewater injection, nuclear waste disposal to mention a few. This phenomenon of fluid flow through a porous material is described as permeability. In geosciences, accurate estimates of the permeability of the porous geological media is of great importance in determining the engineering operations to be executed at such sites. Permeability of rock, soil, or sediment refers to the ability to allow the flow of fluid through its pores and cracks.

## 1.2 Motivation of research

Understanding the numerous outcomes that can result from fracture development or reactivation during CO<sub>2</sub> sequestration is important in determining leakage probability or improving site storage efficiency.

Existing studies have investigated the change in permeability when scCO<sub>2</sub> or brine is injected into different types of rocks and the resulting outcomes. Iglauer et al. (2014) injected supercritical CO<sub>2</sub> and live brine into Berea and Fontainebleau sandstone samples. Their experiments revealed a greater reduction in permeability in the Berea sample - directly proportional to the flow rate; however, there was no noticeable change in permeability of the Fontainebleau samples during live or dead brine injection (this was attributed to the high quartz composition). Only the scCO<sub>2</sub> caused a significant decrease in permeability.

Azin et al. (2015) investigated chemical changes impacting porosity and permeability in carbonate due to dissolution and precipitation from CO<sub>2</sub>-rock-brine interaction. It was found that the dissolution of dolomite, which happened due to acidification of the aqueous system, led to an increase in porosity and permeability of the rock.

A few other studies include the injection of CO<sub>2</sub>-saturated brine (live brine) into sandstone and carbonate rock by Iglauer et al. (2014), investigation of permeability evolution when sandstone undergoes short and long term triaxial compression (Xu & Yang, 2016). These numerous studies have pointed out varying results of permeability evolution depending on the rock type and test conditions.

Investigations of the permeability evolution after fractures induced by CO<sub>2</sub> injection activities can provide insight into the management of ongoing sequestration and monitoring of CO<sub>2</sub> levels concerning changes experienced. Understanding the rock permeability behaviour can provide a wider knowledge for determining CO<sub>2</sub> migration behaviour when fracture occurs.

Rock critical pressure is a dynamic property that changes based on site-specific conditions, some of which are not constant during the lifetime of a

storage site. Results from this study can help predict rock critical pressure for existing and upcoming CO<sub>2</sub> storage sites during sequestration operations; this knowledge can be used to prevent unplanned fracture and risk of CO<sub>2</sub> escape.

Findings from this study can be helpful in the understanding of the favourability, or otherwise, that induced fracture has on the permeability and subsequently, CO<sub>2</sub> injectivity and permissible injection rate; with this knowledge, controlled fracturing can be employed to improve site storage efficiency.

### **1.3 Objectives of this research**

Stemming from the background and motivation to conduct this research, the following objectives will be set:

1. Investigate the impact that an increase in formation pore pressure due to brine and CO<sub>2</sub> injection has on the permeability of sandstone (Berea) and carbonate (Savonnières limestone) rocks before and after the initiation of fracture.
2. Conduct a series of laboratory experiments to identify the critical pressures for the sandstone (Berea) and carbonate (Savonnières limestone) samples respectively, while simulating *in situ* conditions encountered at CO<sub>2</sub> storage sites.
3. Conduct a series of laboratory experiments to measure the change(s) in permeability that occur when a rock is fractured as a result of high pressure due to scCO<sub>2</sub> injection into Berea sandstone and Savonnières limestone carbonate; the changes monitored will encompass permeability values prior and after the fracture has occurred.

### **1.4 Organisation of thesis**

There are five (5) chapters contained in this thesis. In Chapter 1, an introduction to the thesis is given- consisting of a background, motivation, and research objectives. Chapter 2 provides a literature review on the subject from current knowledge and existing research on permeability evolution during CO<sub>2</sub>

injection, chemical, and physical processes experienced in rock formations, as well as stresses developed in rock formations during sequestration.

Chapter 3 presents the experimental design, methodology, and description of materials used in the research. Subsequently, Chapter 4 presents and discusses the results attained from the concluded experiments while recommendations for improvement are made in Chapter 5, concluding the thesis.

## **CHAPTER 2      LITERATURE REVIEW**

### **2.1 Introduction**

In this chapter, the literature review of existing studies on rock permeability is analysed covering a range from the basics of CO<sub>2</sub> sequestration into storage formations to the stress generation experienced during injection; available information on the permeability changes encountered as formation rocks undergoes triaxial compression is also evaluated.

The chapter begins by explaining the sequestration concept identifying the phase behaviour of CO<sub>2</sub>, existing storage options for sequestration of CO<sub>2</sub>, statistics, and a few examples of existing CO<sub>2</sub> storage projects are mentioned. Next, the various trapping mechanisms of CO<sub>2</sub> in geological storage, changes due to injection in storage rock formations are discussed; stress effects due to sequestration and triaxial compression are evaluated.

Permeability of the storage rock has a key significance in the determination of fluid flow, injectivity, and plume distribution (Frailey & Leetaru, 2009). Injection of CO<sub>2</sub> into rocks creates an acidic solution as the CO<sub>2</sub> dissolves in the brine present in the formation (Kim et al., 2018); this acidic solution reacts with the geochemistry of the rock, leading to geophysical and geochemical changes. These changes and the resultant effect on permeability will be discussed as garnered from earlier studies conducted.

### **2.2 Carbon Dioxide Sequestration**

Numerous technologies have been proposed to stem the increasing concentrations of CO<sub>2</sub> in the atmosphere by either (i) reducing fossil fuel combustion or (ii) capturing and storing CO<sub>2</sub> emitted during fossil fuel extraction, combustion, and associated processes.

To successfully sequester CO<sub>2</sub> into geological formations, the injection is usually performed at levels below 800m (Bentham & Kirby, 2005; Koide et al., 1992); at this depth, formation temperature and pressure exceed 31.1°C and 7.38MPa respectively- which is the supercritical state condition for CO<sub>2</sub>. This supercritical state is the ideal state for sequestration operations as it is possible

to inject more CO<sub>2</sub> volume into storage because the CO<sub>2</sub> has a greater liquid-like density in this state while occupying all possible volume like a gas.

Figure 2.1 shows the physical states in which CO<sub>2</sub> exists depending on the pressure-temperature (P-T) conditions. At atmospheric conditions and between the temperature range of -56.5°C and 31.1°C CO<sub>2</sub> exists in a gaseous state; as the temperature drops below -78°C, it exists in a solid-state usually referred to as 'dry ice'. With increasing temperature comes decreasing density, while increasing pressure leads to a density increase for a fluid. The critical point conditions for CO<sub>2</sub> are temperature and pressure of 31.1°C and 7.38Mpa respectively; any values above these and the CO<sub>2</sub> exists in a supercritical state.

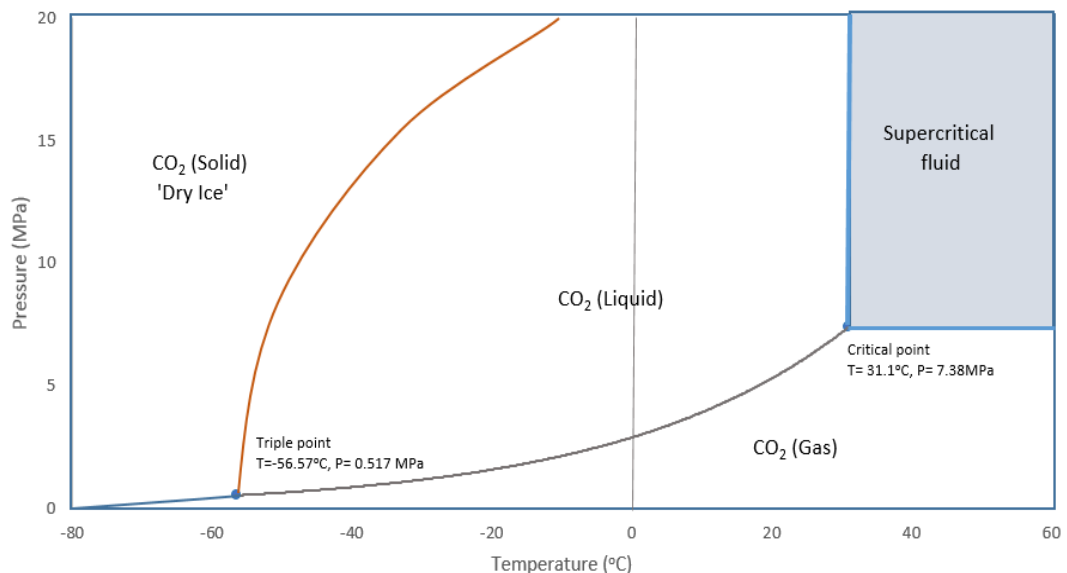


Figure 2.1 CO<sub>2</sub> Phase Diagram. Reproduced from (Aydin et al., 2010)

As the depth into the earth increases, pressure and temperature also increase which affect the physical state of CO<sub>2</sub>. A geothermal gradient of 30°C/km depth is generally considered to determine CO<sub>2</sub> density at varying depths of the rock formation measuring from the surface. Figure 2.2 shows the increasing density of CO<sub>2</sub> at various depths. For instance, at surface conditions of 0°C and 1 bar, one (1) tonne of CO<sub>2</sub> would occupy a volume of 509 m<sup>3</sup>; while the same amount of CO<sub>2</sub> occupies a mere 1.39 m<sup>3</sup> at subsurface conditions of 35°C and 102 bar- which are the estimated conditions at a depth of 1000 m.

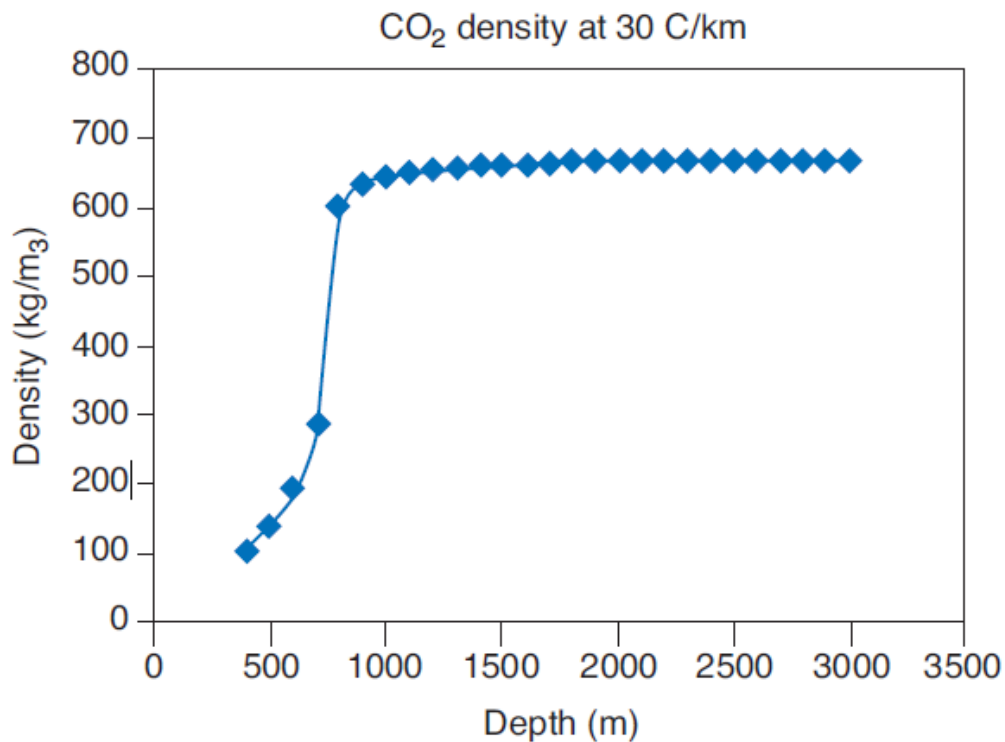


Figure 2.2 CO<sub>2</sub> density based on a geothermal gradient of 30°C/km. From Bentham and Kirby (2005)

### 2.3 CO<sub>2</sub> sequestration options

Currently, the different approaches identified to implementing CO<sub>2</sub> storage include: (i) in oceans as liquid, (ii) in underground geological formations as supercritical fluid (Falkowski et al.), and as (iii) solid carbonates via surface mineral carbonation (IPCC, 2005). Additionally, enhanced oil recovery with CO<sub>2</sub> (known as CO<sub>2</sub>-EOR) in petroleum production, invariably leads to CO<sub>2</sub> sequestration because a percentage of the injected CO<sub>2</sub> remains underground after the crude oil is extracted. The underground storage options are depicted in Figure 2.3.

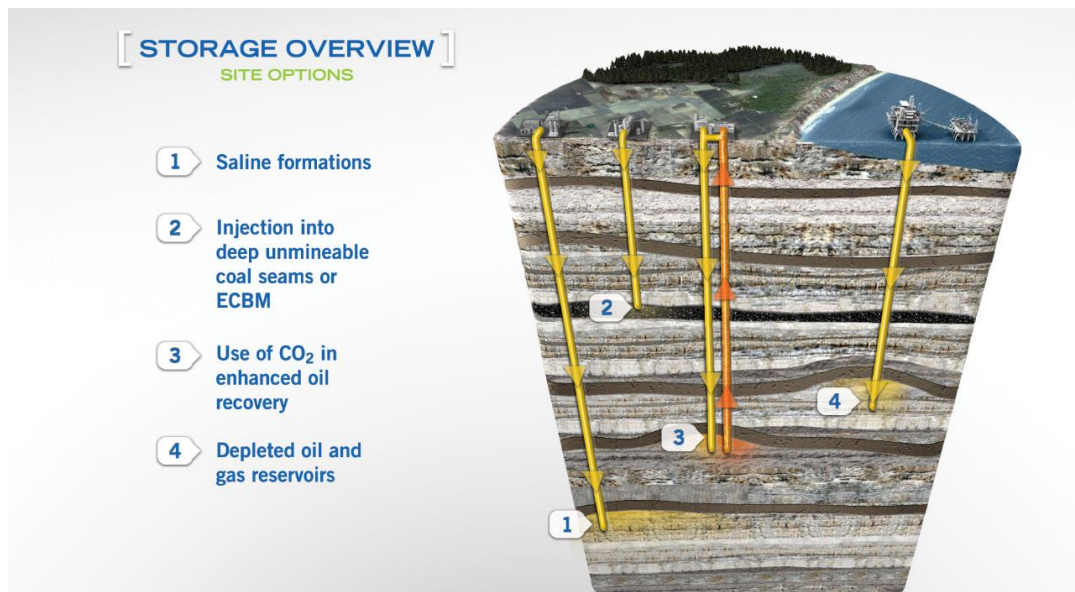


Figure 2.3 Underground geological options for CO<sub>2</sub> storage. (From the Global CCS Institute)

Of these three approaches to CO<sub>2</sub> sequestration, storage in geological formations is still considered the most viable option as the technology is presently the most understood of the available options and already widely used commercially. Storage in geological formations involves the injection of CO<sub>2</sub> into geological storage such as un-minable coal beds, deep saline aquifers or depleted oil and gas reservoirs. A snapshot of the estimated global storage capacity in the various options is shown in Table 2.1.

Table 2.1 Global estimated geological storage capacity. From IPCC (2005)

Geological Formation	Estimated Storage Capacity
Un-minable coal beds	3- 200 GtCO <sub>2</sub>
Depleted oil & gas fields	675-900 GtCO <sub>2</sub>
Deep saline aquifers	> 1000 GtCO <sub>2</sub>

Sedimentary basins are considered the most ideal for geological storage due to their high pore volume and high permeability, coupled with an extensive

abundance in nature (Bachu, 2000). According to the IPCC (2005), extensive research into the various possible geological settings for CO<sub>2</sub> storage have identified deep saline aquifers as providing the largest capacity with at least 1000 gigatonnes of global storage. In addition to the abundance, possible environmental impacts are more acceptable for underground injection compared to oceans where the existence of bio-diversity would pose more complexities in ensuring minimal adverse effects due to sequestration activities. So, while the ocean is seen as the largest sink for CO<sub>2</sub>, increased concentrations of CO<sub>2</sub> can greatly impact the ocean marine life negatively- a situation which is preferably avoided.

Another option, surface mineral carbonation- which is the combination of CO<sub>2</sub> with metals to form stable carbonate, is expensive to implement and still requires further technical studies to determine viability.

Saline aquifers refer to reservoir rocks that are pore filled with saline fluid which cannot be exploited for surface use- due to the fluid high salinity and depth; they usually occur at depths greater than potable water aquifers. A comprehensive understanding of the properties of any rock formation identified for CO<sub>2</sub> storage is important in storage site selection to achieve effective sequestration. Certain properties considered include: (i) adequate rock porosity to hold large volumes of CO<sub>2</sub>, (ii) suitable rock permeability to enable high injection rates of CO<sub>2</sub> without excessive pressure build-up in the formation (Falkowski et al.) and (iii) low-permeability cap rock to completely seal sequestered CO<sub>2</sub> underground and prevent leakages.

Precise measurements of permeability are critical for predicting CO<sub>2</sub> migration and correlating the stability of the CO<sub>2</sub> sequestered underground (Zhang et al., 2017). While high permeability formations are suitable for CO<sub>2</sub> injection into rocks at a high flow rate without creating excessively high pressure, there must be a highly impermeable cap rock overlay on the formation to prevent the escape of the sequestered carbon dioxide into the atmosphere.

Due to the overlying caprock, the formation experiences great confining pressure and high temperatures. During sequestration activities, formation pressure is continually increased and the low-permeability caprock formation,

situated above the high-permeability aquifer formation, is tasked with the prevention of the injected CO<sub>2</sub> (which is less dense than water) from flowing upwards to escape the site.

## **2.4 Major CO<sub>2</sub> sequestration projects**

As of 2018, there are a total of thirty-seven (37) large scale facilities identified globally for CO<sub>2</sub> sequestration. Of these, 17 are in commercial operation while the remainder are at various stages of development and construction (Bui et al., 2018)

Some of the major and pioneer sites currently in operation as dedicated CO<sub>2</sub> sequestration locations include:

- i. *The Sleipner project*** in the Norwegian part of the North Sea is the first purpose-built, commercial scale, offshore plant for CCS and became operational in the year 1996. The project was built to strip CO<sub>2</sub> from gas production in the Sleipner field and inject into the Utsira formation- which is a 200-250m thick sandstone formation situated at a depth between 800m -1000m below the seabed. As of 2010, the injection volume is stated as one million tonnes of CO<sub>2</sub> sequestered annually into the formation; and the site storage capacity estimated at 600 billion tonnes ("Sleipner Project," 2011).
- ii. *The Weyburn – Midale project***  
Located in Saskatchewan, Canada, this project was developed and started operation in 2000 to increase oil production via CO<sub>2</sub>-EOR from the Midale carbonate reservoirs. At an estimated lifespan of 20-25 years, the project currently injects CO<sub>2</sub> at a rate of 3000- 5000 tonnes/day. The aquifer at this location has ideal reservoir properties in the lower regions while the upper regions have very low permeability but high porosity.

iii. ***The Otway Basin project:***

The CO<sub>2</sub>CRC Otway Project in southwest Victoria, Australia was developed as Australia's first site for geological storage of CO<sub>2</sub>; the site demonstrated CO<sub>2</sub> injection into a depleted oil field- the Waarre C formation. Injection operations commenced in March 2008 and at completion in September 2009, 65 000 tonnes of scCO<sub>2</sub> had been injected into the formation located at a depth of 2053m (Cook, 2013). Learnings gained from the project brought up plans to execute the CO<sub>2</sub>CRC Otway Project Stage 2- to demonstrate effective CO<sub>2</sub> storage into a deep saline aquifer.

iv. ***The In Salah CO<sub>2</sub> Storage project,*** in the central region of Algeria, commenced operations in the year 2004. It is an onshore CCS site with an annual injection volume rate of between 0.5 – 1 million tonnes of CO<sub>2</sub> per year into a 20m thick, low-permeability, carboniferous sandstone formation located between depths of 1800-1900m in the Krechba gas field. The natural gas produced has a high CO<sub>2</sub> content which is extracted during the production process, compressed and stored underground. Due to the low permeability of the formation, long-reach horizontal injection wells are used for injection (Eiken et al., 2011; Ringrose et al., 2013).

v. ***The Snøhvit LNG project*** which is located in the northern part of the Norwegian Sea (often called the Barents Sea) incorporates a CCS system which extracts CO<sub>2</sub> and injects into the Tubåen formation located at 2400m below the seabed and with a thickness estimated at 110m (Eiken et al., 2011).

In recent times, the interest in locating carbonate rocks as CO<sub>2</sub> storage sites has increased tremendously due to abundance, as well as the natural trapping abilities of carbonate reservoirs (Shulakova et al., 2017). Approximately 60% of global oil reserves are located in carbonates rock types, with most of the reservoirs in the Middle East being carbonates (IEA,

2017). Furthermore, the reactivity of carbonates when in contact with injected CO<sub>2</sub> is as important since this may affect permeability and porosity of the rock.

## **2.5 Geochemical and geomechanical processes during CO<sub>2</sub> sequestration**

During CO<sub>2</sub> injection into argillaceous sandstones, the release of grain particles can be attributed to two main phenomena. The first being a geochemical process which is based on the theory that there is a critical salt concentration (CSC) level at which clay particles remain adhered to pore surfaces and any salt concentration levels below this would result in the release of the particles (Khilar & Fogler, 1984)

The second phenomenon is a mechanical process that occurs due to the hydrodynamic force exerted by the injected fluid. In this case, there is a critical fluid velocity that causes the release of particles from pore surfaces; this release is a function of the fluid velocity, the mechanism of particle release, and particle deposition (Ochi & Vernoux, 1998). This release occurs as the hydrodynamic forces supersede the attractive forces keeping the particles adhered to the pore surfaces.

Ochi and Vernoux (1998) experimented with fluid injection at various flow rates to validate the theory of throat plugging by grains of argillaceous sandstone. They injected synthetic brine into Berea sandstone samples at reservoir conditions, and realised the permeability decreased by about 50% with an initial increase in flow rate; however, the percentage decrease was not as much with successive flow rate increases, with the samples experiencing decreases of only 5% eventually. This gives an indication that the permeability changes occurred as a result of hydrodynamic mechanisms of release. At low flow rates, the permeability of some samples showed no change while greater permeability reduction was observed with increasing injection rates, thus lending credence to the hypothesis of fines migration and plugging reducing permeability during flow through the rock formation- attesting to the existence of a critical flow rate required to dislodge particles.

Excessive pressure build-up within a storage formation usually precedes many of the possible engineering challenges in carbon sequestration; also, the risk of CO<sub>2</sub> leakage or seismicity increases with increased formation pressure. During sequestration, as the desired volume of CO<sub>2</sub> is injected, the injection pressure needs to be constantly maintained below formation fracture pressure to prevent irreversible formation changes in the storage rock. Accurate estimation of injection pressure is required to prevent these changes.

Wigand et al. (2008) conducted experiments to investigate the effect of brine and supercritical CO<sub>2</sub> on Bunter sandstone, under simulation in situ reservoir conditions (P= 150 bar, T= 60°C). Results from their experiments showed that the dissolution of supercritical CO<sub>2</sub> in the formation brine alters the chemical characteristics. The decrease in PH and dissolution of the dolomite cement with an increase in the concentration of the major elements (Ca, Mg, Mn and Fe) were observed but limited reactivity occurred between the injected scCO<sub>2</sub> and the minerals- an indication that capillary trapping is the more dominant trapping mechanism than mineral trapping.

While dry CO<sub>2</sub> has low reactivity, once it interacts with brine it forms a weak acid (H<sub>2</sub>CO<sub>3</sub>) which easily breaks down into HCO<sub>3</sub><sup>-</sup> and CO<sub>3</sub><sup>2-</sup> and reduces the pH of the brine creating an acidic reaction with the minerals in the formation (Gaus et al., 2008). Also, owing to the number of minerals found in carbonate, geochemical effects are faster in carbonate formations compared to sandstone rocks; mineral dissolution occurs faster and on a more intense scale as the introduction of CO<sub>2</sub> causes water acidification (Espinoza et al., 2011).

Wormholes development in carbonate rocks need to be highly considered as these alter the permeability in the carbonate rocks. Wormholes are long cavities formed from the dissolution of unstable calcite minerals during the injection of CO<sub>2</sub> into carbonate formation. As carbon dioxide is injected into storage, a reaction occurs between the brine in the formation and the CO<sub>2</sub> leading to the formation of weak carbonic acid (Azin et al., 2015; Bachu et al., 1994; Izgec et al., 2008); this acidic environment created leads to the dissolution of the calcite existing in the formation. As the dissolution increases, the existing flow conduits increase in size ranging from a few millimetres to

conduits with diameters in meters. The injection rate determines the dissolution pattern experienced.

## 2.6 CO<sub>2</sub> trapping

During CO<sub>2</sub> injection, permeability anisotropy and relative permeability are factors determining CO<sub>2</sub> distribution in the aquifer; however, in the post-injection phase, the dissolution of CO<sub>2</sub> in the formation brine determines distribution.

Injection of CO<sub>2</sub> into saline aquifers leads to a disruption of the equilibrium state of the formation, causing reactions between the brine-in-formation, reservoir rock, and the injected CO<sub>2</sub> (Fischer et al., 2010). These reactions have a tendency of modifying the chemical, as well as the structural components of the reservoir and caprock resulting in the CO<sub>2</sub> being trapped via physical or chemical mechanisms or a combination of both. There are four main mechanisms currently identified that enable the gradual trapping of CO<sub>2</sub> underground. These are:

- I. **Structural/Stratigraphic Trapping**, where CO<sub>2</sub> is trapped underneath an impermeable cap rock (Bjørlykke & Jahren, 2010). This mode of trapping is usually enabled by the existing caprock preventing the flow of CO<sub>2</sub>; the density of scCO<sub>2</sub> at about 0.6-0.7 g/cm<sup>3</sup> is lower than that of saline formation brine, hence injected CO<sub>2</sub> tends to migrate upwards due to buoyancy forces. Once the CO<sub>2</sub> rises and eventually encounters the impermeable cap rock above the formation, it remains stored there since it cannot pass through the pore spaces of the caprock. The trapping due to impermeable rock connotes a structural trap and most of the sequestered CO<sub>2</sub> gets trapped via this mechanism.
  
- II. **Capillary Trapping**, or residual gas trapping, occurs where interfacial forces retain and immobilize some of the CO<sub>2</sub> in pore spaces as residual gas (Juanes et al., 2006). This type of trapping occurs as small amounts of CO<sub>2</sub> get disconnected and trapped by surface tension forces when CO<sub>2</sub> plume migrates and passes through pore spaces (Figure 2.4).

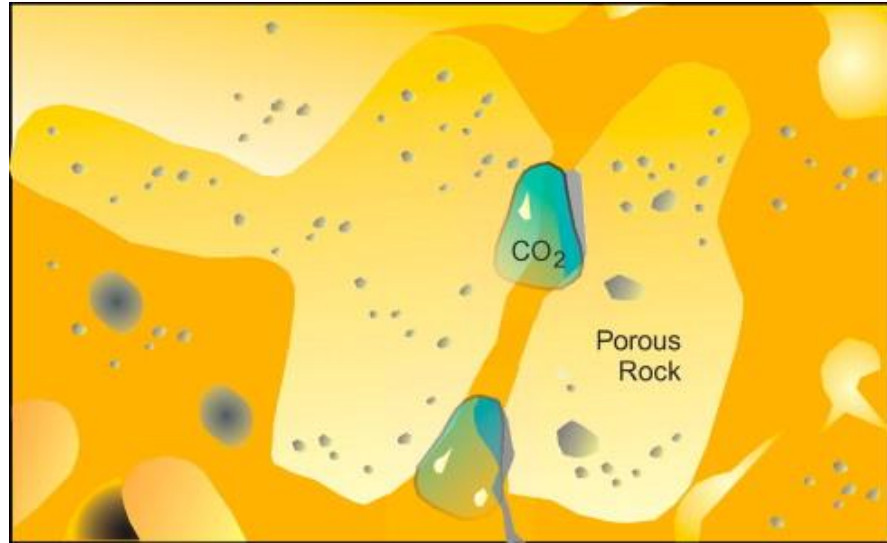
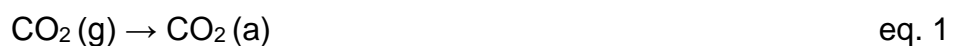


Figure 2.4 Pictorial representation of capillary trapping. From De Silva and Ranjith (2012)

- III. **Solubility Trapping**, also known as dissolution trapping, occurs as injected CO<sub>2</sub> dissolves into the formation brine turning it into dense CO<sub>2</sub> saturated brine (Al-Khdheawi et al., 2017; Iglauer, 2011); the dense brine sinks to the bottom of the aquifer due to greater density than the unsaturated parts of the formation brine, trapping the carbon dioxide. The chemical processes that occur (Bachu et al., 1994) are as depicted below:

The injected CO<sub>2</sub> in gas form dissolves into the brine to an aqueous solution (eq. 1); an equilibrium state is attained between the CO<sub>2</sub> and the weak carbonic acid formed (eq. 2)



Over time, this carbonic acid breaks down into bicarbonate and hydrogen ions,



Furthermore, the bicarbonate ions dissociate into H<sup>+</sup> and CO<sub>3</sub><sup>2-</sup>,



In carbonate rocks, the minerals present partially neutralize the acid by combining with the hydrogen ions, raising the pH of the brine in the formation (Rohmer et al., 2016) as below:



This process leads to the increase in the density of some of the formation brine, which then settles at the bottom of the formation.

IV. **Mineral Trapping**, where the CO<sub>2</sub> saturated brine undergoes chemical reaction with minerals in the formation via precipitation (Bachu et al., 1994). Factors like the rock matrix and chemical composition of the brine in the formation affect the rate of trapping via this mechanism (De Silva & Ranjith, 2012). As the injected CO<sub>2</sub> reacts with the brine to form a weak carbonic, over time this weak acid reacts with minerals present in the formation to form carbonate minerals e.g. CaCO<sub>3</sub>. This mode of trapping is regarded as the slowest and occurs over a longer period. Figure 2.5 shows the effective trapping methods at various stages of CO<sub>2</sub> storage.

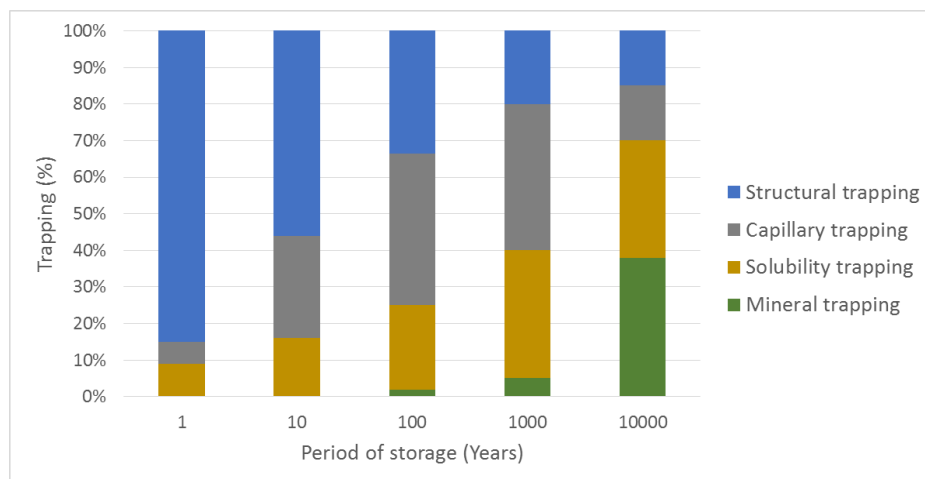


Figure 2.5 Effective trapping mechanisms based on the length of stored CO<sub>2</sub>.  
Modified from Bert et al. (2005)

At the initial stage of injection, CO<sub>2</sub> exists freely in the pore spaces of the reservoir as it gets trapped by either structural or capillary mechanisms; dissolution takes longer to happen, thus leading to pressure build-up in the reservoir as more CO<sub>2</sub> is injected (Liu et al., 2018).

## 2.7 Sandstone and Carbonate rocks

Unlike the homogeneity encountered in sandstone rocks, there is a lot of greatly varying conditions in carbonate formations. From microscopic pores with low permeability to highly permeable rocks with extensive wormhole networks that allow fluid flow, the extremes are often present within similar types of carbonates. Figure 2.6 shows a range of carbonate rocks. Most carbonate rocks are formed by sedimentation due to biological events or from precipitates of seawater. The main minerals found in carbonates are dolomite and calcite; others include phosphate, glauconite, pyrite, quartz, and clay minerals. Rock diagenesis of carbonate rocks significantly determines pore spaces, porosity, and permeability. An affinity to undergoing dissolution is a prominent feature of carbonates and occurrence along fractures leads to the creation of vugs, caves while pathways become enlarged turning into wormholes.

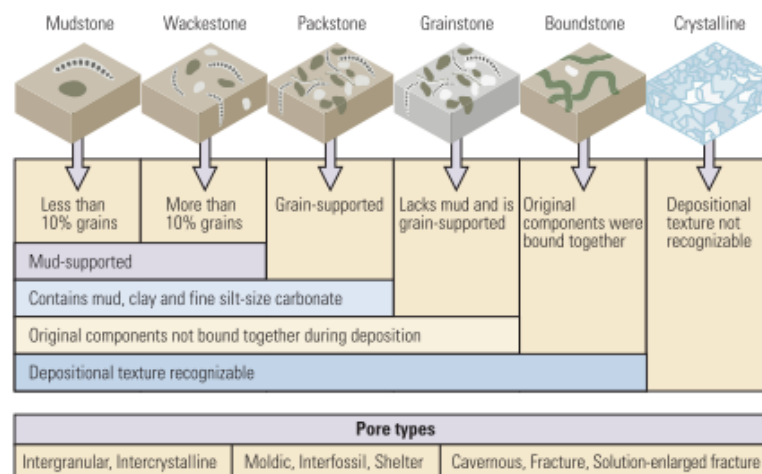


Figure 2.6 Different categories of carbonate rocks based on the Dunham classification. From Akbar et al. (2000)

The lure of carbonates and sandstones for sequestration is their abundance in nature and physical properties that enable the retention of large volumes in the pores of the rock formation.

Carbonate rocks refers to a class of sedimentary rocks which are composed majorly of carbonate minerals; however, there are also occurrences of sodium and potassium carbonates in formations. While carbonates are categorised based on diagenesis, grain texture, mud, and pore types, sandstones are majorly categorised based on the grain sizes and composition (Bjørlykke & Jahren, 2010). Characteristics of reservoir rock which make them ideal for CO<sub>2</sub> storage include high porosity and permeability.

## **2.8 Mechanical properties of Savonnières Limestone**

Important mechanical properties of formation rock commonly discussed include the UCS, Young's Modulus, Poisson's ratio, and cohesive strength. Performing compression tests on rock samples provide the primary data, namely stress, and strain, required to derive these mechanical properties. Of the numerous parameters used in describing the mechanical strength of a rock, the UCS (uniaxial compressive strength) is the most frequently used. UCS of a rock is determined by the chemical and mineralogical composition, porosity, rock fabric, and even by the specimen shape and size (Hawkins, 1998; Siegesmund & Dürrast, 2011) of the rock being tested.

The uniaxial compressive strength, UCS, of a rock specimen is calculated from:

$$\sigma_u = \frac{P}{A} \quad \text{eq. 6}$$

Where  $\sigma_u$  = uniaxial compressive strength, UCS

P = failure load; and

A = cross-sectional area of specimen

Various international standards have been developed to ascertain UCS of a rock. The three most referenced are: the International Society for Rock

Mechanics (ISRM ) for determining uniaxial compressive strength (Bieniawski & Bernede, 1979), the American Society for Testing and Materials (ASTM) standard for determining compressive strength for dimension stones (C170/170M-16, 2016) and the European standard for natural stones (UNE-EN, 1926:2007). To perform UCS testing using these standards, certain shapes and length-to-diameter ratio for the rock samples to be tested have to be adhered to- which can be more expensive and time-consuming. In recent times, various studies have been conducted to obtain the UCS via alternative methods.

Using specimen sizes smaller than the recommended standards, Van Stappen et al. (2019) investigated the UCS of Savonnières comparing large specimen at the recommended ISRM to smaller plugs while maintaining the L:D ratio of 2:1. Large specimens with diameter and length of 45mm and 90mm respectively- a ratio of L:D of 2:1, were tested for UCS; these were then compared to UCS results obtained from smaller plugs cored at length and diameter of 17–19mm and 8-9 mm respectively. From the tests conducted, an average value of 14.5 MPa was obtained as UCS for the large sizes, while the smaller plugs had an average of 15.7 MPa, indicating a minimal difference in values obtained.

Employing a simpler method, He et al. (2017) conducted studies on Savonnières limestone to determine UCS using a scratch test method which was identified as cheaper and less-challenging compared to the standardized procedures (Hobbs, 1964; Protodyakonov, 1960) from the ISRM. This scratch test method required minimal experimental setup and specimen preparation and is more applicable for measurements on rocks in situ compared to standardized methods of the ISRM.

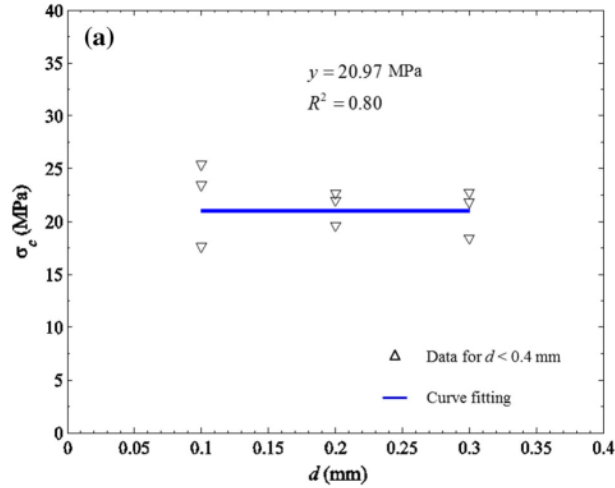


Figure 2.7 UCS of Savonnières limestone using the scratch test method. From He et al. (2017)

These tests were conducted using a range of 0.1mm to 0.4mm for the depth of cut; in their results, UCS of Savonnières limestone was estimated at 20.97 MPa (Figure 2.7), which is close to results obtained using the conventional UCS testing standards (Ulusay, 2014).

Young's modulus is another key rock mechanical property and is calculated using equation 7. In tests conducted by Zhang et al. (2018), they were able to describe the changes in mechanical properties of the Savonnières limestone rocks after carbon dioxide flooding. Using ultrasonic tests, the P and S waves of brine-saturated samples were measured and used to derive Young's modulus (eq. 7) while X-ray CT scans were done to reveal the changes in morphology after flooding. Using the P wave and S wave measurements, the Poisson's ratio- which is the ratio of lateral strain to longitudinal strain, can be derived from eq. 8.

$$E = \frac{\rho V_S^2 (3V_P^2 - 4V_S^2)}{V_P^2 - V_S^2} \quad (\text{eq.7})$$

$$\nu = \frac{V_P^2 - 2V_S^2}{2(V_P^2 - V_S^2)} \quad (\text{eq. 8})$$

Where  $E$  is Young's Modulus,  $\nu$  is Poisson's ratio,  $\rho$  is bulk density,  $V_p$  is P wave velocity and  $V_s$  is S wave velocity.

According to their tests, live brine flooding results (samples 9-13) led to an increase in Poisson's ratio (Figure 2.9) implying that the material experienced more material dissolution while injection of scCO<sub>2</sub> (samples 5-8) led to a slight decrease indicating the dissolution is not as much. From Figure 2.8, Young's modulus experienced a significant decrease after live brine flooding indicating the sample elasticity increased- which can be attributed to increased spaces between grains as a result of dissolution. A comparison of the various values obtained by different authors is shown in Table 2.2.

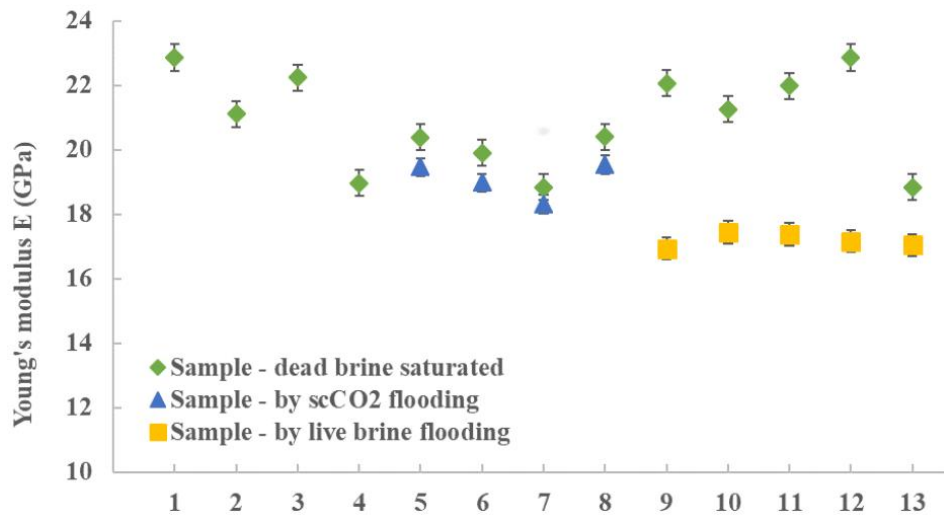


Figure 2.8 Young's Modulus of Savonnières flooded with live brine and scCO<sub>2</sub>. From Zhang et al. (2018)

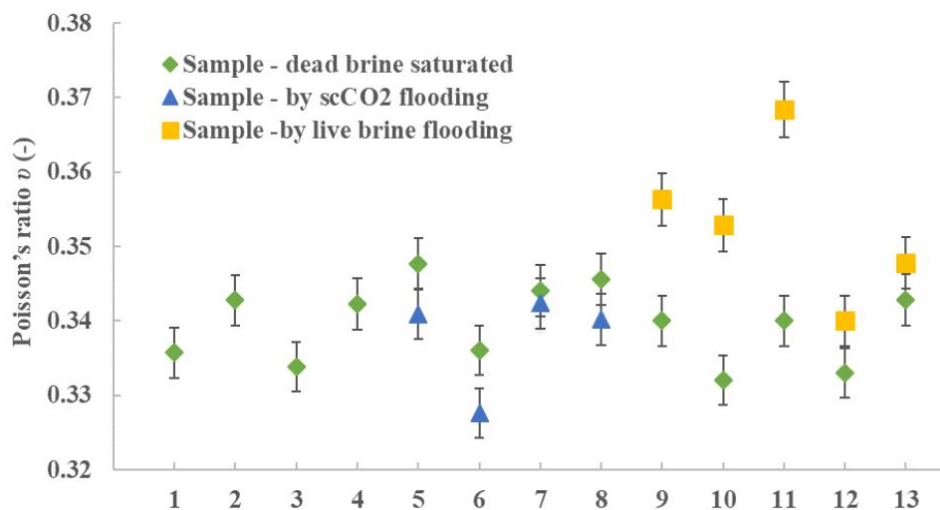


Figure 2.9 Poisson's ratio of Savonnières flooded with live brine and scCO<sub>2</sub>. From Zhang et al. (2018)

Table 2.2 Rock mechanical properties of Savonnieres limestone

<b>Mechanical Properties - Savonnieres</b>	<b>Reference</b>
<b>UCS</b>	
14.5 MPa - 15.7 MPa	<i>Van Stappen et al. (2019)</i>
20.97 MPa	<i>He et al. (2017)</i>
12.5 MPa	<i>Richard et al. (2012)</i>
<b>Young's Modulus</b>	
20.84 GPa- 22.32 GPa	<i>Zhang et al. (2016) *</i>
<b>Poisson's Ratio</b>	
0.33 - 0.35	<i>Zhang et al. (2016)*</i>
<i>*Measured samples cored from the same block like the ones in this study</i>	

## 2.9 Mechanical properties of Berea Sandstone

Uniaxial compression tests conducted on Berea sandstone by Kim et al. (2016) produced an average value of 46.11 MPa, which is comparable to UCS values obtained from similar Berea sandstones by Dehler and Labuz (2007) who obtained 46 MPa. As well, similar results have been reported for Rothbach sandstone (Louis et al., 2009) and Adamswiller sandstone (Gatelier et al., 2002). Comparing the standard uniaxial compression test against the Schmidt hammer test, Cargill and Shakoor (1990), were able to estimate the UCS for Berea sandstone noting a variance of about 8% between the two methods.; according to them, Berea sandstone was estimated as having a UCS of 54.21 MPa.

A handful of studies conducted on Berea provide a baseline understanding of behavioural patterns depicting petrophysical and morphological changes during injection of brine or supercritical CO<sub>2</sub> into Berea samples (Choi et al., 2017; Gray & Fatt, 1963; Iglauer et al., 2014)

Kim et al. (2019) conducted tests to determine the effect of water on the mechanical properties of Berea. Using a non-destructive ultrasonic method, the compressive (P wave) and shear (S wave) velocities were measured at a frequency of 1MHz with the rock samples in dry state and when saturated with water. Under static loading conditions, these measurements were used to

calculate (eq. 6) the Young's Modulus as 14.77 GPa at dry state while a value of 14.49 GPa was recorded after sample saturation with water, showing a minimal effect on the rock at static conditions.

Further studies were conducted on Berea sandstone by Delle Piane and Sarout (2016) to determine the effect of water and supercritical CO<sub>2</sub> on the mechanical and elastic properties of Berea sandstone. The samples were subjected to triaxial loading and temperature and ultrasonic measurements of the P wave and S wave were obtained and used to estimate the Poisson's ratio at 0.28. Also, from their tests, the maximum failure point for Berea sandstone was reported as 77 MPa with dilation observed setting in at differential stress of 54 MPa. Table 2.3 shows values obtained for Berea sandstone by different researchers.

*Table 2.3 Rock mechanical properties of Berea sandstone*

<b>Mechanical Properties - Berea</b>	<b>Reference</b>
<b>UCS</b>	
42.6 MPa	<i>Richard et al. (2012)</i>
46.11 MPa	<i>Kim et al. (2016)</i>
21.5 MPa – 43.55 MPa	<i>Li (2016)</i>
<b>Young's Modulus</b>	
14.77 GPa	<i>(Kim et al., 2016); Li (2016)</i>
19.2 GPa	<i>Madonna and Tisato (2013)</i>
21.4 GPa – 23 GPa	<i>Chapman et al. (2015)</i>
<b>Poisson's Ratio</b>	
0.38	<i>Chau and Wong (1996)</i>
0.32- 0.48	<i>Li (2016)</i>

## **2.10 Stress generation during sequestration and effects on rock structure**

Sequestration activities within a rock formation lead to the generation of stress as existing brine in formation is displaced to make space for the injected scCO<sub>2</sub>. Various studies conducted show that increasing stress affects the rock petrophysical properties- in this case, permeability and porosity being the

properties highlighted. Alam et al. (2014) identified compaction due to applied stress leading to a reduction in porosity as the pores get flattened and consolidated- subsequently leading to reduced permeability. The axial compression experiments conducted on sandstone showed a decrease in permeability with increasing axial stress; as the lateral strain value was recovered and the post-peak region reached, the permeability increased a little but never recovered to initial permeability values prior to axial compression. This decrease was attributed to the plastic deformation of the clay cementing materials contained in the sandstone.

Still, certain studies measuring the effect of stress on directional permeability allude to an increase in permeability citing reorientation of previously unconnected fractures/microcracks leading to new fluid flow paths as the basis for improved permeability (Gray & Fatt, 1963). Records from numerous experiments show that in the strain regime, permeability evolution is dependent on the strain regime under deviatoric loading conditions; in tests conducted on sandstone, initial porosity was identified as the main determinant in the brittle regime.

In high-porosity sandstones, it is understood that failures which occur during compaction lead to a great reduction in permeability due to pore collapse creating barriers to flow; on the other hand, low-porosity sandstones have been shown to experience an increase in permeability as enhanced connectivity of pore spaces happens during stress generation (Zhu et al., 1997)

As the temperature of CO<sub>2</sub> into the storage formation is usually lower than that existing in the rock, there is thermo-elastic stress induced on the formation rock, which further reduces the critical pore fluid pressure needed to achieve fracture initiation. Fracture gradient usually stated as 0.016 MPa/m, impacts the hydrostatic and lithostatic stresses, but not the thermo-elastic stress. CO<sub>2</sub> injection increases the stress on the formation rock, with fracture initiation resulting as the pore pressure exceeds the rock fracture point stress.

## **2.11 Rock Permeability**

In reservoir evaluation, permeability is a critical parameter to be analysed to determine viability for exploration or carbon dioxide sequestration since the effective characterization of fluid flow during these activities is hinged on the precise prediction of permeability (Zhang, 2013). Permeability is a critical rock property that determines the flow rate of fluid through the rock. As CO<sub>2</sub> is injected into a rock formation, the geomechanical and geochemical changes that occur result in either a positive or negative net effect on the permeability of the rock.

Primary permeability refers to the permeability of an intact rock prior to any exploratory, injection or production activities on the formation. This primary permeability is determined by the rock type, diagenesis as well as *in situ* conditions (Zhang, 2013). Permeability is denoted by '*k*' and is commonly measured in millidarcy.

## **2.12 Conditions affecting rock permeability**

Permeability evolution occurs as the formation experiences external activity altering the various factors which determine its permeability. Rock permeability and its evolution during varying levels of stress and pore pressure are of great interest during petroleum production, as well as CO<sub>2</sub> sequestration.

### **2.12.1 Grain size, shape & sorting**

Studies conducted by Coskun et al. (1993) attributed depositional texture, diagenesis, grain size, and sorting to the level of porosity and permeability in rocks. According to them, larger grain sizes result in higher permeability as the effective surface areas of conducting pathways increase with larger grain sizes. However, in sandstones that experience extensive carbonate cementation, the grain sizes alone do not determine the absolute permeability as the pore spaces would have some carbonate cement; distribution of the cement jointly determines the permeability. During injection activities, fluid flow

leads to the dissolution of the cementing bonds between grains causing fines release and altering permeability.

Various authors have proven that greater sorting produces higher permeability (Beard & Weyl, 1973; Rogers & Head, 1961). Grain sorting (Figure 2.10) refers to the uniformity observed amongst similarly sized grains within a range of sizes; well-sorted sedimentary rocks have grains that are of similar sizes. The similar-sized grains tend to create a network which exhibits consistent pore sizes and pathways- enhancing permeability. Poorly sorted rocks with variously sized grains in non-consistent proportions end up with the smaller grains plugging the pores and throats between the larger grains and eventually restricting flow and permeability.

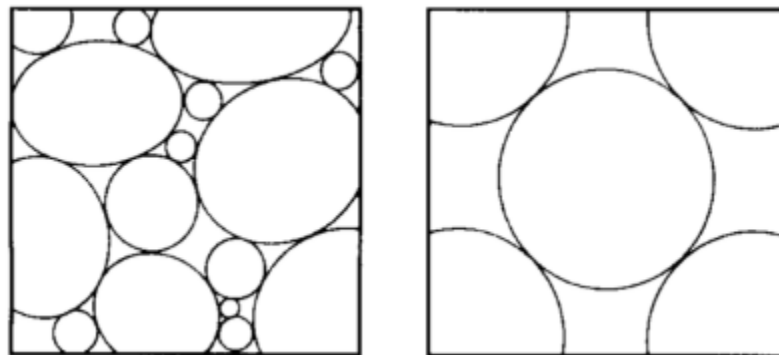


Figure 2.10 Poorly sorted rock (left) with different grain sizes and well-sorted rock (right) showing similar grain size. Reproduced from (Selley, 2000)

### 2.12.2 Overburden pressure

Thick overburden layers of the overlaying rock exert high confining pressure on the reservoir rock; as the depth increases, the overburden pressure correspondingly increases (Gray & Fatt, 1963). As a result, the rock's pore spaces undergo compression, leading to flattening. Permeability values depend on how much restriction is incurred based on the reduction of pore cross-sectional area due to flattening. Adding credence to this, reservoir sample rocks brought to the surface have been observed to expand in the absence of the overburden pressure encountered while in situ. Increasing overburden pressure leads to a reduction in rock permeability (Fatt & Davis, 1952; Zhou et al., 2011)

Also, a high temperature within a formation due to overburden pressure at increasing depth creates a volumetric expansion of the rock, which has an inverse effect on the discontinuity aperture, reducing the rock mass permeability (Zhang, 2013).

### 2.13 Fluid injection

*In situ* permeability can be exponentially greater than values obtained during laboratory experiments as a result of flow enhancement in scale fractures, coupled with the various pressure and temperature conditions.

Iglauer et al. (2014) conducted experiments on Berea and Fontainebleau sandstone samples, to determine the permeability evolution during injection of (i) CO<sub>2</sub> saturated brine, (ii) unsaturated brine and (iii) supercritical CO<sub>2</sub>. Their findings showed that live brine and scCO<sub>2</sub> injection significantly reduced the permeability in Berea sandstone by causing the release and transport of fines, which subsequently clog the pore throat; a conclusion deduced from the higher permeability reductions observed at higher flow rate. Fontainebleau, on the other hand, only showed marginal reduction in permeability with brine injection; however, injection of scCO<sub>2</sub> resulted in considerable permeability reduction.

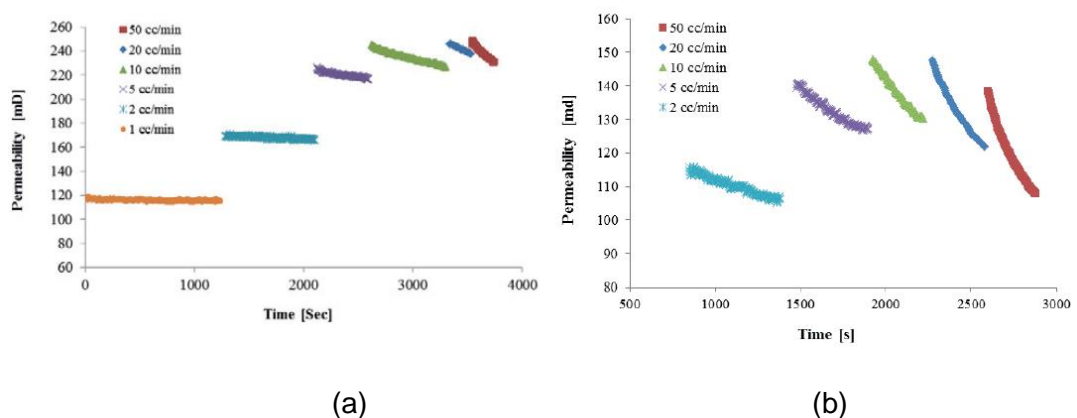


Figure 2.11 Permeability evolution in Berea sandstone at different injection rates over time using (a) dead brine and (b) live brine. Reproduced from Iglauer et al. (2014)

From Figure 2.11, the permeability reduction over time increased greatly at higher injection rates, indicative of the impurities contained in the sandstone dissolving faster, thus releasing fines and clogging throats faster.

Supercritical CO<sub>2</sub> injection tests performed on Savonnières limestone by Zhang et al. (2016) reported geomechanical weakening due to formation of wormholes in the samples; the samples were tested at *insitu* reservoir conditions of confining pressure at 15MPa, pore pressure of 10MPa and temperature of – representative of storage at a depth of 1000m in the earth's crust. The microstructure and geomechanical properties were noted to have undergone significant changes with permeability increments of between 24% - 42% recorded across the experimented samples.

Injection of CO<sub>2</sub> into low clay content Berea sandstone was performed by Al-Yaseri et al. (2017) to determine the evolution of permeability; their tests revealed factors affecting permeability as the salt type and concentration, acidity and clay minerals in the rock. However, the injection of CO<sub>2</sub> initially increased the permeability, but varying the injection rates did not affect permeability.

## **2.14 Mechanical stress**

Considerable changes in the physical properties of the reservoir rock are experienced during periods of geomechanical compaction due to *in situ* stress conditions; key property is the permeability, which is primarily dependent on the rock pore geometry (David et al., 2001). Several parameters determine the experimentally observed permeability evolution of rock under stress; some of these parameters include the loading conditions, initial porosity, fluid flow rate, strain loading rate, and temperature. Although permeability is an original geometric property, it is altered by stresses acting on the permeable rock. Some authors have replicated these stress conditions encountered during sequestration to provide an insight into the behaviours of rocks undergoing mechanical stress.

Zhu et al. (1997) conducted triaxial compression experiments on porous sandstone to investigate the effect on porosity and permeability in the axial direction when radial stress is applied up to sample failure. Testing of the samples was done at room temperature and axial stress was applied to cause failure by cataclastic flow resulting from the effective mean stresses on the specimen. Conducting the tests with pore pressure fixed at 10MPa and effective pressure between 80 to 250 MPa, their findings revealed an overall reduction in permeability. The trend showed an initial increase in the permeability as the effective mean stresses increased due to stress-induced microcracks growing parallel in the direction of the principal stress, thus providing additional conduits in the flow direction. However, once the critical stress state of the sample was attained, an abrupt decrease up to 3 orders of magnitude occurred; this massive reduction was attributed to pore collapse and crushed grains which occurred after attainment of the critical stress state.

Heiland (2003) conducted experiments on Lower Permian sandstone to investigate permeability changes under differential stress in pre-failure and failure regions of deformed rock. Results from their experiments showed an initial decrease in the low-porosity sandstone during compaction and a slight increase as the samples experienced dilatancy. Although an increase occurred with dilatancy, it never returned the permeability to the initial values prior to testing of the specimen. Essentially, a net decrease in permeability was experienced.

Experiments conducted on sandstone by Alam et al. (2014) showed that at confining pressure of 15MPa, similar to the overburden pressure at CO<sub>2</sub> storage depths of 1000m, permeability reduction in sandstone occurred as a result of grains compaction due to the cementing materials becoming thinner. It showed an initial decrease in permeability of Kimachi sandstone as axial stress was increasingly applied, followed by an increase as the total strain recovered its value; eventually, coalescing of the locally dense microcracks led to the increase in permeability around the peak load before maintaining stability in the residual strength state. These tests were carried out at confining pressures between 1- 15 MPa with the upper limit corresponding to effective vertical stress at depths of 1000m. Compaction was identified as the major

process leading to permeability reduction as the cementing materials became thinner with increased axial compression and the pore spaces reduced in area or closed up completely.

Xu and Yang (2016) conducted experiments to determine the evolution of sandstone under both short-term and long-term triaxial compressions. In their findings, they showed that the confining pressure had an effect on the mode of failure of the sandstone samples; consequently, the permeability evolution varies with the applied confining stress. As the deviatoric stress is increased, it was observed that the permeability slightly increased. This was attributed to the compression of primary cracks developing into fissures, thus enabling the improvement of flow. They identified three stages in the permeability evolution of sandstone similar to the deformation stages in a monotonic creep test. The first stage, called the decaying creep stage, shows the permeability decrease with increase in compaction volumetric strain; in the second stage, the permeability slightly increases as the volumetric strain also increases – known as the stable creep stage; the third stage, called the accelerate creep stage, witnesses a further increase in permeability as the volumetric strain goes from compaction to dilation. Lastly, there was a failure plane formation with a surge increase of permeability as percolation takes place. Also noted from their experiments is that the permeability evolution follows a similar trend even with different permeating fluids.

Triaxial compression experiments conducted by Chen et al. (2017) on sandstone to measure permeability evolution with damage induced show that pore pressure difference only slightly affected the permeability in sandstone; however, confining pressure was reported as having a significant influence on the sandstone permeability. Testing the sandstone samples at varying confining pressures of 10MPa, 20MPa, and 30MPa, they were able to show the various permeability trends obtainable due to differences in confining pressure. The permeability continually decreased as the deviatoric stress was increased; this was attributed to a decrease in the aperture of the microcracks originally connected in the rock being reduced as stress increased on the samples.

In triaxial compression tests conducted on Vosges sandstone by Bésuelle et al. (2000), it was shown that the number of failure surfaces increases correlatively with the increase in confining pressure. When confining pressure was maintained within the range of 10MPa to 30MPa while varying axial stress, the failure patterns showed one or two parallel bands which are indicative of the shear bands; at higher values of confining pressure, around 40-60MPa, more bands appeared. As the confining pressure increases, the number and angle of bands with respect to principal axial stress increase, as depicted in Figure 2.12

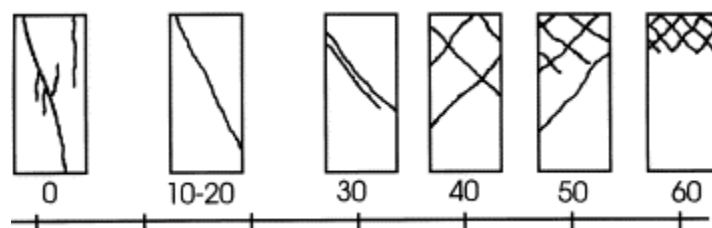


Figure 2.12 Sandstone shear band patterns at different confining pressures (Values in MPa) From Bésuelle et al. (2000).

In triaxial experiment studies carried out by Zhou et al. (2011) on Indiana limestone, their results showed that permeability could either be increased or decreased depending on the loading path and rock yielding behaviour- a property which, in carbonates, varies immensely. Contributing to the numerous possible behaviours of carbonate undergoing stress induced by CO<sub>2</sub> injection is the overburden pressure (replicated in the laboratory by confining pressure on the sample). As the overburden pressure increases correlating to the depth in the earth of the storage site, the behaviours and permeability evolution differ. At lower confining pressures of 100 psi and 300 psi, a decrease in permeability is noticeable during initial compression attributed to pore and micro-cracks closures while permeability increment is noticeable after the shear failure stage when the micro-cracks coalesce to improve pathway connections.

However, at greater confining pressures of 1500 psi - 4000 psi (correlating to values obtainable at required depths for CO<sub>2</sub> storage), the decrease in permeability is quite evident as depicted in Figure 2.13.

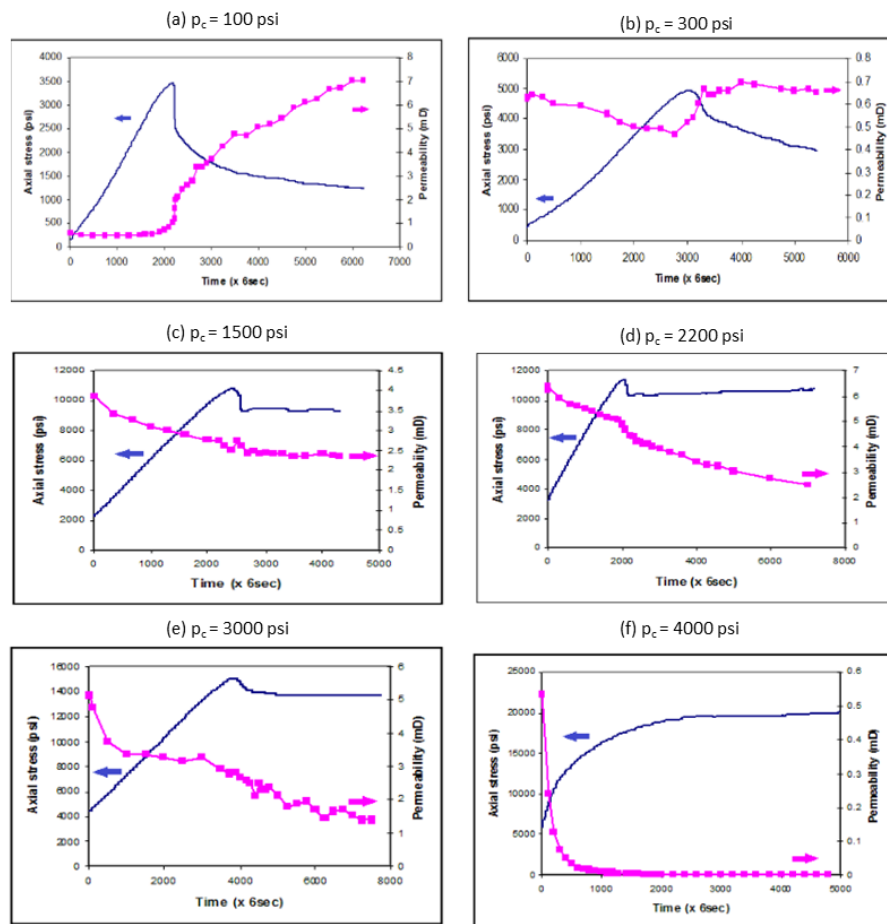


Figure 2.13 Variations in Indiana limestone permeability evolution at different confining pressures. From (Zhou et al., 2011)

As carbonates mostly have weaker microstructural rigidity due to their heterogeneity, it is easier to have pore collapses and compaction failure in the early stages of stress application at high confining pressure; hence tests to be carried out on carbonate will be at low confining pressure to avoid compaction before fracture failure.

During sequestration activities, the injection of CO<sub>2</sub> leads to an increase in pore pressure hence decreasing the effective stress. Fluctuations in the pore pressure of a reservoir determines the stress state conditions generated and the rock behaviour is a net outcome of the summation of pore pressure and stress. Based on the effective stress concept (Ghabezloo et al., 2009), the effective stress is given as

$$\sigma_{\text{eff}} = \sigma_t - bP_p \quad (\text{Eq. 10})$$

where,  $\sigma_{\text{eff}}$  is the effective stress

$\sigma_t$  is the total stress

b is Biot's factor

$P_p$  is the pore pressure.

From Figure 2.14, it can be seen that permeability is higher when the effective stress is lower. Hence, when confining pressure and pore pressure are maintained but the axial stress is increased, it is expected that the permeability reduces.

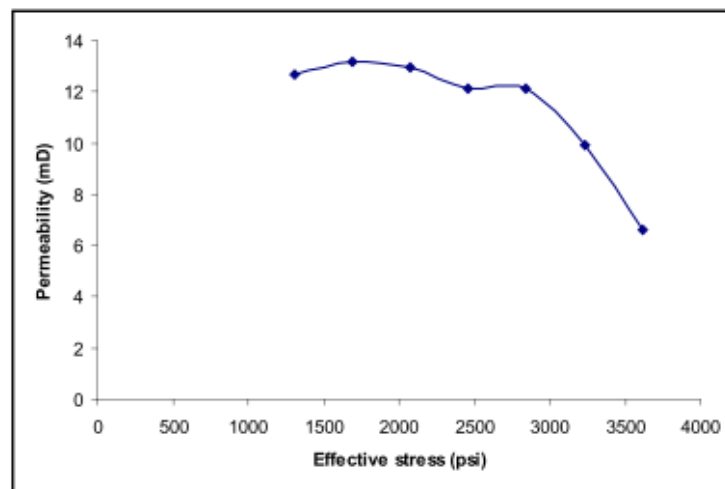


Figure 2.14 Relationship between permeability and effective stress in carbonate.  
From (Zhou et al., 2011)

As experienced within pore spaces, the permeability of fractures decreases as the compressive stress on the rock increases; points of contact between the uneven, rough surfaces of the fractures increase in number as well as in area, leading to some of the fractures totally closing off flow through them. (Mitchell & Faulkner, 2008; Walsh, 1981).

## **CHAPTER 3      EXPERIMENTAL SETUP, MATERIALS & METHODS**

### **3.1 Introduction**

In this chapter, the samples, and materials used in this study as well as the equipment, methods, and procedures will be discussed. The chapter commences by describing the physical and mineralogical properties of the sandstone and carbonate samples used in this study; the fluids used for injection into the samples are described as well. The equipment used and modifications, if any, are discussed to aid in describing the methods and procedures followed.

To achieve the objectives set out for this study, the experimental setup was designed to include equipment for triaxial compression tests, core-flooding, microstructural analysis via SEM imaging, and X-ray CT scanning. All the experimental activities were performed using existing equipment within the Curtin University Department of Petroleum Engineering laboratories and some equipment located at the CSIRO-Kensington laboratories. These equipment and processes are well described in the following sections.

The objectives are to:

1. Measure permeability evolution in core samples under triaxial compression with dead brine injected
2. Measure permeability evolution in core samples under triaxial compression with live brine injected
3. Measure permeability evolution in core samples under triaxial compression with supercritical carbon dioxide (scCO<sub>2</sub>) injected

Schematics showing the various setup configurations for the three different tests are illustrated within this chapter.

### 3.2 Equipment used

Various fluid injection and rock mechanics testing equipment are combined in different configurations to achieve the objectives of these experiments. Depending on the tests to be run, a few modifications are made to suit and enable the conditions necessary for testing. The equipment used can be grouped into three main categories namely a triaxial compression system, an injection system, and control system. The general equipment setup is shown in Figure 3.1.



Figure 3.1 Experimental setup of triaxial and fluid injection equipment showing; oven-fitted stress frame (a), Vinci pumps (b), heating control for Vinci pumps (b1), Reactor mixer (c), High pressure mixing cell (c1), Water heat bath (c2), mixer controller (c3), Recording computer (d), CO<sub>2</sub> cylinder (e), and data acquisition system (f).

### 3.2.1 Triaxial compression system

The equipment used to perform triaxial compressions on the core samples in this study comprises the (i) Hoek cell and (ii) stress frame. The stress frame is fitted with an oven enclosure capable of achieving temperatures as high as 70°C to enable reservoir temperature conditions for supercritical CO<sub>2</sub> and live brine. The Hoek cell is setup in the oven as shown in Figure 3.2, to keep the temperature constantly as required for maintaining supercritical condition of the CO<sub>2</sub> during flooding tests with live brine or scCO<sub>2</sub>. Attached to the oven is a controller to keep the set temperature within an accuracy of  $\pm 0.2^{\circ}\text{C}$ .

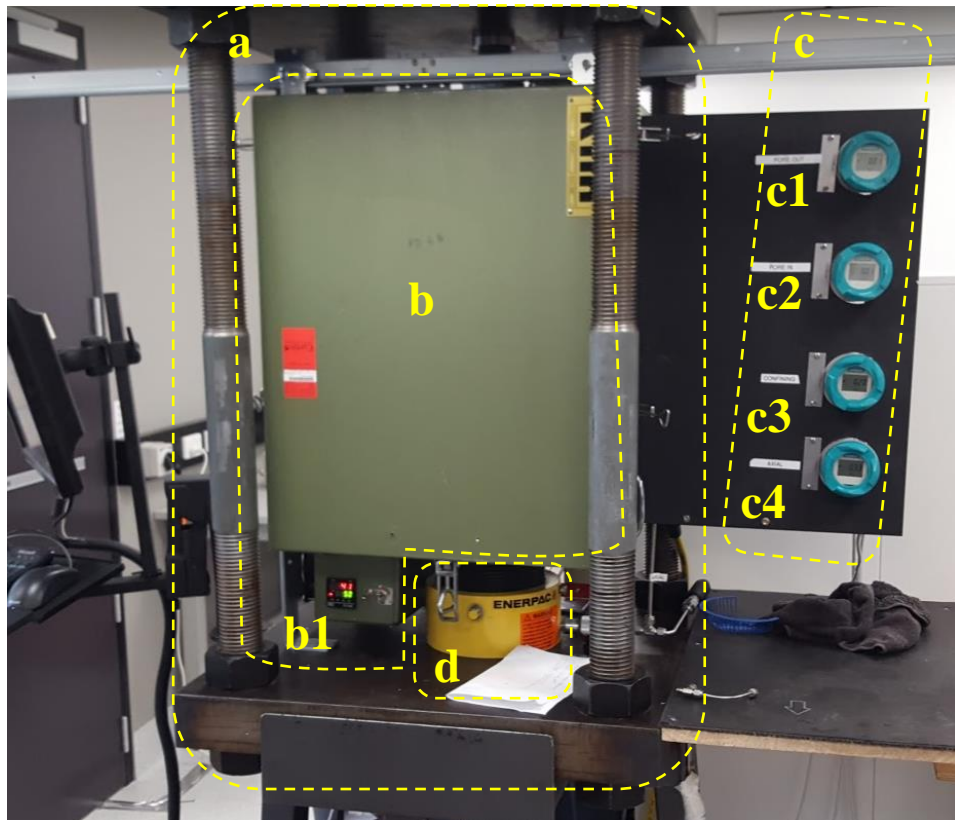


Figure 3.2 Stress frame (a), Oven enclosure (b), Temperature controller (b1), Pressure measurement (c), Input pore pressure (c1), Output pore pressure (c2), Confinement stress (c3), Ram pressure (c3), and hydraulic ram (d).

The Hoek cell (Figure 3.3a) houses samples during testing according to ASTM D7012 (Standard Test Methods for Compressive Strength and Elastic Moduli of Intact Rock Core Specimens under Varying States of Stress and

Temperatures). The particular model used in this study is capable of applying confining pressure up to 10000psi (70Mpa) on the rock samples; and able to accommodate samples of 38mm diameter and up to 90mm in length.

An ENERPAC hydraulic ram with a maximum limit of 70000 KN is used to directly apply axial stress on the sample. However, it was noted that the surface area of the ram is much larger than the surface area of the tested samples, hence a conversion factor needs to be applied to determine what the stress value on the hydraulic jack becomes when concentrated on the smaller surface of the samples. This information is easily obtained from the LabVIEW software used in data logging- evident in Appendix A. Based on this, a multiplication factor of 12.8 is applied to the pressure transmitted to the specimen due to the larger surface area of the piston compared to the samples.

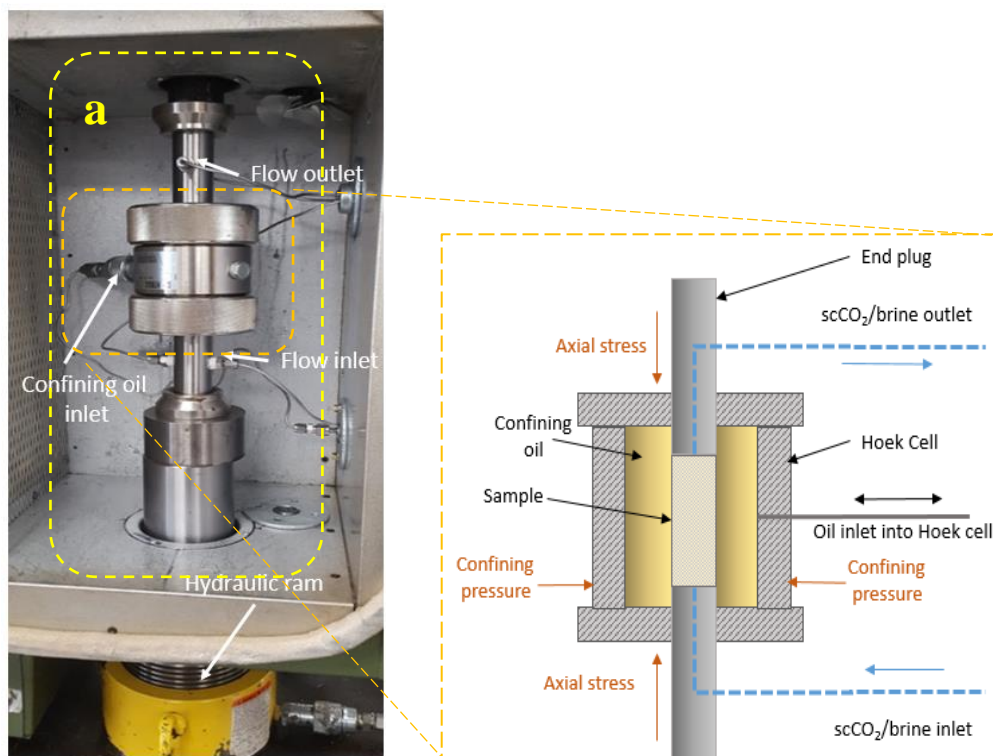


Figure 3.3 Setup showing (a) the Hoek cell affixed in the stress frame within the oven enclosure; and (b) schematic showing flow directions and applied stresses

Figure 3-3b shows the direction of flow within the specimen as setup in the Hoek cell; also shown are the various components that ensure a closed flow system through the specimen. The end plugs used at both ends of the samples to ensure uniform axial stress permeating fluid injection through the sample surface areas are shown in Figure 3.4. For better pressure measurements, one hole injects fluid through the rock samples while the second is dedicated to pressure measurement.

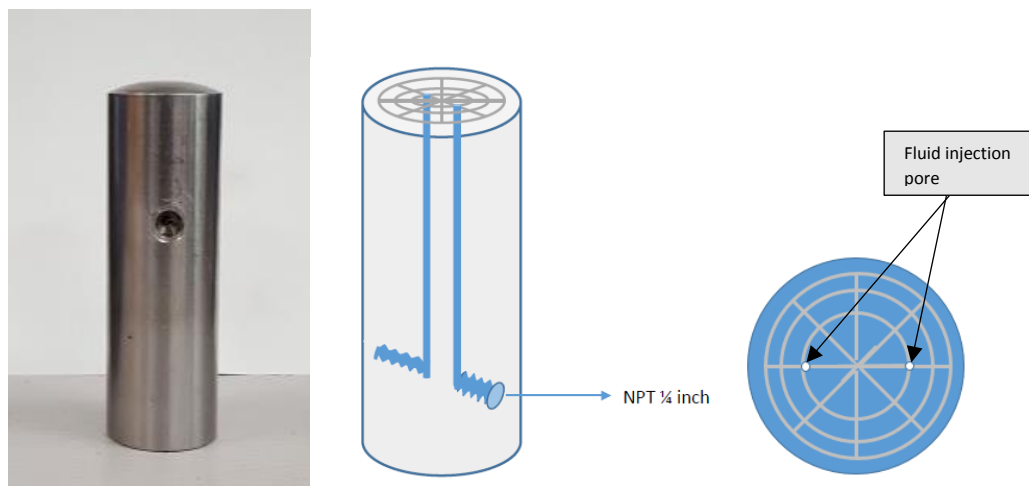


Figure 3.4 End plug and cross-section of circular surface with two holes where one is dedicated to pressure measurement while the second hole injects fluid through rock sample.

ISCO 260HP syringe pumps (0.5% FS pressure accuracy, Figure 3.5ii) provide the required hydraulic pressure for applying axial and confining pressure on the sample. ISCO pumps can provide constant flow, constant pressure and are programmable for gradual pressure increment. Injection of hydraulic oil produces the axial stress on the sample, back pressure, and confining pressure on the samples during test runs. The pumps are able to deliver precise, pulsation-free, positive flow over a range of 0.001 mL/min to 400 mL/min and capable of providing pressure up to a maximum of 10000psi (70Mpa).

### 3.2.2 Fluid injection system

A Vinci pump (shown in Figure 3.5a), which is a high pressure, dual syringe, positive displacement pump able to deliver specified pressure, volume, and flow rate at both ambient and reservoir conditions is used to inject the permeating fluids into the samples. The pump can be operated by running either in constant flow rate or constant pressure mode and has a maximum pressure capability of 70MPa.

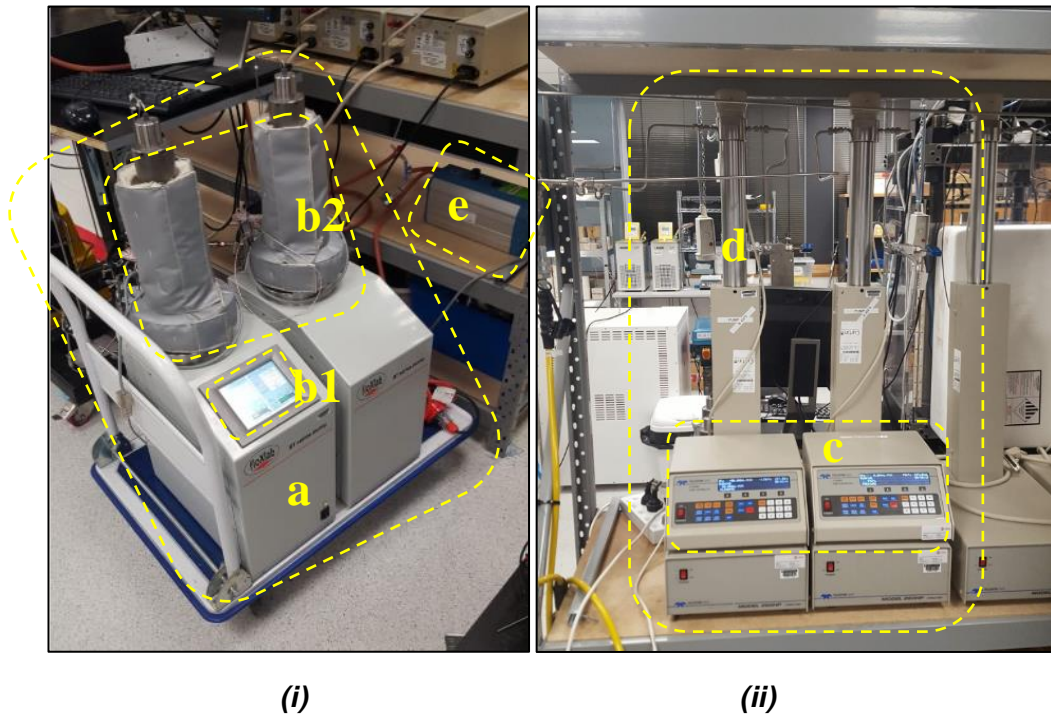


Figure 3.5 Vinci pumps **(i)** for injecting brine and CO<sub>2</sub> into the samples showing the **(a)** pump housing **(b1)** user interface control, **(b2)** fluid tank with temperature control jacket; positive displacement ISCO pumps **(ii)** to produce confining and axial pressure on rock specimen in Hoek Cell showing **(c)** pump controller and **(d)** oil tank; and **(e)** vacuum pump for removing air in the samples

All parts of the equipment that come in contact with liquid are made of either stainless steel or Hastelloy to minimise any fluid corrosion effect on the parts when exposed to wet scCO<sub>2</sub> or high salinity fluid at high temperatures and pressures. Each of these pumps is able to inject 250cc in one run.

A precision back-pressure regulator (BPR) capable of providing a maximum 5000psi of backpressure to the fluid flow is connected at the outlet position to help achieve steady pore pressure within the core specimen and ensure one-directional flow. This regulator is connected to an ISCO pump which maintains

the regulator pressure at 1000psi. A diaphragm within the regulator separates the oil from the fluid in the line being regulated.

### **3.2.3 Control system**

The connected equipment including the ancillary devices namely sensors, transducers and valves are all jointly monitored on a Windows OS desktop computer with monitoring and data logging software.

## **3.3 Materials used**

The rock samples used were cored into cylindrical shapes with diameters of 38mm and 64mm in length. The limestone samples were cored from a slab with the use of a wet diamond coring bit having an internal diameter of 38mm. After coring, a lathe machine was used to cut into the desired length and machined to ensure flat edges on the samples. Berea sandstones samples were obtained in the pre-cored dimensions from KOCUREK Industries – a rock supplier based in Texas, USA.

### **3.3.1 Rock Samples**

Savonnières limestone was used as the carbonate rock; while Berea sandstone represented the sandstone group. The Savonnières samples were cored with a diameter of 38mm (1.5in) and a length of 65mm (2.5in); the Berea sandstone samples were sourced from quarries in the U.S.A while the Savonnières came from France.

#### **3.3.1.1 Savonnières limestone**

The carbonate rock samples used in this study are Savonnières limestone, cored from a quarried block obtained from the Savonnières-en-Perthois quarries in the north-eastern part of France. Savonnières limestone is an oolitic and shelly limestone formed over 100 million years ago during the Upper Jurassic era (Fronteau et al., 2010). Compared to other oolitic limestones found in the Paris basin, a noticeable level of oolites dissolution can be observed in the Savonnières (Figure 3.6) which results in macro-pores within the oolites. The microstructure of the Savonnières is complex due to the diagenesis processes leading to its formation, resulting in both micro- and

macro-heterogeneity of the rock (Roels et al., 2003). There exist a diverse range of microfacies characterized by layers of dissolved shelly fragments, hollow ooids and dolomite present (Dewanckele et al., 2014), which increase the complexity of the rock's microstructure. Savonnières has a pore structure consisting of spherical and elliptical ooids and peloids which can have diameters up to 6mm; the ooids form through deposition and dissolution of concentric layers around a pre-existing nucleus while peloids lack internal structure (Flügel, 2013).

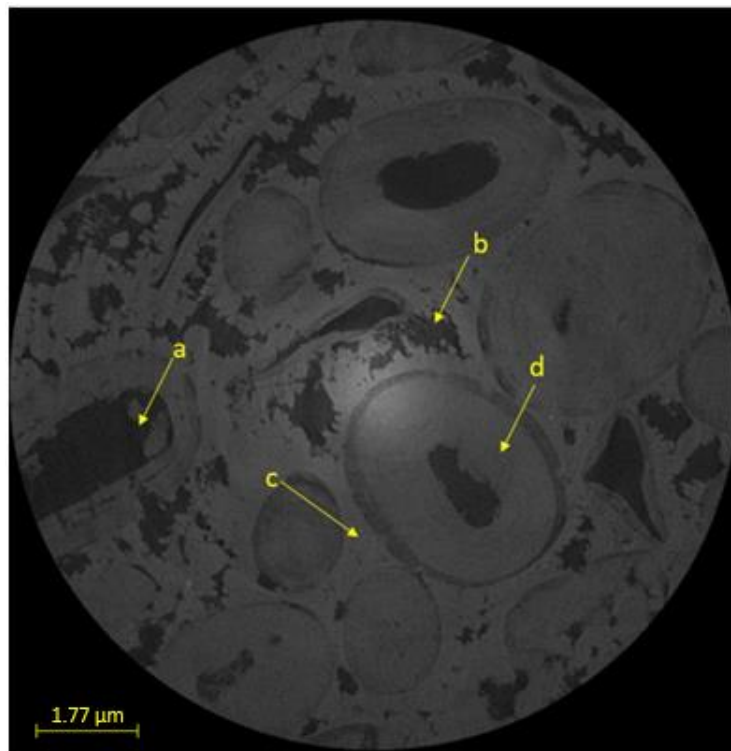


Figure 3.6 Micro CT scan of Savonnières limestone showing (a) mouldic porosity, (b) intergranular macroporosity, (c) intergranular mesopores and (d) intra-granular microporosity

During the diagenesis process, namely the cyclic dissolution and cementation, these hollow cores of ooids and ooid fragments are formed as dissolution occurs mostly in the high magnesium content area which surrounds the cortex- which is the low magnesium content area with sparite cement around it (Dewanckele et al., 2014). Savonnières limestone has roughly 97% calcite and 3% biotite composition, indicated in the XRD analysis in Figure 3.7, with fine

closely woven grey-beige grains and oolites having an average diameter of 500 $\mu\text{m}$ .

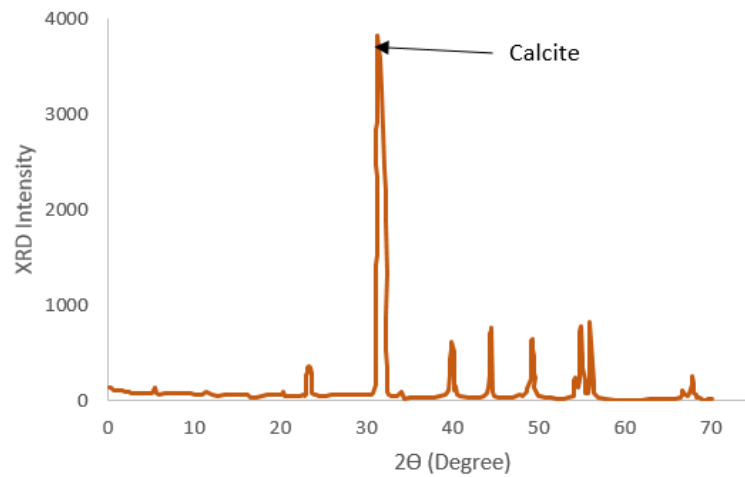


Figure 3.7 XRD of Savonnières limestone. Reproduced from (Zhang et al., 2018)

Scanning electron microscopy (SEM) analysis (Figure 3.8) and thin section petrography performed by Lebedev et al. (2014) show Savonnières as having oolitic grains that are partially cemented by clear, palisadic calcite cement with the long axis of crystal palisades extending between 200– 300  $\mu\text{m}$  in length. Also, the porosity is stated as ranging from 14-21% (Lebedev et al., 2014) and between 30-40% (Fronteau et al., 2010). The samples in this study have porosity values ranging from 23 to 29 %.

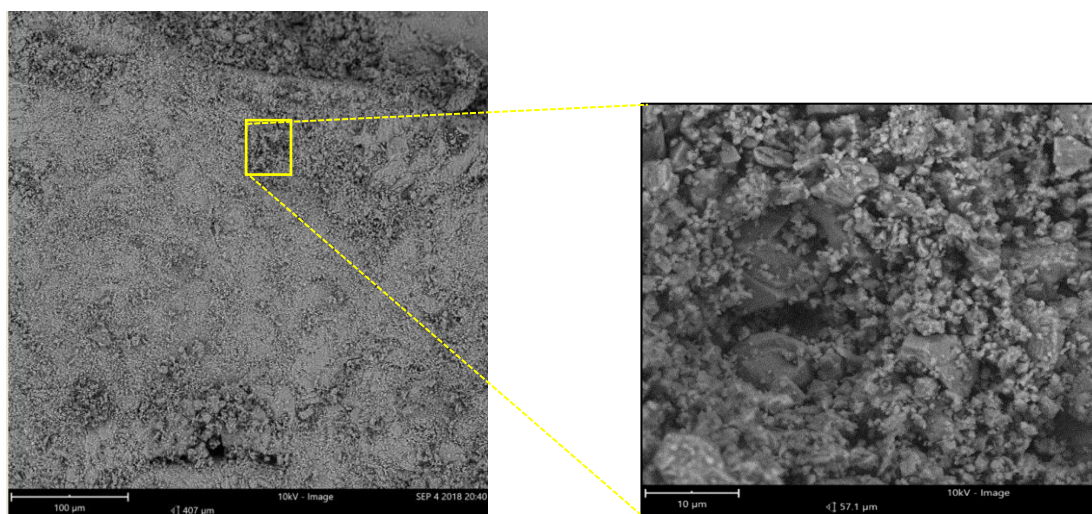


Figure 3.8 SEM Image of Savonnières limestone

Various pore types can be pointed out in the complex pore network existing in Savonnières. Some of these include bimoldic macropores 'bp', composite ooids 'c', intra ooid pores 'iop', concentric layer oolitic cortices 'o', all ranging in sizes from 0.0001mm – 0.1mm - depicted in Figure 3.9. These varying sizes lead to relatively low permeability compared to the porosity experienced in the rock.

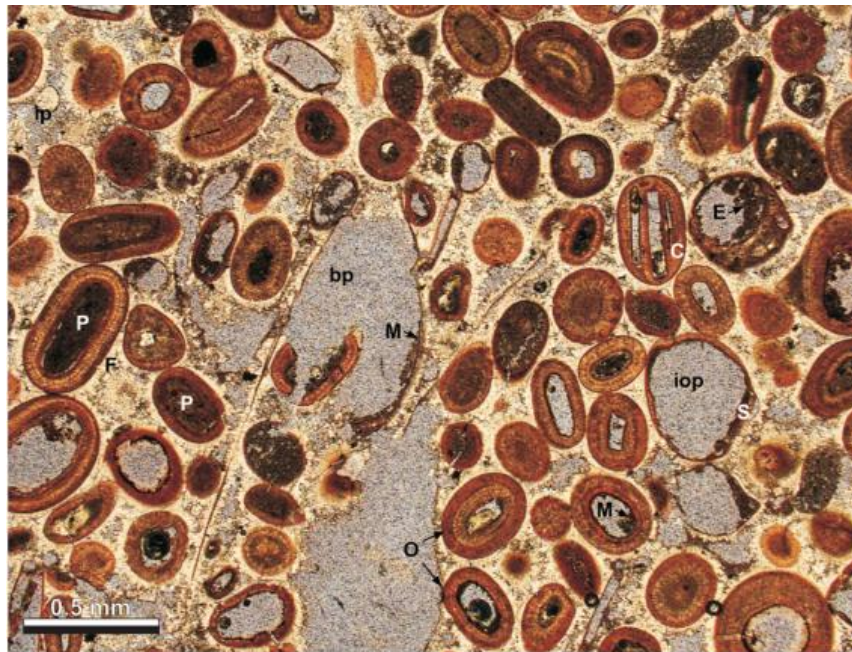


Figure 3.9 Thin section petrography of Savonnières showing limestone bimoldic porosity **bp**, intra ooid pores **iop**, palisadic fringing cement **f**, composite ooid **c**, concentric layer oolitic cortices **o** and superficial ooid **s**. From (Lebedev et al., 2014)

Numerous research has been performed on Savonnières limestone (Dewanckele et al., 2014; Mikhaltsevitch et al., 2016; Shulakova et al., 2017), and even further, in conjunction with CO<sub>2</sub> flooding within the Curtin (Lebedev et al., 2014; Lebedev et al., 2017; Raza et al., 2020; Zhang et al., 2018; Zhang et al., 2016). Hence building on these previous studies, the properties of Savonnières limestone are clearly identifiable and provide an established base for obtaining insight into the limestone rock.

Raza et al. (2020) investigated the feasibility of limestone reservoirs as geosequestration sites, specifically using Savonnières limestone. The samples involved were analysed prior to and after scCO<sub>2</sub> injection to find out

the petrophysical changes and mechanical degradations experienced when flooding is executed at low injection rates. In their findings, it was realised that there was an increase in porosity coupled with matrix dissolution leading to a reduction in the elastic and strength properties of the rock. Their studies also state that the low injection rate has a negligible effect on matrix dissolution as other studies conducted at high injection rates still reported some losses of matrix integrity.

Lebedev et al. (2017) noticed an abrupt increase in permeability of Savonnières limestone at the point of initial dissolution during the injection of live brine into the core samples (Figure 3.10); however, there was no considerable change in the permeability after the new level had been attained with continued flooding.



Figure 3.10 Savonnières core samples R, N & H pre-testing

### **3.3.1.2 Berea Sandstone**

Berea sandstone is a Mississippian terrestrial sandstone quarried from Berea, Ohio in the United States which, over the years, has been widely used in laboratory studies on reservoir topics. Its use has been popular across processes relating to fluid flow and transport, as well as phase interactions between water/oil/gas/rock. As it is quite homogenous, with well-defined characteristics and readily available, Berea is regularly employed in research and core flooding experiments on sandstone.

It is also widely used in studies on energy production (geothermal) and carbon dioxide sequestration and as a foundation for generating simulation models used in analysing permeability change. Its suitability is mainly hinged on its block scale homogeneity and lateral continuity, coupled with limited mineral composition and distribution of constant grain sizes. Berea has mostly quartz grains that are well distributed and smoothed with minor amounts of feldspar, dolomite and clays (Churcher et al., 1991).

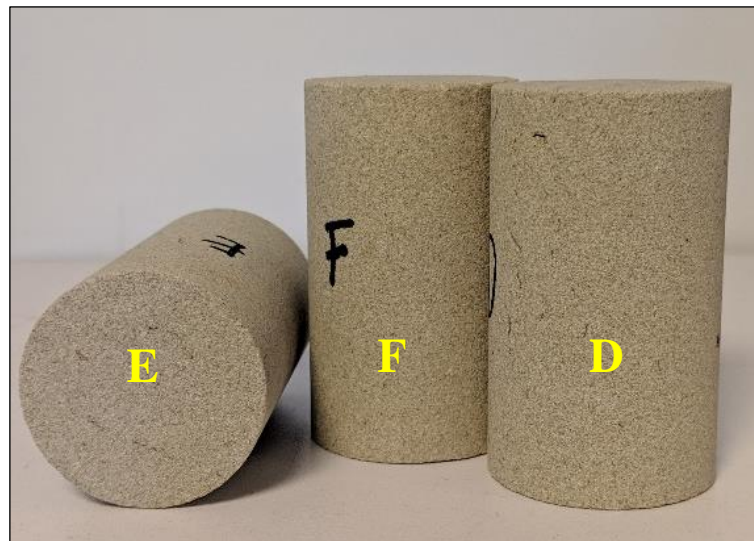


Figure 3.11 Berea core samples E, F & D prior to testing

Table 3-1 shows the mineral composition of the Berea sandstone (Figure 3.11) used in this experiment; X-ray diffraction analysis was used in evaluating the mineralogy composition and content of the rock samples, also depicted in the XRD image in Figure 3-12.

Table 3.1 XRD derived composition of Berea sandstone.

Mineral composition	Wt %
Quartz	87
Albite	3
Calcite	2
Kaolinite	6
Illite	2

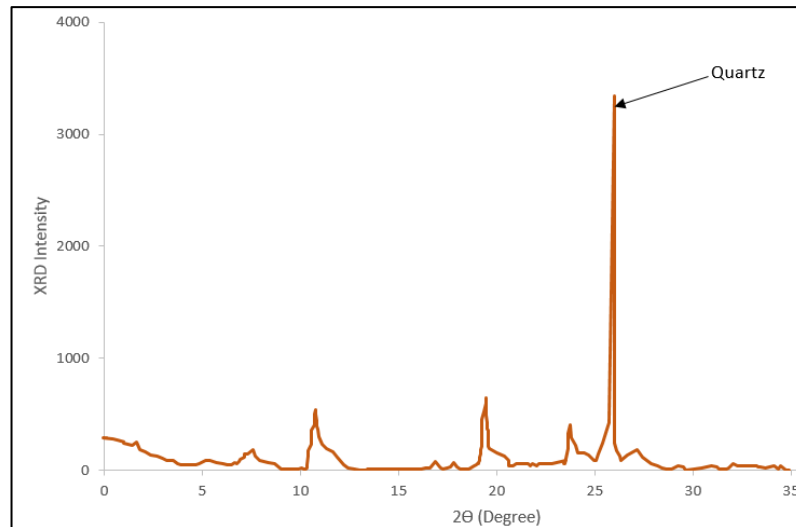


Figure 3.12 XRD of Berea sandstone. Reproduced from (Kim et al., 2019)

Using a combination of focused ion beam-scanning electron microscopy (FIB-SEM) and micro-computed tomography (CT), Berea sandstone is described as having interconnected small pores with diameters ranging from 30-40  $\mu\text{m}$  and large voids with diameters of 100-250  $\mu\text{m}$  (Bera et al., 2011) and as indicated in Figure 3.13. Berea sandstone has high permeability with values stated to be between 100 to 400 mD and porosity values between 19% - 24% (Gray & Fatt, 1963).

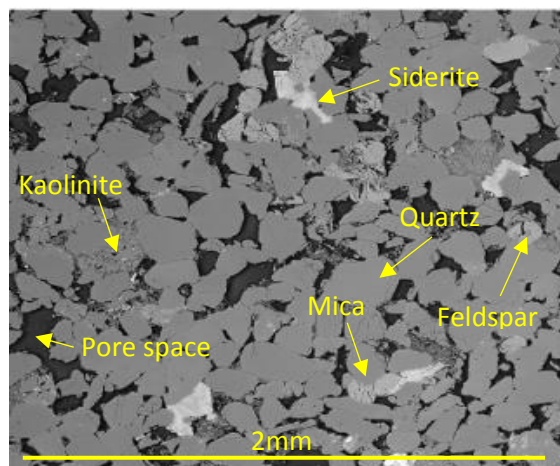


Figure 3.13 SEM Image of Berea sandstone

Prior to testing each sample, the initial porosity and permeability were measured before core flooding. An AP-608 automated helium porosi-

permeameter equipment was used for this measurement; the AP-608 is able to perform tests at confining pressures of up to 9950 psi across a wide range of permeability values from 0.001 mD to > 10D. Using a pressure decay method, it determines the porosity and the Klinkenberg-corrected permeability of a sample by injecting inert gas through the sample. The measured permeabilities for the Savonnieres rock samples used are shown in Figures 3.14 and 3.15 with porosity measurements feature in Figures 3.16 and 3.17.

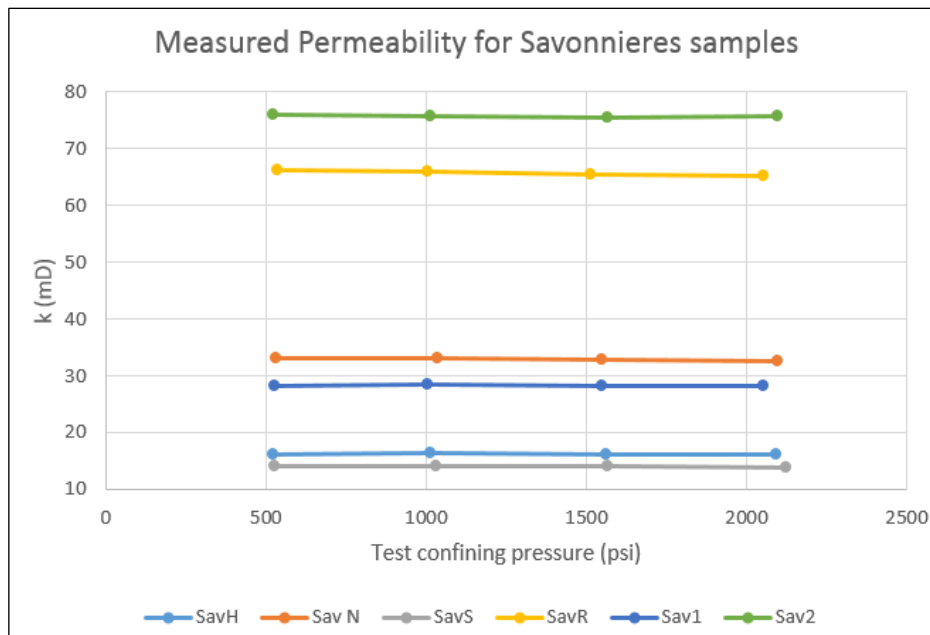


Figure 3.14 Permeability values of Savonnieres samples as measured with the AP-608 poro-permeameter

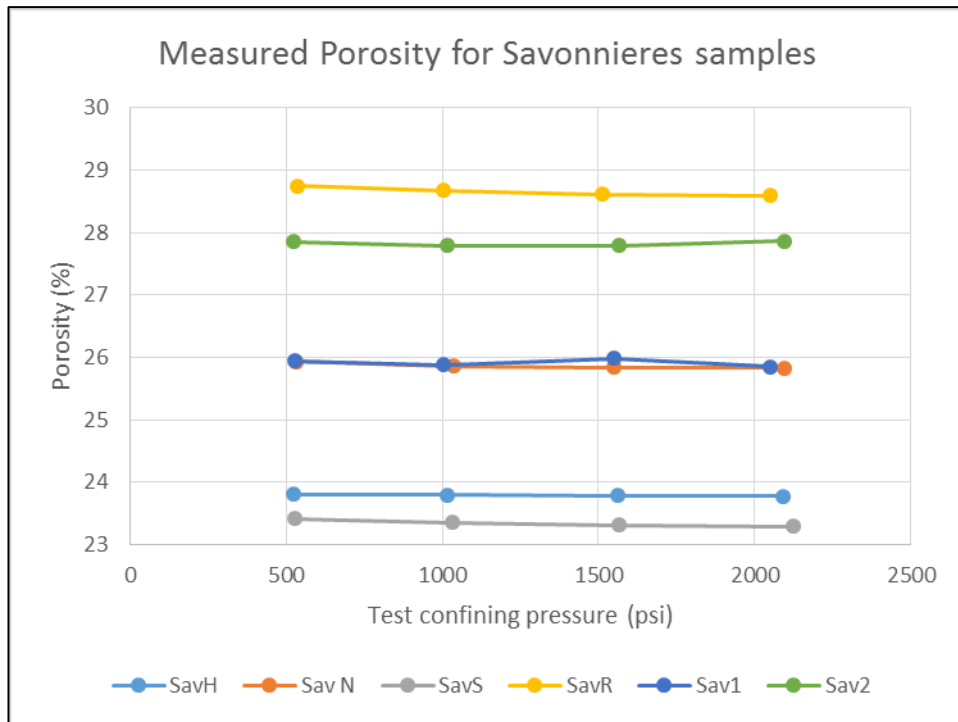


Figure 3.15 Porosity values of Savonnieres samples as measured with the AP-608 poro-permeameter

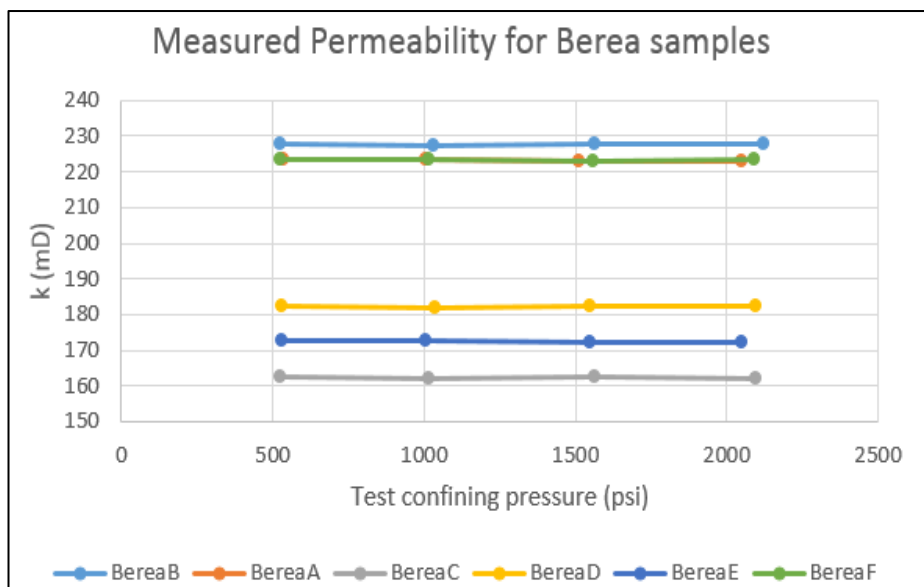


Figure 3.16 Permeability values of Berea samples as measured with the AP-608 poro-permeameter

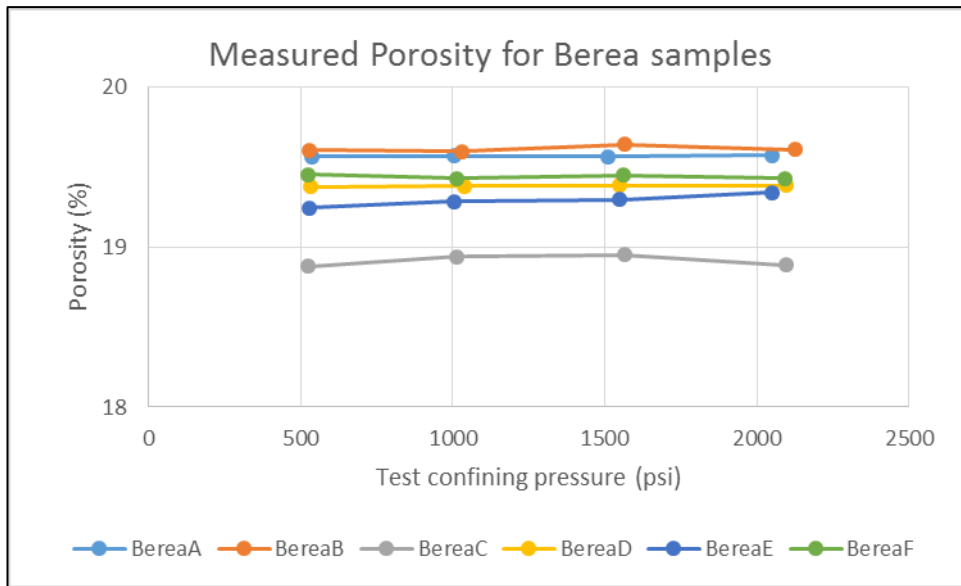


Figure 3.17 Porosity values of Berea samples as measured with the AP-608 poro-permeameter

The core samples were split into three groups. The groupings were done mainly in accordance with the type of tests conducted with the permeating fluid used. Table 3.2 shows the petro-physical characteristics of the samples in which dead brine was used as the injection fluid. Dead brine was injected initially to observe changes with a neutral pH fluid.

Table 3.2 Petrophysical properties of core samples injected with dead brine (Group 1)

Sample ID	Length (mm)	Diameter (mm)	Rock type	Mass (g)	Permeability (mD)	Porosity (%)
A	64.50	38.02	Sandstone	157.16	223.19	19.57
B	64.80	38.04	Sandstone	156.79	227.67	19.62
R	64.41	38.55	Carbonate	144.67	65.73	28.66
S	64.60	38.65	Carbonate	156.00	14.04	23.34

The second group with petro-physical characteristics as shown in Table 3.3 comprises of the samples which live brine (i.e. CO<sub>2</sub> saturated brine) was used as the injection fluid.

Table 3.3. Petrophysical properties of core samples injected with live brine (Group 2)

Sample ID	Length (mm)	Diameter (mm)	Rock type	Mass (g)	Permeability (mD)	Porosity (%)
E	64.56	37.98	Sandstone	156.07	172.44	19.29
F	64.72	38.03	Sandstone	155.99	223.27	19.44
Sav-2	64.94	38.60	Carbonate	147.80	75.75	27.83
H	64.75	38.46	Carbonate	156.49	16.20	23.79

Lastly, the core samples in group three were core flooded with supercritical CO<sub>2</sub> during testing and the initial petro-physical characteristics are as shown in Table 3.4.

Table 3.4 Petrophysical properties of core samples injected with supercritical CO<sub>2</sub> (Group 3)

Sample ID	Length (mm)	Diameter (mm)	Rock type	Mass (g)	Permeability (mD)	Porosity (%)
C	64.86	37.98	Sandstone	156.97	162.24	18.92
D	64.75	37.96	Sandstone	155.99	182.12	19.38
Sav-1	64.55	38.52	Carbonate	153.00	28.24	25.91
N	64.95	38.65	Carbonate	151.82	32.87	25.87

### 3.3.2 Fluids and salts

Sodium chloride (NaCl) and potassium chloride (KCl) salts obtained from Sigma-Aldrich™ were used in the preparation of brine solution for these tests. Considering the fact that both NaCl and KCl are PH neutral salts, hence it is assumed that the PH of the synthetic brine prepared in the lab is around 7. Also, injection rate during core flooding will be kept constant at 2cc/min, as previous studies show that there is minimal effect of flow rate variation on permeability evolution during compression tests (Al-Yaseri et al., 2017). Prior to preparation for the uses in this experiment, the fluid were sourced in their primary states as shown in Table 3.5.

Table 3.5 Experimental fluids used in for injection and sources

Fluid	Source	Physical state	Chemical state
Distilled water	David Gray	Liquid	99.9% purity
Carbon dioxide (CO <sub>2</sub> )	BOC Australia	Gas (Compressed in lab to scCO <sub>2</sub> )	99.9 purity; food grade gas code 082

### 3.4 Experimental procedure

#### 3.4.1 Dead brine preparation

The brine used for full saturation of the rock specimens before testing commenced was prepared by mixing the sodium chloride (NaCl) and potassium chloride (KCl) salts with distilled water in a bottle; to ensure complete dissolution of the salts in the distilled water, a magnetic stirrer was used to bring the solution to complete equilibrium (24hrs). This synthetic brine is used in saturating the core samples and also in the first test which involved core flooding the samples with dead brine during triaxial compression. The brine solution prepared for this experiment had a concentration of 5% NaCl, 1% KCl and 94% distilled water.

#### 3.4.2 Live brine preparation

The procedure for preparation of live brine was followed as outlined by El-Maghraby et al. (2012), who also stated that the solubility of CO<sub>2</sub> in a solution with KCl will be greater than in a solution with only NaCl. The equipment layout is shown in Figure 3.18 and includes a John Morris *Parr 4848* equilibrating reactor. This reactor combines the synthetic lab-prepared brine and pure scCO<sub>2</sub> at high mixing speed and supercritical conditions to enable complete dissolution in the brine.

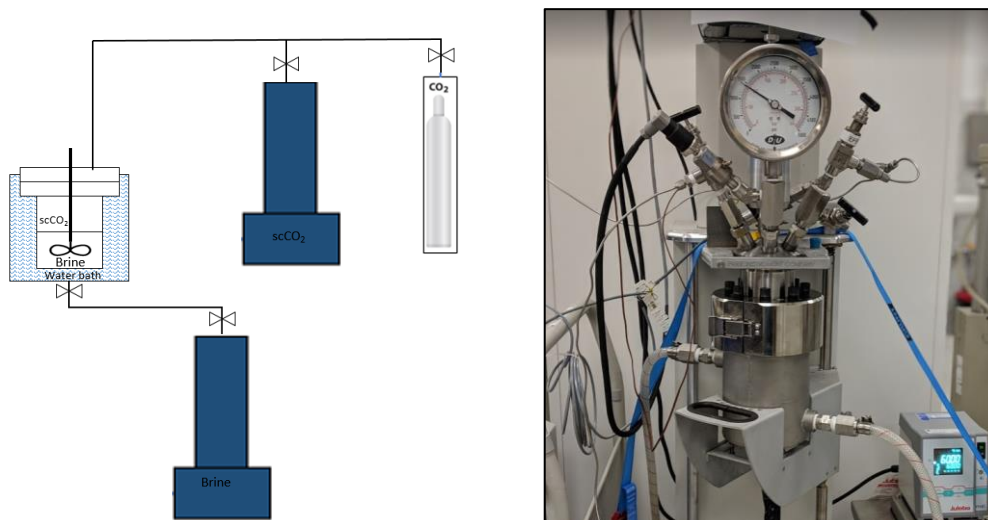


Figure 3.18 Schematic of setup for live brine preparation and close up view of reactor

- Firstly,  $\text{scCO}_2$  was prepared in one of the *ISCO 500D* high precision syringe pumps by transferring  $\text{CO}_2$  from the  $\text{CO}_2$  cylinder into the pump and compressing to supercritical pressure; the pump was also heated to  $50^\circ\text{C}$  using the heating jacket attached. Once the pump had been filled with  $\text{CO}_2$ , it was pressurized to 10MPa to make  $\text{scCO}_2$ .
- Approximately 350 cc of synthetic brine was injected into the reactor using a second syringe pump that had been filled with brine;  $\text{scCO}_2$  from the first pump was continually injected into the reactor until supercritical pressure was attained. The reactor was constantly maintained at a temperature of  $50^\circ\text{C}$  in a water bath to keep the temperature above supercritical requirement.
- The stirrer of the reactor was switched on at a speed of 200 rpm to agitate and rapidly dissolve the  $\text{CO}_2$  into the brine solution. More  $\text{CO}_2$  was continually pumped into the reactor as the  $\text{CO}_2$  dissolution in the brine progressed (indicated by a reduction in pressure). Once the  $\text{CO}_2$  volume readings attained stability, indicating no more mass transfer into the reactor, the brine was deemed fully saturated and it took approximately 60 minutes of equilibrating to attain this saturation point.
- The live brine was transferred from the reactor into the Vinci pump which had a capacity of 250cc; from the Vinci pump, it was injected at

the required flow rate into the core samples in the Hoek cell, while being maintained at supercritical pressure and temperature to prevent mass transfer between the two phases.

To minimise the risk of components separation, adequate insulation of the tubing to transport the live brine from the reactor to Vinci pump and to the Hoek cell was performed to maintain the supercritical temperature required to prevent phase separation.

### 3.4.3 Rock sample preparation

Before commencing triaxial compression and core flooding tests, the rock samples were oven-dried at 65°C for 24 hours to eliminate any fluid content within the rock pores.

For the tests involving supercritical CO<sub>2</sub> and live brine, the rock specimens were wrapped in a multilayered sleeve to prevent CO<sub>2</sub> diffusion through the confining sleeve in the Hoek cell which could damage the rubber sleeves on contact and lead to oil leak into the test sample. Firstly, the core samples were wrapped in aluminium foil, followed by a layer of Teflon tape, then another layer of aluminium foil, and lastly, in a heat shrinkable polyolefin tubing as depicted in Figure 3.19.

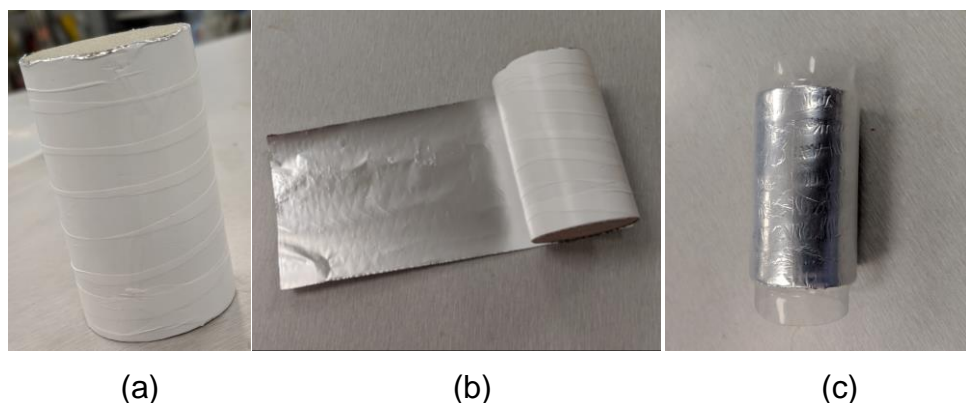


Figure 3.19 Protective wrapping of core samples in (a) teflon over aluminium foil (b) aluminium foil over teflon, and (c) polyolefin tubing as final layer prior to scCO<sub>2</sub> injection testing

### 3.4.4 Testing procedures

The sample testing will follow the specifics particular to each group based on the conditions and setup required for the different fluids used to continually remain in the expected phase. The objectives are to investigate the effect of stresses and failure on axial permeability via:

- i) Triaxial compression with dead brine injection
- ii) Triaxial compression with live brine injection
- iii) Triaxial compression with supercritical carbon dioxide (scCO<sub>2</sub>)

The difference between the major principal stress (axial) and minor principal stress (confining) is calculated as the deviatoric stress on the sample. For these experiments, triaxial compression tests are conducted from an initial isotropic stress state until the samples experience failure. During testing, confining pressure is kept constant while axial stress is gradually increased.

The below steps show the general steps followed similarly for each test conducted:

- Individual rock samples to be tested are inserted into the Hoek cell, ensuring proper placement in the middle of the cell and the end plugs fixed at both ends of the sample, and effective pressure of 2MPa was applied to eliminate leak from the sample-sleeve interface.
- Initial axial stress and confining pressure were gradually increased to 10Mpa, attaining a hydrostatic state of stress similar to *in situ* sequestration conditions. Pore pressure was also increased gradually as the overburden pressure was being increased until the desired value was reached.
- With all tubing, valves, and equipment connections confirmed tight and leak-free, the whole system is vacuumed for 24 hours to eliminate any air within the pores of the rock samples.
- Then the Vinci pump was run in constant-pressure mode to inject synthetic brine into the lines and sample for about 24hours, fully

saturating the core sample. Complete saturation was confirmed by monitoring volume stability on the syringe pump.

- For dead brine injection tests, the synthetic brine was injected directly from the Vinci syringe pump. For the tests conducted with live brine, the live brine which was prepared in the reactor and transferred into the Vinci syringe pump, it was injected into the samples and displacing the dead brine for 5 pore volumes. Supercritical carbon dioxide was prepared in the Vinci syringe pump, as mentioned earlier, by compressing CO<sub>2</sub> gas at effective pressure and temperature of 10MPa and 50°C.
- Prior to conducting the tests with live brine and scCO<sub>2</sub> injection, the oven enclosure housing the Hoek cell was heated to maintain an effective temperature of 50°C; and a Type T thermocouple was attached to the Hoek cell to verify the actual temperature of the sample during the test.
- For all three test modes, the fluid injection was programmed on the Vinci pump to operate in constant flow mode at a flow rate of 2 cc/min and approximately 10 pore volume (PV) was injected per sample. The tests were conducted at conditions representative of reservoir storage locations at 1000m depth of (10Mpa confining and 10Mpa pore pressure).
- Axial stress was programmed on the ISCO syringe pump at an incremental rate of 150 kPa/min. This gradual increment was sustained until the sample fails- indicated by a noticeable drop in axial stress recording on the logging software and a surge in the pump flow rate to attempt to restore the axial stress to the point of failure.
- At this point the valve on the axial stress line was closed off to maintain the pressure within the core sample and hold the stress from exceeding the sample critical point of fracture, hence preventing further fracture sliding.

- The injection of permeating fluid (dead brine, live brine, or scCO<sub>2</sub>) continued while monitoring the trend in pressure difference values between the inlet and outlet pressures at the sample ends. After pressure drop had stabilised, the system was depressurised and sample was removed.
- Micro CT scans were then conducted on the samples to generate 2D and 3D views of the sample, showing structural changes to the samples. A Siemens SOMATOM medical scanner was used in achieving this. By applying an energy beam of 140 kV/ 500mAs, high-resolution (0.6mm) transversal images were developed along the x, y, and z-axes.

During CO<sub>2</sub> injection into underground storage, increased pore pressure leads to rock fracture; however, similar amount of pore pressure required for fracture cannot be generated in the lab, hence axial stress is applied to aid fracture in the samples.

Figure 3.20, Figure 3.21 and Figure 3.22 show the setup for the three test groups highlighting the different modifications made to achieve the objectives for each test.

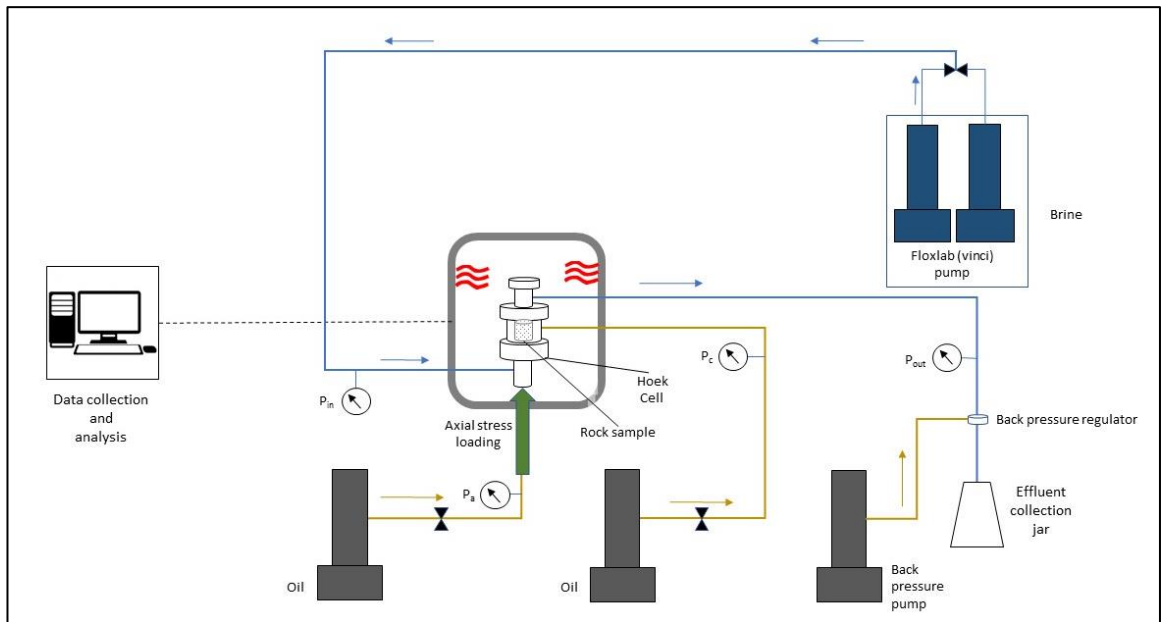


Figure 3.20 Schematic of equipment setup for permeability evolution measurement tests with unsaturated (dead) brine injected

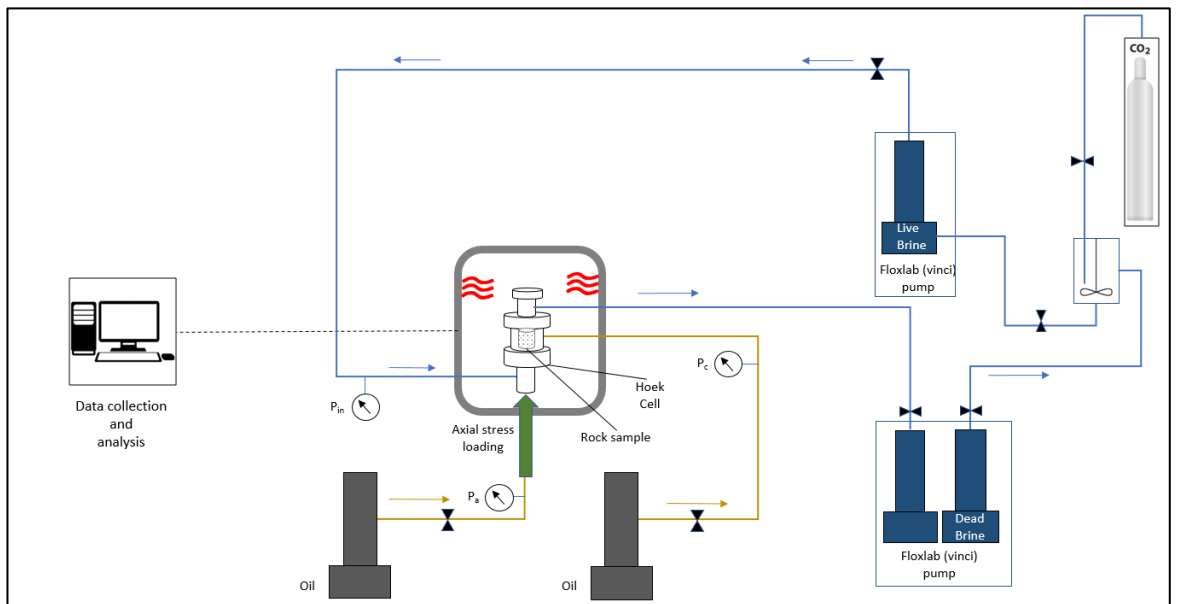


Figure 3.21 Schematic of equipment setup for permeability evolution measurement tests with live (CO<sub>2</sub> saturated) brine injected

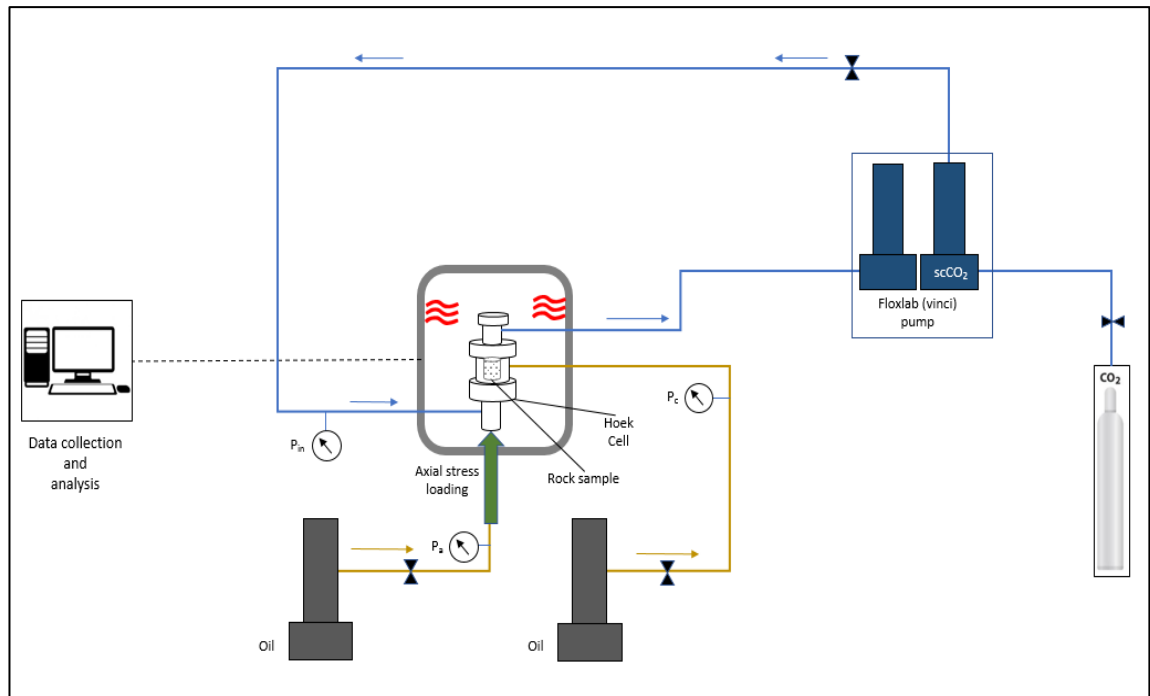


Figure 3.22 Schematic of equipment setup for permeability evolution measurement tests with supercritical carbon dioxide ( $scCO_2$ ) injected

### 3.5 Permeability Measurement and calculations

High precision pressure sensors connected to the inlet and outlet end plugs are utilised in recording pressure values and pressure drop across the sample which will be used to calculate permeability according to Darcy's law. In the laboratory, there are two methods employed in the measurement of permeability which are (i) the steady-state flow method- for permeability values  $k > 0.1mD$ , and (ii) the unsteady state method, also called pore oscillation method for values of  $k < 0.1mD$  (Fischer & Paterson, 1992; Kranz et al., 1990). In this experiment, the steady-state flow method was employed with differential pressure between the injection inlet and outlet measured to calculate the permeability evolution of the sample with continuous injection. The calculations follow the Darcy equation for permeability.

The permeability evolution is obtained by plotting the recorded trend of the pressure drop over time with increasing axial stress up until, and after, the sample experiences fracture. To determine the critical stress point of the samples, unconfined uniaxial compression tests up to failure were performed on additional samples outside of the already identified groups.

## **CHAPTER 4 RESULTS AND DISCUSSIONS**

In this chapter, the results obtained from the experiments conducted are presented and each outcome is discussed. As depicted in the experimental procedures in Chapter 3, three sets of tests were conducted as outlined, categorised using the injection fluid involved. Each set had the two types of rocks, namely Berea sandstone and Savonnières limestone, flooded during triaxial compression. The results are presented indicating the rock sample involved, injection fluid used, and stress conditions under which the tests were performed.

Worthy to note that injection of supercritical CO<sub>2</sub> or live brine into carbonate rocks may lead to geochemical reactions in addition to the geomechanical reactions which is a major mechanism in sandstone. These reactions alter the petrophysical attributes of the sample rocks via either mineral dissolution & precipitation as well as physical compaction, in addition to fines migration. And the impact varies per sample based on the amount of core heterogeneity, mineralogy, and existing fractures or microcracks.

### **4.1 Rock samples injected with dead brine**

Two (2) Berea sandstone and two (2) Savonnières limestone rock samples were experimented on with dead synthetic brine as the injection fluid. All rock samples were confined to 10MPa, axially compressed to 15MPa and maintained at a temperature of 50°C representative of reservoir conditions.

In the Berea samples, the permeability gradually decreased as the sample underwent further triaxial compression as a result of microcracks closing; a slight increase was then observed as the yield phase was being approached- attributable to a few cracks fusing to become channels and fines pushed further downstream to open the channels. As the peak stress phase is reached, the permeability remains steady and shows no further change with the plastic strain stage already attained. The results here can mainly be attributed to fines migration and the pore collapse experienced in the rock

pores. As the failure occurred, an upsurge in permeability occurred, after which the permeability remained steady in the plastic strain stage.

In the Savonnières sample flooded with unsaturated brine graphed in Figure 4.5, the permeability showed a continual decline in permeability as axial compression was gradually increased. Even after sample failure, there was no noticeable change to the trend being followed. Overall, the permeability reduced in all samples; as well, there were no indications that the permeability would alter in trend even with continued injection. The induced fracture in this sample did not shear all the way through the sample which contributed to minimal effect on permeability trend at the point of critical failure.

Overall, the samples experienced a reduction in permeability due to a combination of fines migration and pore collapse, as geochemical reactions during injection with unsaturated brine are negligible.

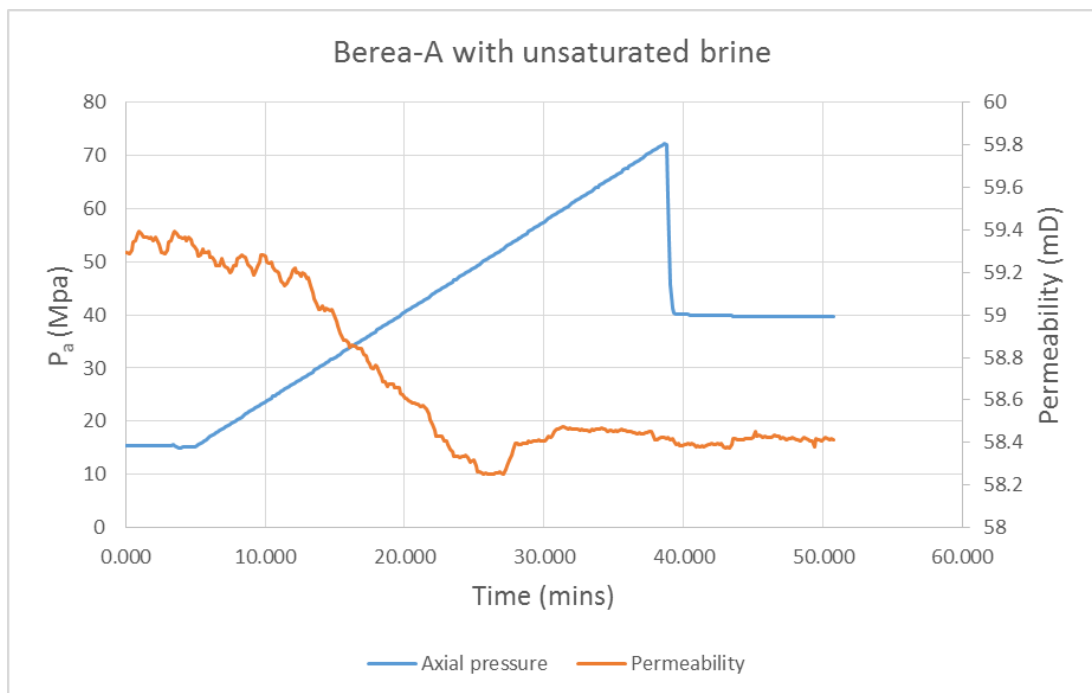


Figure 4.1 Permeability evolution observed during simultaneous flooding with unsaturated brine and triaxial loading, up to failure, of Berea Sandstone sample 'A'

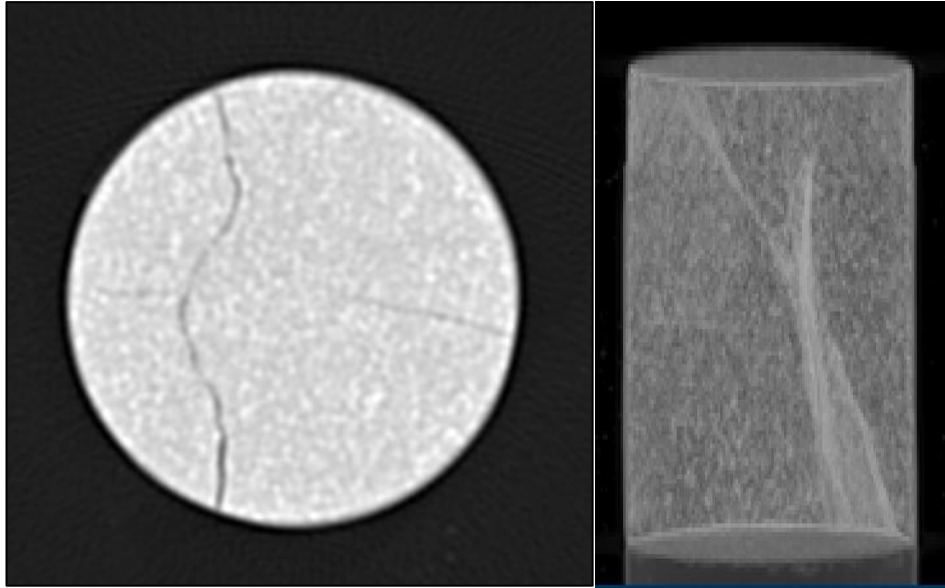


Figure 4.2 CT scan images of Berea Sandstone sample 'A' showing induced fractures across the cross-sectional area and longitudinal section after triaxial compression failure during flooding with unsaturated brine

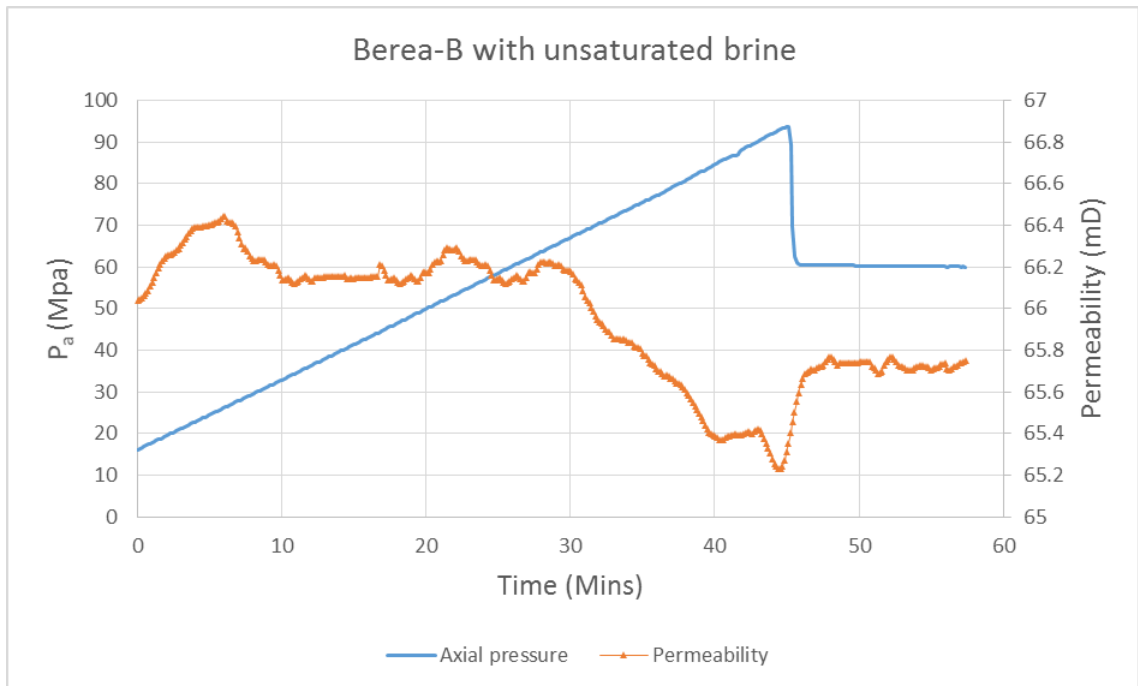


Figure 4.3 Permeability evolution observed during simultaneous flooding with unsaturated brine and triaxial loading, up to failure, of Berea Sandstone sample 'B'

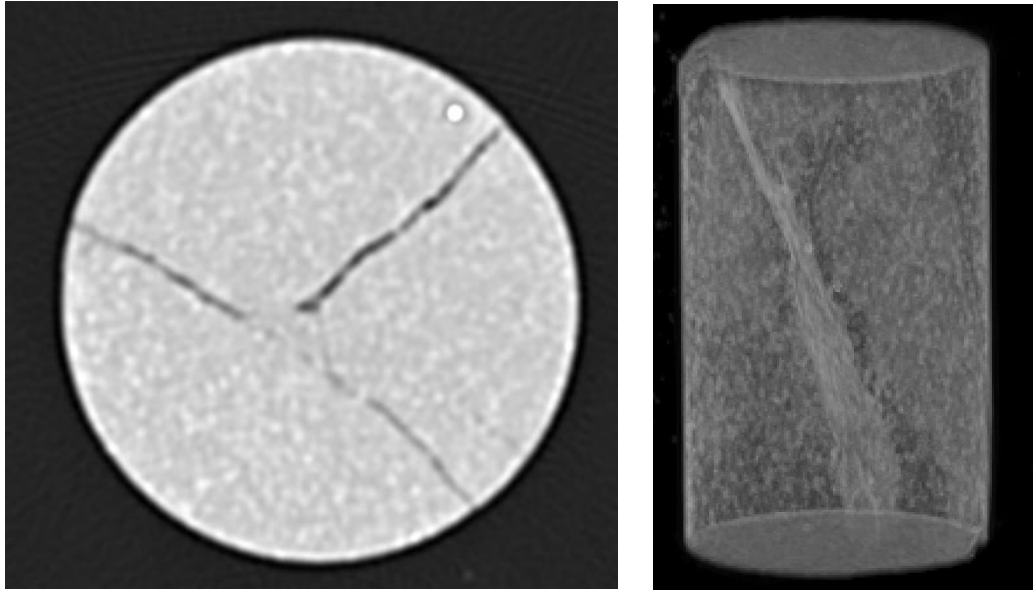


Figure 4.4 CT scan images of Berea Sandstone sample 'B' showing induced fractures across the cross-sectional area and longitudinal section after triaxial compression failure during flooding with unsaturated brine

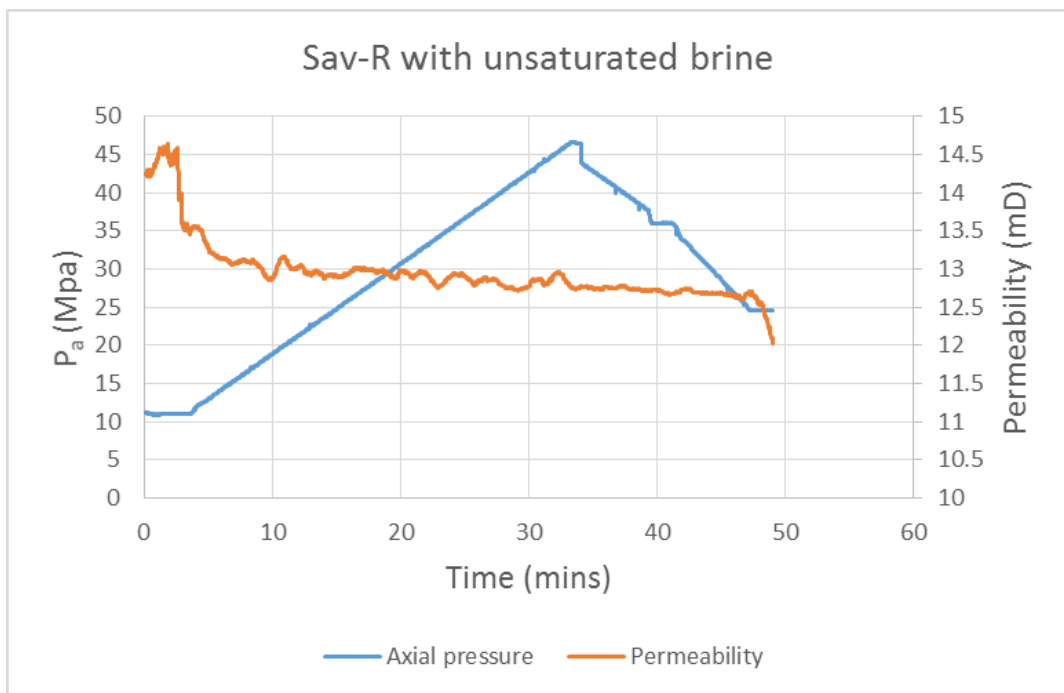


Figure 4.5 Permeability evolution during simultaneous flooding with unsaturated brine and triaxial loading, up to failure, of Savonnières limestone sample 'R'

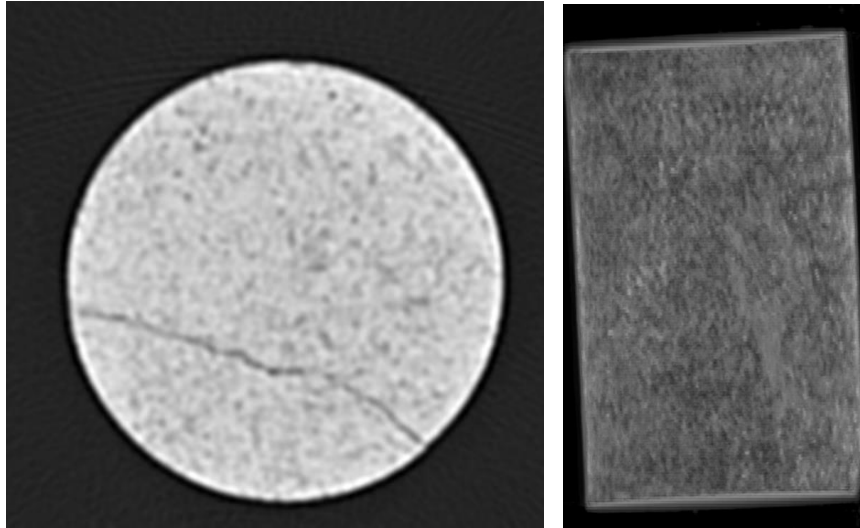


Figure 4.6 CT scan images of Savonnières limestone sample 'R' showing the induced fractures across the cross-sectional area after triaxial compression failure during flooding with unsaturated brine.

#### **4.2 Rock samples injected with CO<sub>2</sub> saturated (live) brine**

Two (2) Berea sandstone and two (2) Savonnières limestone rock samples were experimented on with saturated (CO<sub>2</sub> acidified) synthetic brine as the injection fluid.

Figures 4.7 and 4.9 show the permeability change recorded in Berea samples with live brine injected. As expected the permeability gradually reduced with progressing axial stress on the sample, evident of microcracks closure and pore compaction. As fracture is attained, there is an abrupt increase in permeability of sample 'E' as a result of a newly introduced pathway; however, sample 'F' experienced cyclic fluctuations post-fracture. As the injection is continued, the permeability decreases further and then shows indications of increasing gradually, similar to results obtained by Sayegh et al. (1990), Iglauer et al. (2014), Xu and Yang (2016) which could have been further validated with extended injection period.

At the confining pressure of 10MPa, Savonnières requires minimal stress to experience compaction due to low UCS compared to sandstone. Hence, as shown in Figure 4-11 and Figure 4-13, the Savonnières samples experienced a gradual reduction in permeability with increasing axial compression which

led to microcracks closures and pore compaction. At the point of failure, samples are moderately compacted and the fracture is shear, which doesn't create a clear pathway along the longitudinal section of the samples.

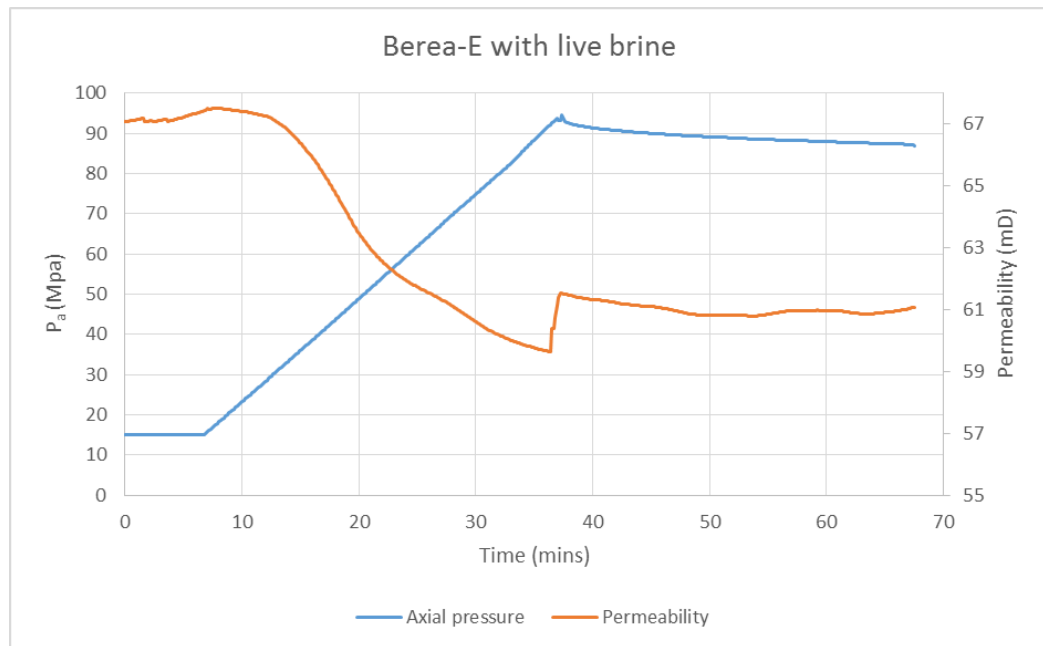


Figure 4.7 Permeability evolution observed during simultaneous flooding with live brine and triaxial loading, up to failure, of Berea Sandstone sample 'E'

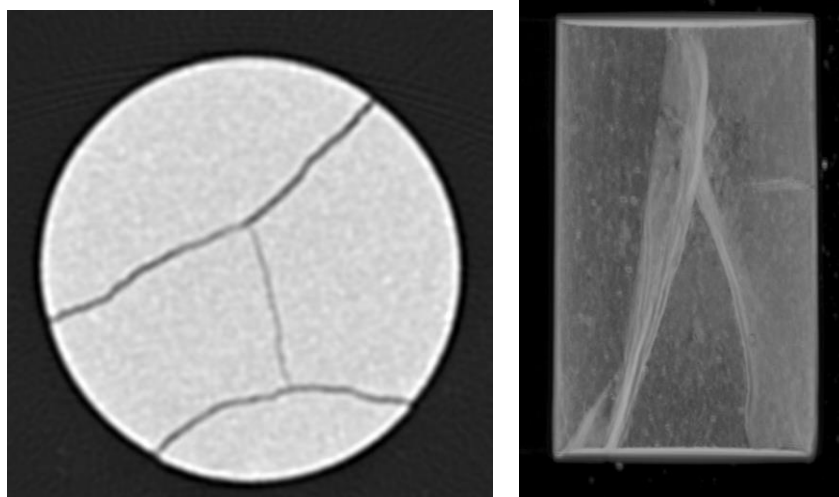


Figure 4.8 CT scan images of Berea Sandstone sample 'E' showing the induced fractures across the cross-sectional area and longitudinal section after triaxial compression failure during flooding with live brine.

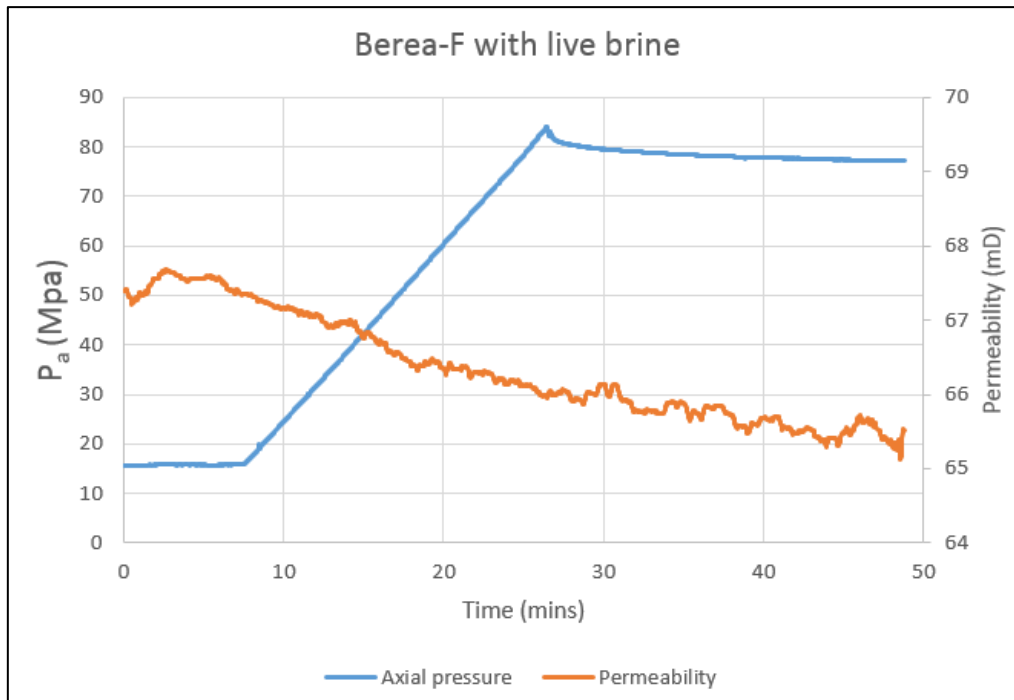


Figure 4.9 Permeability evolution observed during simultaneous flooding with live brine and triaxial loading, up to failure, of Berea Sandstone sample 'F'

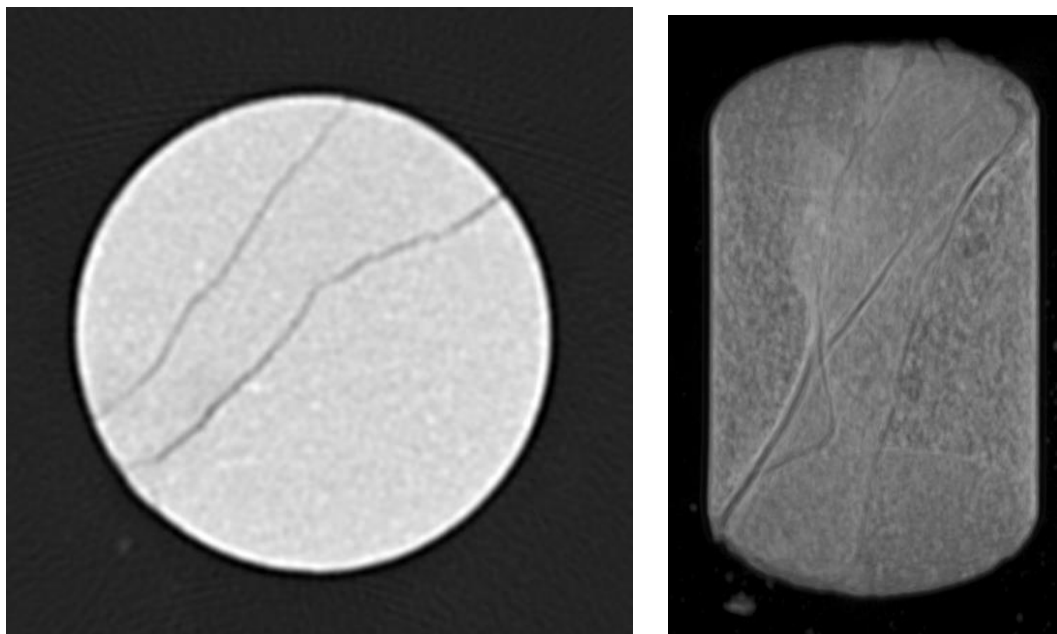


Figure 4.10 CT scan images of Berea Sandstone sample 'F' showing the induced fractures across the cross-sectional area and longitudinal section after triaxial compression failure during flooding with live brine.



Figure 4.11 Permeability evolution observed during simultaneous flooding with live brine and triaxial loading, up to failure, of Savonnières Limestone Sample '1'

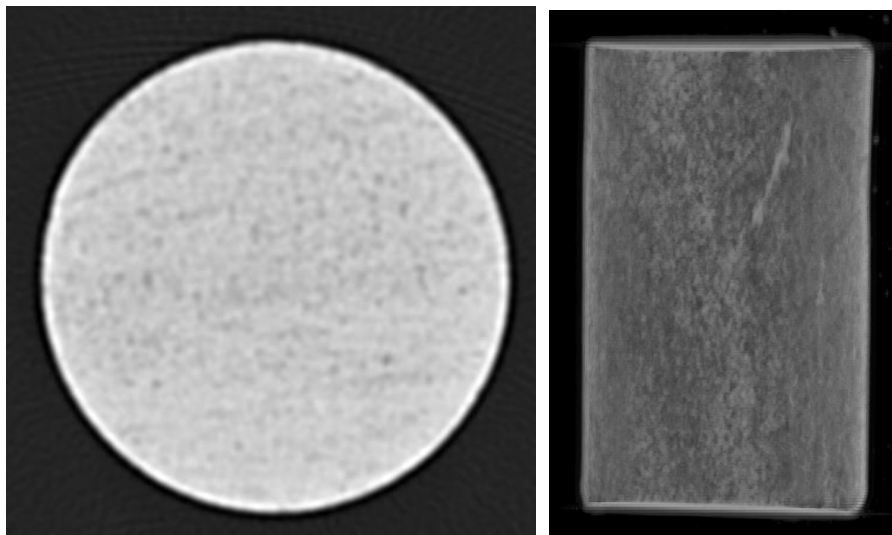


Figure 4.12 CT scan images of Savonnières Limestone Sample '1' showing a slightly induced fracture line across the cross-sectional area and longitudinal section after triaxial compression failure during flooding with live brine.



Figure 4.13 Permeability evolution observed during simultaneous flooding with live brine and triaxial loading, up to failure, of Savonnières limestone sample ‘H’

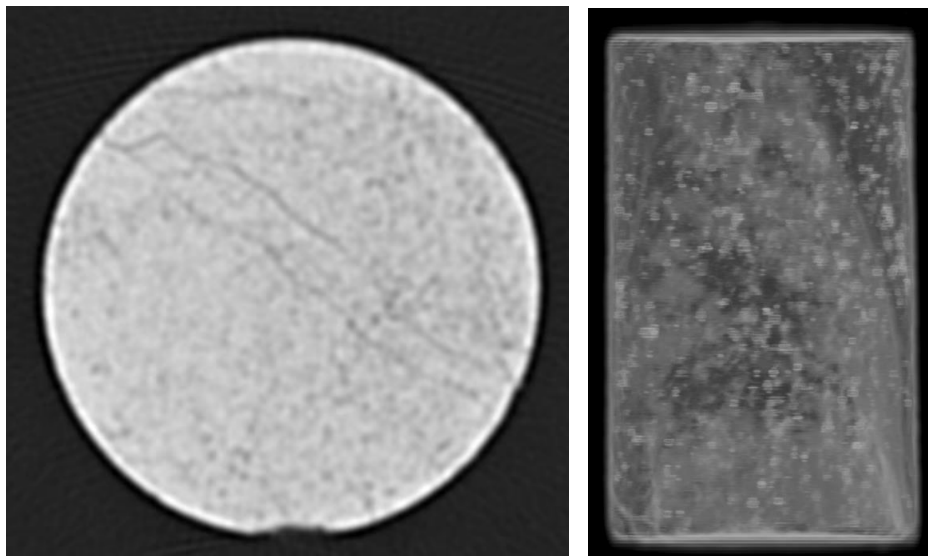


Fig 4.14 CT scan images of Savonnières limestone sample ‘H’ showing the induced fractures across the cross-sectional area and longitudinal section after triaxial compression failure during flooding with live brine.

### 4.3 Rock samples injected with supercritical carbon dioxide (scCO<sub>2</sub>)

Two (2) Berea sandstone and two (2) Savonnières limestone rock samples were experimented on with supercritical CO<sub>2</sub> as the injection fluid.

In almost all cases, a decrease in final permeability compared to permeability at the start of testing was noticed. The confining pressure placed on the samples coupled with the initial axial compression stress caused the pores and existing microcracks to close as a result of compaction. As the induced fractures occurred, there was a sharp change in the Savonnières limestone samples after which the permeability gradually increased with continued scCO<sub>2</sub> injection.

The Berea sandstone experienced a sharp decrease at the point of fracture with an alteration of permeability direction; as the stress state was maintained and scCO<sub>2</sub> injection continued, the permeability gradually increased. Table 4.1 shows the change experienced in permeability before and after the samples were fractured. It is key to point out that some of these post-fracture values were still changing when recorded and can still evolve further if the injections were executed for extended periods of time.

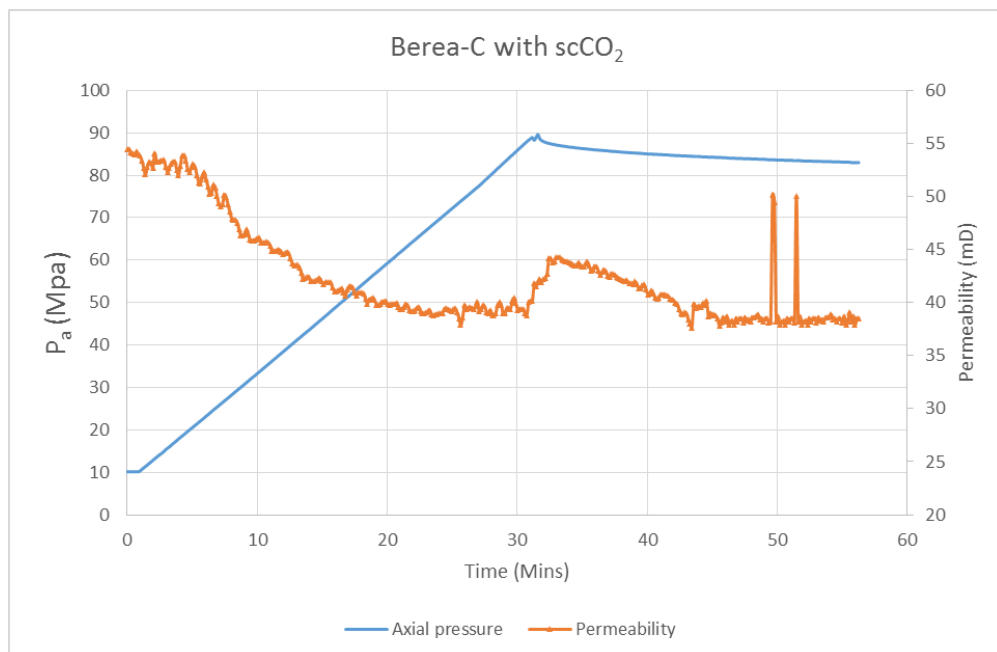


Figure 4.15 Permeability evolution observed during simultaneous flooding with supercritical CO<sub>2</sub> and triaxial loading, up to failure, of Berea Sandstone sample 'C'

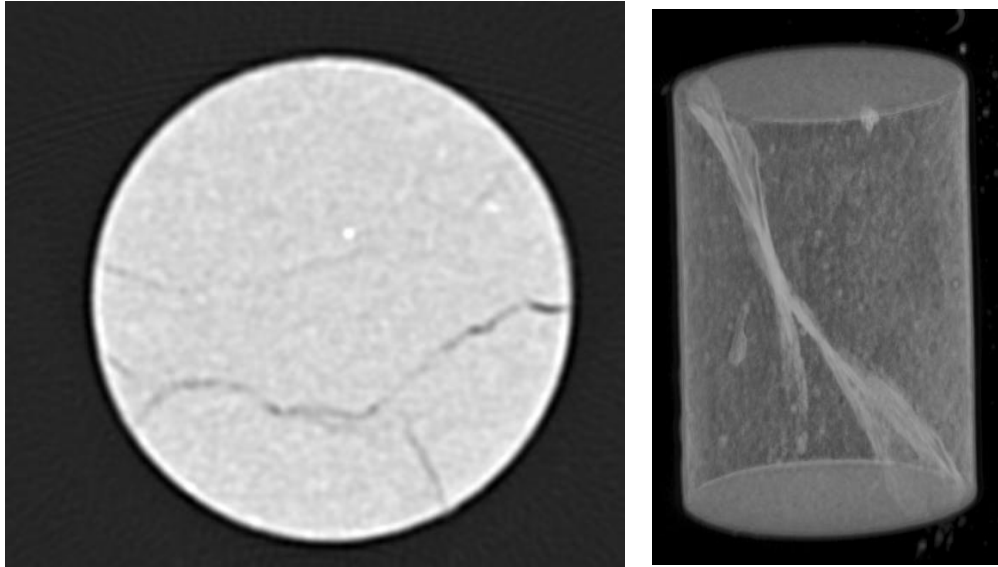


Fig 4.16 CT scan images of Berea Sandstone Sample 'C' showing the induced fractures across the cross-sectional area and longitudinal section after triaxial compression failure during flooding with supercritical carbon dioxide

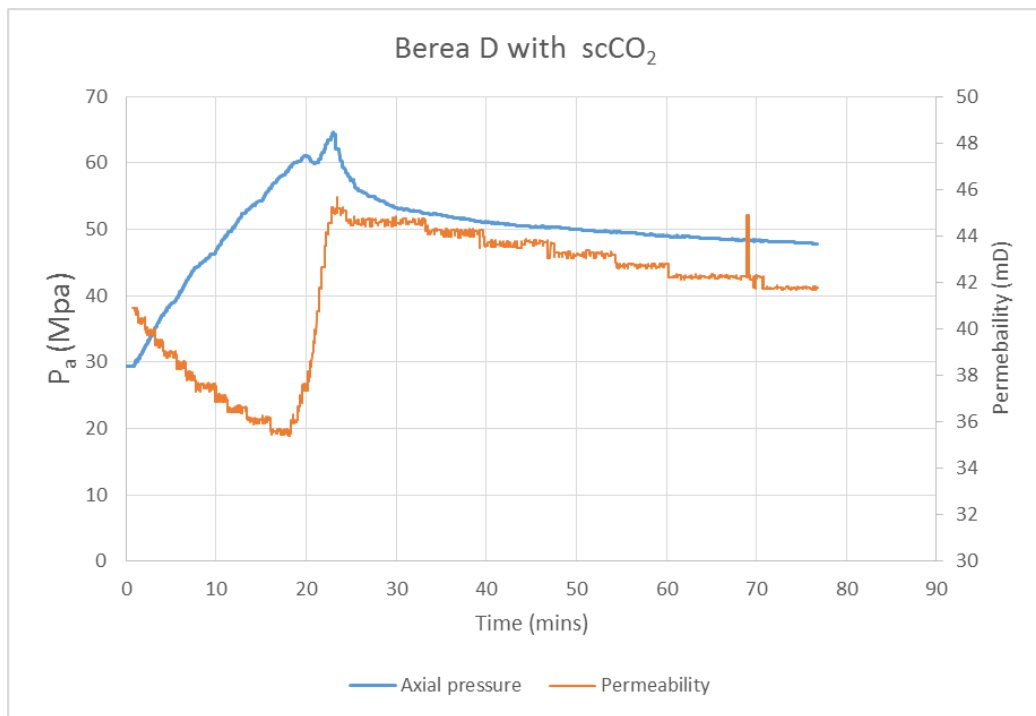


Figure 4.17 Permeability evolution observed during simultaneous flooding with supercritical CO<sub>2</sub> and triaxial loading, up to failure, of Berea Sandstone sample 'D'

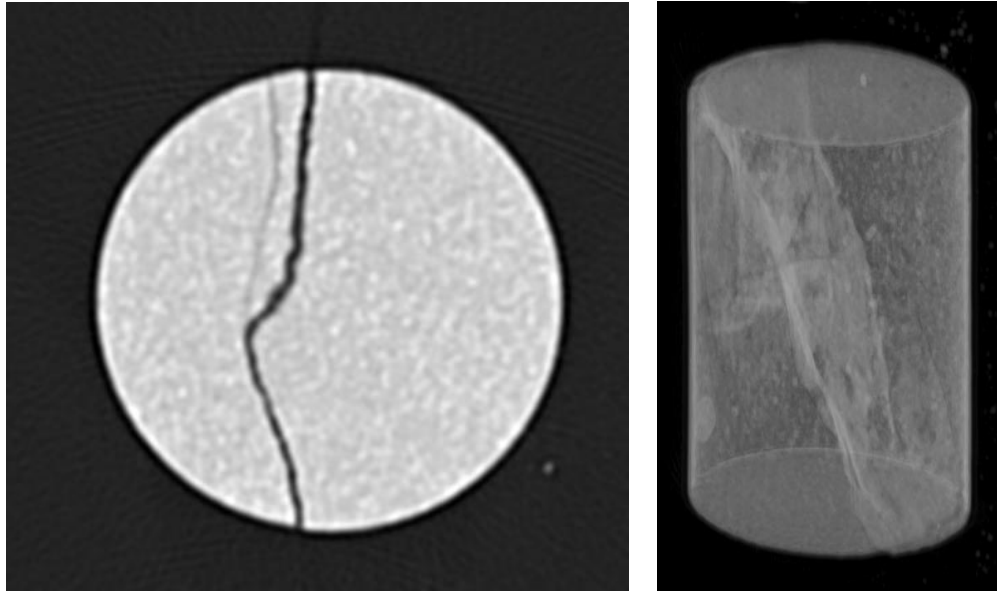


Fig 4.18 CT scan images of Berea Sandstone Sample 'D' showing the induced fractures across the cross-sectional area and longitudinal section after triaxial compression failure during flooding with supercritical carbon dioxide

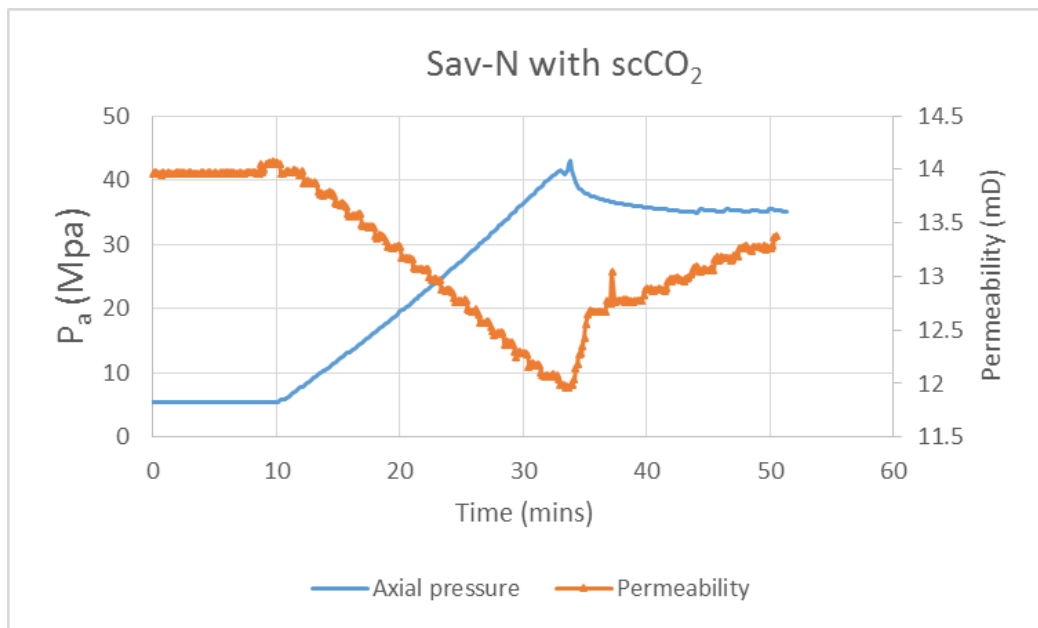


Figure 4.19 Permeability evolution observed during simultaneous flooding with supercritical  $\text{CO}_2$  and triaxial loading, up to failure, of Savonnières Limestone Sample N

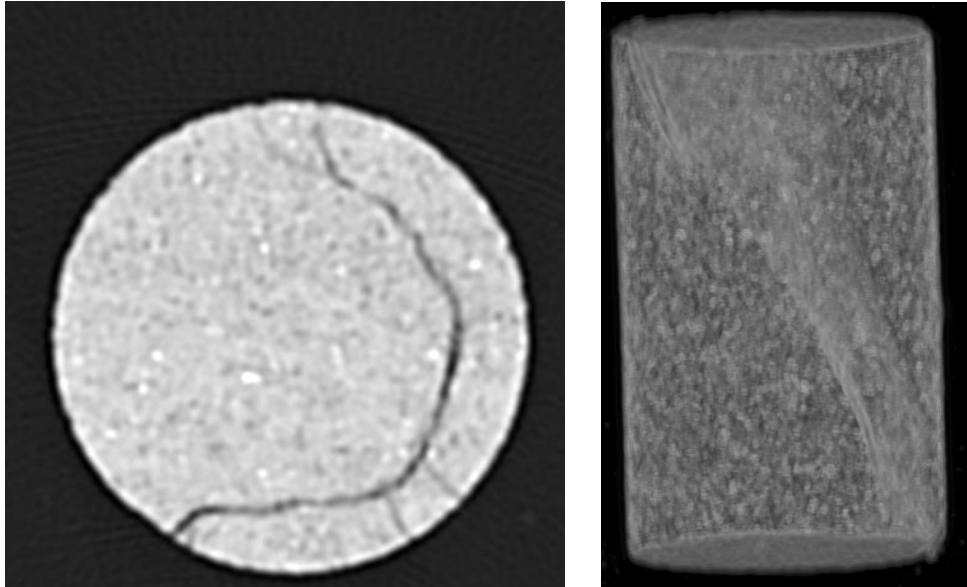


Figure 4.20 CT scan images of Savonnières sample 'N' showing the induced fractures across the cross-sectional area and longitudinal section after triaxial compression failure during flooding with supercritical carbon dioxide

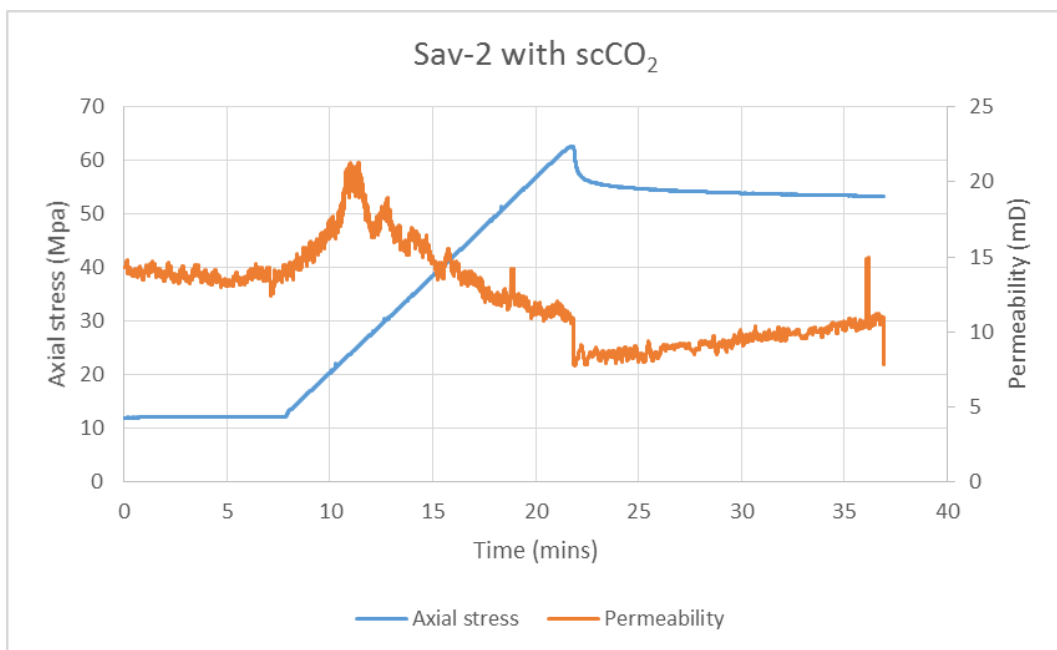


Figure 4.21 Permeability evolution observed during simultaneous flooding with supercritical CO<sub>2</sub> and triaxial loading, up to failure, of Savonnières Limestone sample '2'

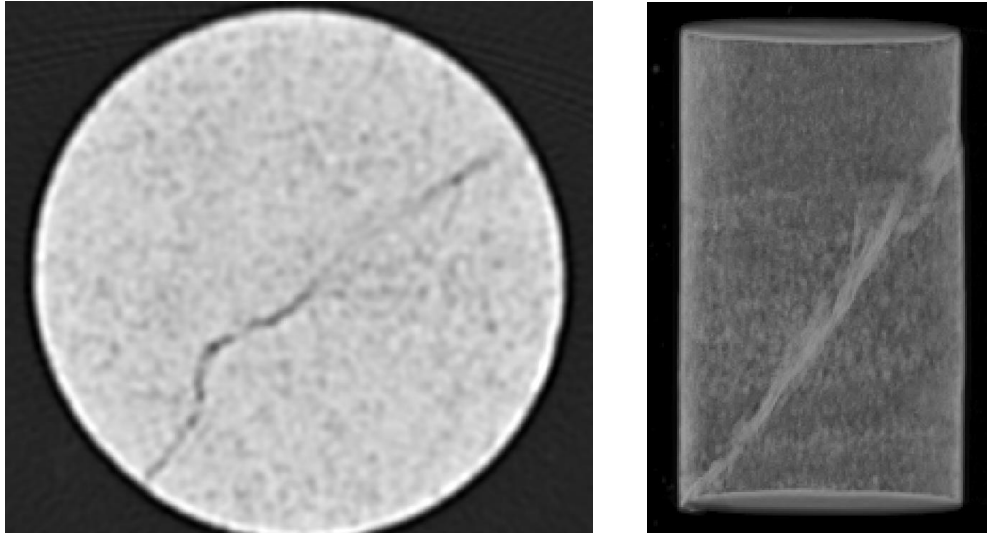


Figure 4.22 CT scan images of Savonnières sample '2' showing the induced fractures across the cross-sectional area and longitudinal section after triaxial compression failure during flooding with supercritical carbon dioxide

Figure 4.23 provides an example of the shear fractures experienced in the rocks tested.

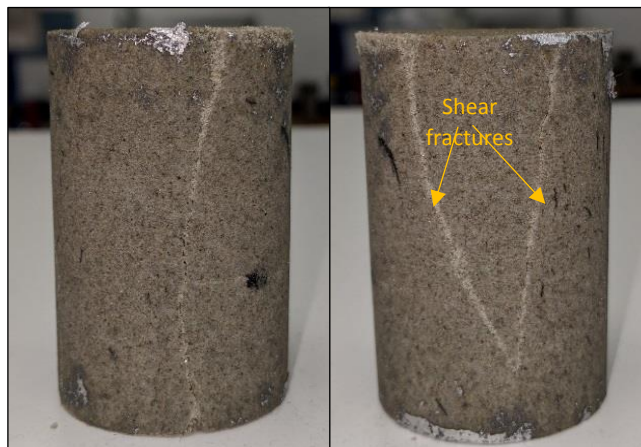


Figure 4.23 Berea sandstone after fracture showing the shear fracture and tensile crack at  $P_c = 10\text{MPa}$

#### 4.4 Permeability change in rocks post-fracture

Overall, the samples showed a reduction in permeability after completion of the triaxial compression tests and simultaneous flooding. The comparisons in Table 4.1 indicate the Savonnières limestone experiencing higher percentage difference compared to the Berea sandstone.

Table 4.1 Percentage change in permeability observed after fracture in rock samples

	Permeability at reservoir condition		
Sample ID	Pre-test	Post-test	% Change
<b>Injection with unsaturated brine</b>			
Berea A	59.3	58.4	1.51
Berea B	66.04	64.47	2.37
Sav R	14	12	14.28
<b>Injection with live brine</b>			
Berea E	67.09	60.91	9.21
Berea F	67.37	61.67	8.46
Sav H	8.11	2.32	71.39
Sav 1	20.65	14.94	27.65
<b>Injection with scCO<sub>2</sub></b>			
Berea C	54.49	38.47	29.39
Berea D	61.87	62.69	1.33
Sav 2	14.12	10.51	25.56
Sav N	13.96	12.77	8.52

## CHAPTER 5 CONCLUSION AND RECOMMENDATIONS

### 5.1 Conclusion

In this thesis, we have shown that permeability evolves during the injection of supercritical carbon dioxide or saturated brine into carbonate and sandstone rocks at reservoir conditions. The movement of fluid through the rock matrix as well as the acidic nature of the injected fluids lead to the dissolution of the bonding cement between the rock grains while also moving the particles released as fines further downstream. Counteractively, the increasing axial stress applied during testing leads to compaction reducing the available porosity and subsequently, permeability. As set out to determine, it has been shown that induced fractures as a result of increased stress in rocks impact the permeability by altering the trend immediately after fracture occurrence.

From the study carried out in this thesis, the following findings were realised:

- The geomechanical responses of carbonate rocks to the injection of supercritical carbon dioxide differs compared to sandstone rocks. For both types of rocks, permeability is reduced during triaxial compression; however, fracture occurrence produces differing results due to rock heterogeneity.
- After fracture introduction into the samples with continued injection, the Savonnières limestone rocks show an increase in permeability as mineral dissolution plays a major part in increasing existing or creating new flow channels.
- Berea sandstone rocks after fracture introduction experienced a slight decline or remained at steady values of permeability with continued injection after the initial abrupt change in the permeability. This can be attributed to fines migration and physical compaction being the major mechanisms in effect.
- Fracture occurrence in the rocks provides a temporary alteration to the rock permeability behaviour- either to improve or negatively impact permeability. The results obtained can provide insight into expected rock behaviour with fracturing to impact permeability in the desired

direction. Although, it needs to be mentioned that the fracture planes induced in the rock samples differ from those existing in natural rock reservoirs

- Most of the samples experienced fracture occurring at an angle of approximately 20-30 degrees to the direction of axial loading direction (principal acting stress,  $\sigma_1$ ); which is consistent with the expected faulting regime for a confining pressure of 10MPa (Bésuelle et al., 2000).
- In the Berea sandstone, the permeability reduced at the initial stage of progressing axial stress and then increased a little before settling at a value lower than the initial permeability before axial compression. This study is valuable as it provides insight into the permeability evolution during the stages of CO<sub>2</sub> injection and induced fracture on the permeability.

Reduction of elastic properties and pore collapse in the samples ensures the permeability values do not restore to previous values even after the triaxial compression is stopped- noticeably more in the Berea sandstone. The effect of confining pressure indicates a reduction in rock permeability; as axial stress consistently increased, the permeability decreased predictably – aligning with similar results in existing research (Al-Yaseri et al., 2017; Baud et al., 2012; Chen et al., 2017; Ding et al., 2016)

## **5.2 Recommendations**

The studies conducted have proven valuable and align with existing research, mentioned above, on the subject. Nevertheless, the following points are recommended to improve on findings obtained from this study.

Further investigation can be carried out to provide additional knowledge on the effect of the fracture permeability with extended injection times, as the fracture asperities provide new surface for geochemical and geomechanical reactions. The permeability evolution measured over a longer time with continued fluid flow through the fractures can provide knowledge on morphological changes

due to fracture introduction; as well, simulation models can be used to scale-up the effect of injection induced fractures relative to volumes obtained in actual reservoir storage sites. Lastly, constant flow rates were maintained across all the experimental tests in this research; studies considering different flow rates can be employed to evaluate the impact on post-fracture reservoir permeability.

## REFERENCES

- Akbar, M., Vissapragada, B., Alghamdi, A. H., Allen, D., Herron, M., Carnegie, A., . . . Saxena, K. (2000). *A Snapshot of Carbonate Reservoir Evaluation* (Vol. 12).
- Al-Khdheawi, E. A., Vialle, S., Barifcani, A., Sarmadivaleh, M., & Iglauer, S. (2017). Impact of reservoir wettability and heterogeneity on CO<sub>2</sub>-plume migration and trapping capacity. *International Journal of Greenhouse Gas Control*, *58*, 142-158.  
doi:<https://doi.org/10.1016/j.ijggc.2017.01.012>
- Al-Yaseri, A., Zhang, Y., Ghasemiziarani, M., Sarmadivaleh, M., Lebedev, M., Roshan, H., & Iglauer, S. (2017). Permeability Evolution in Sandstone Due to CO<sub>2</sub> Injection. *Energy & Fuels*, *31*(11), 12390-12398. doi:10.1021/acs.energyfuels.7b01701
- Alam, A. K. M. B., Niioka, M., Fujii, Y., Fukuda, D., & Kodama, J.-i. (2014). Effects of confining pressure on the permeability of three rock types under compression. *International Journal of Rock Mechanics and Mining Sciences*, *65*, 49-61.  
doi:<http://dx.doi.org/10.1016/j.ijrmms.2013.11.006>
- Aydin, G., Karakurt, I., & Aydiner, K. (2010). Evaluation of geologic storage options of CO<sub>2</sub>: Applicability, cost, storage capacity and safety. *Energy Policy*, *38*(9), 5072-5080.  
doi:<https://doi.org/10.1016/j.enpol.2010.04.035>
- Azin, R., Mehrabi, N., Osfouri, S., & Asgari, M. (2015). Experimental Study of CO<sub>2</sub> – Saline Aquifer-Carbonate Rock Interaction during CO<sub>2</sub> Sequestration. *Procedia Earth and Planetary Science*, *15*, 413-420. doi:<http://dx.doi.org/10.1016/j.proeps.2015.08.023>
- Bachu, S. (2000). Sequestration of CO<sub>2</sub> in geological media: criteria and approach for site selection in response to climate change. *Energy Conversion and Management*, *41*(9), 953-970. doi:[http://dx.doi.org/10.1016/S0196-8904\(99\)00149-1](http://dx.doi.org/10.1016/S0196-8904(99)00149-1)
- Bachu, S., & Adams, J. J. (2003). Sequestration of CO<sub>2</sub> in geological media in response to climate change: capacity of deep saline aquifers to sequester CO<sub>2</sub> in solution. *Energy Conversion and Management*, *44*(20), 3151-3175.  
doi:[https://doi.org/10.1016/S0196-8904\(03\)00101-8](https://doi.org/10.1016/S0196-8904(03)00101-8)
- Bachu, S., Gunter, W. D., & Perkins, E. H. (1994). Aquifer disposal of CO<sub>2</sub>: Hydrodynamic and mineral trapping. *Energy Conversion and Management*, *35*(4), 269-279.  
doi:[https://doi.org/10.1016/0196-8904\(94\)90060-4](https://doi.org/10.1016/0196-8904(94)90060-4)
- Baud, P., Meredith, P., & Townend, E. (2012). Permeability evolution during triaxial compaction of an anisotropic porous sandstone. *Journal of Geophysical Research: Solid Earth*, *117*(B5). doi:10.1029/2012jb009176
- Beard, D., & Weyl, P. (1973). Influence of texture on porosity and permeability of unconsolidated sand. *AAPG bulletin*, *57*(2), 349-369.
- Benson, S. M., & Cole, D. R. (2008). CO<sub>2</sub> Sequestration in Deep Sedimentary Formations. *Elements*, *4*(5), 325.
- Bentham, M., & Kirby, M. (2005). CO<sub>2</sub> Storage in Saline Aquifers. *Oil & Gas Science and Technology - Rev. IFP*, *60*(3), 559-567.
- Bera, B., Mitra, S. K., & Vick, D. (2011). Understanding the micro structure of Berea Sandstone by the simultaneous use of micro-computed tomography (micro-CT) and focused ion beam-scanning electron microscopy (FIB-SEM). *Micron*, *42*(5), 412-418.  
doi:<https://doi.org/10.1016/j.micron.2010.12.002>
- Bert, M., Ogunlade, D., Heleen de, C., Manuela, L., & Leo, M. (2005). *IPCC special report on carbon dioxide capture and storage*. United States: Cambridge University Press, New York, NY (United States).
- Bésuelle, P., Desrues, J., & Raynaud, S. (2000). Experimental characterisation of the localisation phenomenon inside a Vosges sandstone in a triaxial cell. *International Journal of Rock Mechanics and Mining Sciences*, *37*(8), 1223-1237.  
doi:[https://doi.org/10.1016/S1365-1609\(00\)00057-5](https://doi.org/10.1016/S1365-1609(00)00057-5)

- Biddle, K. T., & Wielchowsky, C. C. (1994). Hydrocarbon Traps: Chapter 13: Part III. Processes.
- Bieniawski, Z., & Bernede, M. (1979). *Suggested methods for determining the uniaxial compressive strength and deformability of rock materials: Part 1. Suggested method for determining deformability of rock materials in uniaxial compression*. Paper presented at the International Journal of Rock Mechanics and Mining Sciences & Geomechanics Abstracts.
- Bjørlykke, K., & Jahren, J. (2010). Sandstones and Sandstone Reservoirs. In K. Bjørlykke (Ed.), *Petroleum Geoscience: From Sedimentary Environments to Rock Physics* (pp. 113-140). Berlin, Heidelberg: Springer Berlin Heidelberg.
- Bui, M., Adjiman, C. S., Bardow, A., Anthony, E. J., Boston, A., Brown, S., . . . Mac Dowell, N. (2018). Carbon capture and storage (CCS): the way forward. *Energy & Environmental Science*, 11(5), 1062-1176. doi:10.1039/C7EE02342A
- C170/170M-16, A. (2016). Standard test method for compressive strength of dimension stone. In *ASTM C170/170M-16*.
- Cargill, J. S., & Shakoor, A. (1990). Evaluation of empirical methods for measuring the uniaxial compressive strength of rock. *International Journal of Rock Mechanics and Mining Sciences and Geomechanics Abstracts*, 27(6), 495-503. doi:10.1016/0148-9062(90)91001-N
- Chapman, S. A., Tisato, N., Quintal, B., & Holliger, K. (2015). Laboratory measurements of seismic wave attenuation in Berea sandstone as a function of water saturation and confining pressure. In *SEG Technical Program Expanded Abstracts 2015* (pp. 3079-3084).
- Chau, K., & Wong, R. (1996). *Uniaxial compressive strength and point load strength of rocks*. Paper presented at the International Journal of Rock Mechanics and Mining Sciences & Geomechanics Abstracts.
- Chen, X., Yu, J., Tang, C. a., Li, H., & Wang, S. (2017). Experimental and Numerical Investigation of Permeability Evolution with Damage of Sandstone Under Triaxial Compression. *Rock Mechanics and Rock Engineering*, 50(6), 1529-1549. doi:10.1007/s00603-017-1169-3
- Choi, C. S., Cheon, D. S., & Song, J. J. (2017). Effect of pore and confining pressure on the supercritical CO<sub>2</sub> permeability of sandstone: Implications for the effective pressure law. *Journal of Geophysical Research: Solid Earth*, 122(8), 6231-6246. doi:10.1002/2017jb014475
- Churcher, P. L., French, P. R., Shaw, J. C., & Schramm, L. L. (1991). *Rock Properties of Berea Sandstone, Baker Dolomite, and Indiana Limestone*. Paper presented at the Proceedings of the 1991 SPE International Symposium on Oilfield Chemistry, Anaheim, Feb. 20–22.
- Cook, P. J. (2013). 11 - The CO<sub>2</sub>CRC Otway Project in Australia. In J. Gluyas & S. Mathias (Eds.), *Geological Storage of Carbon Dioxide (CO<sub>2</sub>)* (pp. 251-277): Woodhead Publishing.
- Coskun, S. B., Wardlaw, N. C., & Haverslew, B. (1993). Effects of composition, texture and diagenesis on porosity, permeability and oil recovery in a sandstone reservoir. *Journal of Petroleum Science and Engineering*, 8(4), 279-292. doi:[https://doi.org/10.1016/0920-4105\(93\)90005-Y](https://doi.org/10.1016/0920-4105(93)90005-Y)
- David, C., Menendez, B., Zhu, W., & Wong, T. f. (2001). Mechanical compaction, microstructures and permeability evolution in sandstones. *Physics and Chemistry of the Earth, Part A: Solid Earth and Geodesy*, 26(1), 45-51. doi:[https://doi.org/10.1016/S1464-1895\(01\)00021-7](https://doi.org/10.1016/S1464-1895(01)00021-7)
- De Silva, P. N. K., & Ranjith, P. G. (2012). A study of methodologies for CO<sub>2</sub> storage capacity estimation of saline aquifers. *Fuel*, 93, 13-27. doi:<https://doi.org/10.1016/j.fuel.2011.07.004>

- Dehler, W., & Labuz, J. F. (2007). Stress path testing of an anisotropic sandstone. *Journal of geotechnical and geoenvironmental engineering*, 133(1), 116-119.
- Delle Piane, C., & Sarout, J. (2016). Effects of water and supercritical CO<sub>2</sub> on the mechanical and elastic properties of Berea sandstone. *International Journal of Greenhouse Gas Control*, 55, 209-220. doi:10.1016/j.ijggc.2016.06.001
- Dewanckele, J., De Kock, T., Fronteau, G., Derluyn, H., Vontobel, P., Dierick, M., . . . Cnudde, V. (2014). Neutron radiography and X-ray computed tomography for quantifying weathering and water uptake processes inside porous limestone used as building material. *Materials Characterization*, 88, 86-99.  
doi:<https://doi.org/10.1016/j.matchar.2013.12.007>
- Ding, Q.-L., Ju, F., Song, S.-B., Yu, B.-Y., & Ma, D. (2016). An experimental study of fractured sandstone permeability after high-temperature treatment under different confining pressures. *Journal of Natural Gas Science and Engineering*, 34, 55-63.  
doi:<http://dx.doi.org/10.1016/j.jngse.2016.06.034>
- Eiken, O., Ringrose, P., Hermanrud, C., Nazarian, B., Torp, T. A., & Høier, L. (2011). Lessons learned from 14 years of CCS operations: Sleipner, In Salah and Snøhvit. *Energy Procedia*, 4, 5541-5548. doi:<https://doi.org/10.1016/j.egypro.2011.02.541>
- El-Maghraby, R. M., Pentland, C. H., Iglauer, S., & Blunt, M. J. (2012). A fast method to equilibrate carbon dioxide with brine at high pressure and elevated temperature including solubility measurements. *The Journal of Supercritical Fluids*, 62, 55-59.  
doi:<https://doi.org/10.1016/j.supflu.2011.11.002>
- Ennis-King, J. P., & Paterson, L. (2005). Role of Convective Mixing in the Long-Term Storage of Carbon Dioxide in Deep Saline Formations. *SPE Journal*, 10(03), 349-356.  
doi:10.2118/84344-PA
- Espinoza, D. N., Kim, S. H., & Santamarina, J. C. (2011). CO<sub>2</sub> geological storage — Geotechnical implications. *KSCE Journal of Civil Engineering*, 15(4), 707-719.  
doi:10.1007/s12205-011-0011-9
- Falkowski, P., Scholes, R. J., Boyle, E., Canadell, J., Canfield, D., Elser, J., . . . Steffen, W. (2000). The Global Carbon Cycle: A Test of Our Knowledge of Earth as a System. *Science*, 290(5490), 291.
- Fatt, I., & Davis, D. H. (1952). Reduction in Permeability With Overburden Pressure. *Journal of Petroleum Technology*, 4(12), 16-16. doi:10.2118/952329-G
- Fischer, G. J., & Paterson, M. S. (1992). Chapter 9 Measurement of Permeability and Storage Capacity in Rocks During Deformation at High Temperature and Pressure. *International Geophysics*, 51, 213-252. doi:[http://dx.doi.org/10.1016/S0074-6142\(08\)62824-7](http://dx.doi.org/10.1016/S0074-6142(08)62824-7)
- Fischer, S., Liebscher, A., & Wandrey, M. (2010). CO<sub>2</sub>-brine-rock interaction — First results of long-term exposure experiments at in situ P-T conditions of the Ketzin CO<sub>2</sub> reservoir. *Chemie der Erde - Geochemistry*, 70(Supplement 3), 155-164.  
doi:<https://doi.org/10.1016/j.chemer.2010.06.001>
- Flügel, E. (2013). *Microfacies of carbonate rocks: analysis, interpretation and application*: Springer Science & Business Media.
- Frailey, S. M., & Leetaru, H. (2009). Geological factors affecting CO<sub>2</sub> plume distribution. *Energy Procedia*, 1(1), 3107-3112.  
doi:<https://doi.org/10.1016/j.egypro.2009.02.091>
- Fronteau, G., Schneider-Thomachot, C., Chopin, E., Barbin, V., Mouze, D., & Pascal, A. (2010). Black-crust growth and interaction with underlying limestone microfacies. In R. Prikryl & A. Torok (Eds.), *Natural Stone Resources for Historical Monuments* (Vol. 333, pp. 25-34). Bath: Geological Soc Publishing House.
- Gatelier, N., Pellet, F., & Loret, B. (2002). Mechanical damage of an anisotropic porous rock in cyclic triaxial tests. *International Journal of Rock Mechanics and Mining Sciences*, 39(3), 335-354.

- Gaus, I., Audigane, P., André, L., Lions, J., Jacquemet, N., Durst, P., . . . Azaroual, M. (2008). Geochemical and solute transport modelling for CO<sub>2</sub> storage, what to expect from it? *International Journal of Greenhouse Gas Control*, 2(4), 605-625. doi:<https://doi.org/10.1016/j.ijggc.2008.02.011>
- Ghabezloo, S., Sulem, J., Guédon, S., & Martineau, F. (2009). Effective stress law for the permeability of a limestone. *International Journal of Rock Mechanics and Mining Sciences*, 46(2), 297-306. doi:<https://doi.org/10.1016/j.ijrmms.2008.05.006>
- Gray, D. H., & Fatt, I. (1963). The Effect of Stress on Permeability of Sandstone Cores. *Society of Petroleum Engineers Journal*, 3(02), 95-100. doi:10.2118/531-PA
- Hawkins, A. (1998). Aspects of rock strength. *Bulletin of Engineering Geology and the Environment*, 57(1), 17-30.
- He, X., Xu, C., Peng, K., & Huang, G. (2017). Simultaneous Identification of Rock Strength and Fracture Properties Via Scratch Test. *Rock Mechanics and Rock Engineering*, 50(8), 2227-2234. doi:10.1007/s00603-017-1224-0
- Heiland, J. (2003). Permeability of Triaxially Compressed Sandstone: Influence of Deformation and Strain-rate on Permeability. In H.-J. Kümpel (Ed.), *Thermo-Hydro-Mechanical Coupling in Fractured Rock* (pp. 889-908). Basel: Birkhäuser Basel.
- Hendriks, C. A., & Blok, K. (1993). Underground storage of carbon dioxide. *Energy Conversion and Management*, 34(9), 949-957. doi:[http://dx.doi.org/10.1016/0196-8904\(93\)90041-8](http://dx.doi.org/10.1016/0196-8904(93)90041-8)
- Hesse, M. A., Orr, F. M., & Tchelepi, H. A. (2008). Gravity currents with residual trapping. *Journal of Fluid Mechanics*, 611, 35-60. doi:10.1017/S002211200800219X
- Hobbs, D. W. (1964). A simple method for assessing the uniaxial compressive strength of rock. *International Journal of Rock Mechanics and Mining Sciences & Geomechanics Abstracts*, 1(1), 5-15. doi:[https://doi.org/10.1016/0148-9062\(64\)90066-X](https://doi.org/10.1016/0148-9062(64)90066-X)
- Holloway, S., & van der Straaten, R. (1995). The Joule II project the underground disposal of carbon dioxide. *Energy Conversion and Management*, 36(6), 519-522. doi:[https://doi.org/10.1016/0196-8904\(95\)00057-K](https://doi.org/10.1016/0196-8904(95)00057-K)
- IEA. (2017). *CO<sub>2</sub> Emissions From Fuel Combustion: Overview*. Retrieved from <https://www.iea.org/publications/freepublications/publication/CO2EmissionsFromFuelCombustion2017Overview.pdf>
- IEA. (2018). *Global Energy & CO<sub>2</sub> Status Report*. Retrieved from [https://webstore.iea.org/download/direct/2461?fileName=Global\\_Energy\\_and\\_CO2\\_Status\\_Report\\_2018.pdf](https://webstore.iea.org/download/direct/2461?fileName=Global_Energy_and_CO2_Status_Report_2018.pdf)
- IEA. (2020). *Global Energy Review 2020*. Retrieved from <https://www.iea.org/reports/global-energy-review-2020>
- Iglauer, S. (2011). Dissolution trapping of carbon dioxide in reservoir formation brine—a carbon storage mechanism. In *Mass transfer-advanced aspects*: InTechOpen.
- Iglauer, S., Sarmadivaleh, M., Al-Yaseri, A., & Lebedev, M. (2014). Permeability evolution in sandstone due to injection of CO<sub>2</sub>-saturated brine or supercritical CO<sub>2</sub> at reservoir conditions. *Energy Procedia*, 63, 3051-3059. doi:<http://dx.doi.org/10.1016/j.egypro.2014.11.328>
- IPCC. (2005). *IPCC—Intergovernmental Panel on Climate Change* (C. Cambridge University Press, UK and New York, NY, USA Ed.): IPCC—Intergovernmental Panel on Climate Change.
- IPCC, I. (2006). Guidelines for national greenhouse gas inventories. *Prepared by the National Greenhouse Gas Inventories Programme. Eggleston HS, Buendia L, Miwa K, Ngara T, Tanabe K, editors. Published: IGES, Japan.*
- Izgec, O., Demiral, B., Bertin, H., & Akin, S. (2008). CO<sub>2</sub> injection into saline carbonate aquifer formations I: Laboratory investigation. *Transport in Porous Media*, 72(1), 1-24. doi:10.1007/s11242-007-9132-5

- Juanes, R., Spiteri, E. J., Orr Jr, F. M., & Blunt, M. J. (2006). Impact of relative permeability hysteresis on geological CO<sub>2</sub> storage. *Water Resources Research*, 42(12). doi:10.1029/2005WR004806
- Khilar, K. C., & Fogler, H. S. (1984). The existence of a critical salt concentration for particle release. *Journal of Colloid and Interface Science*, 101(1), 214-224. doi:[https://doi.org/10.1016/0021-9797\(84\)90021-3](https://doi.org/10.1016/0021-9797(84)90021-3)
- Kim, E., Stine, M., & Martins de Oliveira, D. (2019). Effects of water content and loading rate on the mechanical properties of Berea Sandstone. *Journal of the Southern African Institute of Mining and Metallurgy*, 119(12), 1077-1082.
- Kim, K., Vilarrasa, V., & Makhnenko, R. (2018). CO<sub>2</sub> Injection Effect on Geomechanical and Flow Properties of Calcite-Rich Reservoirs. *Fluids*, 3, 66. doi:10.3390/fluids3030066
- Kim, K. Y., Zhuang, L., Yang, H., Kim, H., & Min, K.-B. (2016). Strength anisotropy of Berea sandstone: results of X-ray computed tomography, compression tests, and discrete modeling. *Rock Mechanics and Rock Engineering*, 49(4), 1201-1210.
- Koide, H., Tazaki, Y., Noguchi, Y., Nakayama, S., Iijima, M., Ito, K., & Shindo, Y. (1992). Subterranean containment and long-term storage of carbon dioxide in unused aquifers and in depleted natural gas reservoirs. *Energy Conversion and Management*, 33(5), 619-626. doi:[https://doi.org/10.1016/0196-8904\(92\)90064-4](https://doi.org/10.1016/0196-8904(92)90064-4)
- Kranz, R. L., Saltzman, J. S., & Blacic, J. D. (1990). Hydraulic diffusivity measurements on laboratory rock samples using an oscillating pore pressure method. *International Journal of Rock Mechanics and Mining Sciences & Geomechanics Abstracts*, 27(5), 345-352. doi:[http://dx.doi.org/10.1016/0148-9062\(90\)92709-N](http://dx.doi.org/10.1016/0148-9062(90)92709-N)
- Lebedev, M., Wilson, M. E. J., & Mikhaltsevitch, V. (2014). An experimental study of solid matrix weakening in water-saturated Savonnières limestone. *Geophysical Prospecting*, 62(6), 1253-1265. doi:10.1111/1365-2478.12168
- Lebedev, M., Zhang, Y., Sarmadivaleh, M., Barifcani, A., Al-Khdheawi, E., & Iglauer, S. (2017). Carbon geosequestration in limestone: Pore-scale dissolution and geomechanical weakening. *International Journal of Greenhouse Gas Control*, 66, 106-119. doi:10.1016/j.ijggc.2017.09.016
- Li, H. (2016). An Experimental Investigation of Geometric Effects of Core Samples on Berea Sandstone Geo-mechanical Behaviors. In B. Guo, Y. Feng, & A. Hayatdavoudi (Eds.): ProQuest Dissertations Publishing.
- Liu, B., Xu, J., Li, Z., Malekian, R., & Xu, Z. (2018). Modeling of CO<sub>2</sub> transport and pressure buildup in reservoirs during CO<sub>2</sub> storage in saline aquifers: a case in Dongying Depression in China. *Environmental Earth Sciences*, 77(5), 158. doi:10.1007/s12665-018-7341-6
- Louis, L., Baud, P., & Wong, T.-f. (2009). Microstructural inhomogeneity and mechanical anisotropy associated with bedding in Rothbach sandstone. *Pure and Applied Geophysics*, 166(5-7), 1063-1087.
- Madonna, C., & Tisato, N. (2013). A new Seismic Wave Attenuation Module to experimentally measure low-frequency attenuation in extensional mode. *Geophysical Prospecting*, 61(2), 302-314. doi:10.1111/1365-2478.12015
- Mikhaltsevitch, V., Lebedev, M., & Gurevich, B. (2016). Laboratory measurements of the effect of fluid saturation on elastic properties of carbonates at seismic frequencies. *Geophysical Prospecting*, 64(4 - Advances in Rock Physics), 799-809. doi:<https://doi.org/10.1111/1365-2478.12404>
- Mitchell, T. M., & Faulkner, D. R. (2008). Experimental measurements of permeability evolution during triaxial compression of initially intact crystalline rocks and implications for fluid flow in fault zones. *Journal of Geophysical Research: Solid Earth*, 113(B11). doi:10.1029/2008JB005588

- Ochi, J., & Vernoux, J.-F. (1998). Permeability decrease in sandstone reservoirs by fluid injection: Hydrodynamic and chemical effects. *Journal of Hydrology*, 208(3), 237-248. doi:[https://doi.org/10.1016/S0022-1694\(98\)00169-3](https://doi.org/10.1016/S0022-1694(98)00169-3)
- Protodyakonov, M. (1960). *New methods of determining mechanical properties of rocks*. Paper presented at the Proceedings of the International Conference on Strata Control.
- Raza, A., Gholami, R., & Sarmadivaleh, M. (2020). Feasibility of limestone reservoirs as a carbon dioxide storage site: An experimental study. *AAPG bulletin*, 104(1), 83-96. doi:10.1306/04241918124
- Richard, T., Dagrain, F., Poyol, E., & Detournay, E. (2012). Rock strength determination from scratch tests. *Engineering Geology*, 147-148, 91-100. doi:<https://doi.org/10.1016/j.enggeo.2012.07.011>
- Rigg, A., Allinson, G., Bradshaw, J., Ennis-King, J., Gibson-Poole, C., Hillis, R., . . . Streit, J. (2001). The search for sites for geological sequestration of CO<sub>2</sub> in Australia: A progress report on GEODISC. *The APPEA Journal*, 41(1), 711-726.
- Ringrose, P. S., Mathieson, A. S., Wright, I. W., Selama, F., Hansen, O., Bissell, R., . . . Midgley, J. (2013). The In Salah CO<sub>2</sub> Storage Project: Lessons Learned and Knowledge Transfer. *Energy Procedia*, 37, 6226-6236. doi:<https://doi.org/10.1016/j.egypro.2013.06.551>
- Roels, S., Carmeliet, J., & Hens, H. (2003). Modelling Unsaturated Moisture Transport in Heterogeneous Limestone. *Transport in Porous Media*, 52(3), 333-350. doi:10.1023/A:1023552011642
- Rogers, J. J., & Head, W. B. (1961). Relationships between porosity, median size, and sorting coefficients of synthetic sands. *Journal of Sedimentary Research*, 31(3), 467-470.
- Rohmer, J., Pluymakers, A., & Renard, F. (2016). Mechano-chemical interactions in sedimentary rocks in the context of CO<sub>2</sub> storage: Weak acid, weak effects? *Earth-Science Reviews*, 157, 86-110. doi:<https://doi.org/10.1016/j.earscirev.2016.03.009>
- Rutqvist, J., Birkholzer, J., Cappa, F., & Tsang, C. F. (2007). Estimating maximum sustainable injection pressure during geological sequestration of CO<sub>2</sub> using coupled fluid flow and geomechanical fault-slip analysis. *Energy Conversion and Management*, 48(6), 1798-1807. doi:<https://doi.org/10.1016/j.enconman.2007.01.021>
- Sayegh, S. G., Krause, F. F., Girard, M., & DeBree, C. (1990). Rock/Fluid Interactions of Carbonated Brines in a Sandstone Reservoir: Pembina Cardium, Alberta, Canada. *SPE Formation Evaluation*, 5(04), 399-405. doi:10.2118/19392-PA
- Selley, R. C. (2000). *Applied sedimentology*: Elsevier.
- Shulakova, V., Sarout, J., Pimienta, L., Lebedev, M., Mayo, S., Clennell, M. B., & Pervukhina, M. (2017). Effect of supercritical CO<sub>2</sub> on carbonates: Savonnières sample case study. *Geophysical Prospecting*, 65(1), 251-265. doi:10.1111/1365-2478.12369
- Siegesmund, S., & Dürrast, H. (2011). Physical and mechanical properties of rocks. In *Stone in architecture* (pp. 97-225): Springer.
- Sleipner Project. (2011). Retrieved from [http://www.co2captureandstorage.info/project\\_specific.php?project\\_id=26](http://www.co2captureandstorage.info/project_specific.php?project_id=26)
- Sminchak, J., Gupta, N., Byrer, C., & Bergman, P. (2001, 2001-05-31). *Issues Related to Seismic Activity Induced by the Injection of CO<sub>2</sub> in Deep Saline Aquifers*, United States.
- Streit, J. E., & Hillis, R. R. (2004). Estimating fault stability and sustainable fluid pressures for underground storage of CO<sub>2</sub> in porous rock. *Energy*, 29(9), 1445-1456. doi:<https://doi.org/10.1016/j.energy.2004.03.078>
- Ulusay, R. (2014). *The ISRM suggested methods for rock characterization, testing and monitoring: 2007-2014*: Springer.
- UNE-EN. (1926:2007). Natural stone test methods. In *Determination of uniaxial compressive strength*: AENOR.

- Van Stappen, J. F., De Kock, T., De Schutter, G., & Cnudde, V. (2019). Uniaxial compressive strength measurements of limestone plugs and cores: a size comparison and X-ray CT study. *Bulletin of Engineering Geology and the Environment*, 78(7), 5301-5310. doi:10.1007/s10064-018-01448-0
- Walsh, J. B. (1981). Effect of pore pressure and confining pressure on fracture permeability. *International Journal of Rock Mechanics and Mining Sciences & Geomechanics Abstracts*, 18(5), 429-435. doi:[https://doi.org/10.1016/0148-9062\(81\)90006-1](https://doi.org/10.1016/0148-9062(81)90006-1)
- Wigand, M., Carey, J. W., Schütt, H., Spangenberg, E., & Erzinger, J. (2008). Geochemical effects of CO<sub>2</sub> sequestration in sandstones under simulated in situ conditions of deep saline aquifers. *Applied Geochemistry*, 23(9), 2735-2745. doi:<https://doi.org/10.1016/j.apgeochem.2008.06.006>
- Xu, P., & Yang, S.-Q. (2016). Permeability evolution of sandstone under short-term and long-term triaxial compression. *International Journal of Rock Mechanics and Mining Sciences*, 85, 152-164. doi:<http://dx.doi.org/10.1016/j.ijrmms.2016.03.016>
- Xu, T., Apps, J. A., & Pruess, K. (2005). Mineral sequestration of carbon dioxide in a sandstone-shale system. *Chemical Geology*, 217(3-4 SPEC. ISS.), 295-318. doi:10.1016/j.chemgeo.2004.12.015
- Zhang, F., Ye, B., Ye, W. M., & Xua, L. (2017). Measurement of Supercritical CO<sub>2</sub> Permeability in Porous Rock at Reservoir Conditions. In A. Ferrari & L. Laloui (Eds.), *Advances in Laboratory Testing and Modelling of Soils and Shales (ATMSS)* (pp. 69-77). Cham: Springer International Publishing.
- Zhang, L. (2013). Aspects of rock permeability. *Frontiers of Structural and Civil Engineering*, 7(2), 102-116. doi:10.1007/s11709-013-0201-2
- Zhang, Y., Lebedev, M., Sarmadivaleh, M., Yu, H., & Iglauer, S. (2018). *The Elastic Moduli Change After Carbon Dioxide Flooding Into Limestone: An Experimental Study*. Paper presented at the Proceedings of the 6th Unconventional Resources Technology Conference.
- Zhang, Y., Sarmadivaleh, M., Lebedev, M., Barifcani, A., Rezaee, R., Testamantia, N., & Iglauer, S. (2016). *Geo-Mechanical Weakening of Limestone Due to Supercritical CO<sub>2</sub> Injection*. Paper presented at the Offshore Technology Conference Asia.
- Zhou, X., Zeng, Z., & Liu, H. (2011). *Stress-dependent Permeability of Carbonate Rock And Its Implication to CO<sub>2</sub> Sequestration*. Paper presented at the 45th U.S. Rock Mechanics / Geomechanics Symposium, San Francisco, California.
- Zhu, W., Montesi, L. G. J., & Wong, T.-f. (1997). Shear-enhanced compaction and permeability reduction: Triaxial extension tests on porous sandstone. *Mechanics of Materials*, 25(3), 199-214. doi:[https://doi.org/10.1016/S0167-6636\(97\)00011-2](https://doi.org/10.1016/S0167-6636(97)00011-2)

“Every reasonable effort has been made to acknowledge the owners of copyright material. I would be pleased to hear from any copyright owner who has been omitted or incorrectly acknowledged”